

AFRL-ML-WP-TR-2004-4282

**NONDESTRUCTIVE EVALUATION
(NDE) TECHNOLOGY INITIATIVE
PROGRAM (NTIP)**

**Delivery Order 0033: Magnetostrictive Shear
Guided Wave Sensor Technology for Bond Line
Monitoring**



Glenn M. Light, Ph.D., Hegeon Kwun, Ph.D., Sang Kim, Ph.D., Robert Spinks, Martin J. Sablik, Ph.D., and Myoung Choi, Ph.D.

**Southwest Research Institute
Department of Sensor Systems and NDE Technology
6220 Culebra Road
San Antonio, TX 78228**

JUNE 2003

Final Report for 17 June 2002 – 30 June 2003

Approved for public release; distribution is unlimited.

STINFO FINAL REPORT

**MATERIALS AND MANUFACTURING DIRECTORATE
AIR FORCE RESEARCH LABORATORY
AIR FORCE MATERIEL COMMAND
WRIGHT-PATTERSON AIR FORCE BASE, OH 45433-7750**

NOTICE

USING GOVERNMENT DRAWINGS, SPECIFICATIONS, OR OTHER DATA INCLUDED IN THIS DOCUMENT FOR ANY PURPOSE OTHER THAN GOVERNMENT PROCUREMENT DOES NOT IN ANY WAY OBLIGATE THE U.S. GOVERNMENT. THE FACT THAT THE GOVERNMENT FORMULATED OR SUPPLIED THE DRAWINGS, SPECIFICATIONS, OR OTHER DATA DOES NOT LICENSE THE HOLDER OR ANY OTHER PERSON OR CORPORATION; OR CONVEY ANY RIGHTS OR PERMISSION TO MANUFACTURE, USE, OR SELL ANY PATENTED INVENTION THAT MAY RELATE TO THEM.

THIS REPORT HAS BEEN REVIEWED BY THE OFFICE OF PUBLIC AFFAIRS (ASC/PA) AND IS RELEASABLE TO THE NATIONAL TECHNICAL INFORMATION SERVICE (NTIS). AT NTIS, IT WILL BE AVAILABLE TO THE GENERAL PUBLIC, INCLUDING FOREIGN NATIONALS.

THIS TECHNICAL REPORT HAS BEEN REVIEWED AND IS APPROVED FOR PUBLICATION.

/s/

THOMAS J. MORAN, Project Engineer
Nondestructive Evaluation Branch
Metals, Ceramics & NDE Division

/s/

JAMES C. MALAS, Branch Chief
Nondestructive Evaluation Branch
Metals, Ceramics & NDE Division

/s/

GERALD J. PETRAK, Assistant Chief
Metals, Ceramics & NDE Division
Materials & Manufacturing Directorate

IF YOUR ADDRESS HAS CHANGED, IF YOU WISH TO BE REMOVED FROM OUR MAILING LIST, OR IF THE ADDRESSEE IS NO LONGER EMPLOYED BY YOUR ORGANIZATION, PLEASE NOTIFY AFRL/MLLP, WRIGHT-PATTERSON AFB OH 45433-7750 TO HELP MAINTAIN A CURRENT MAILING LIST.

COPIES OF THIS REPORT SHOULD NOT BE RETURNED UNLESS RETURN IS REQUIRED BY SECURITY CONSIDERATIONS, CONTRACTUAL OBLIGATIONS, OR NOTICE ON A SPECIFIC DOCUMENT.

REPORT DOCUMENTATION PAGE				<i>Form Approved</i> <i>OMB No. 0704-0188</i>				
The public reporting burden for this collection of information is estimated to average 1 hour per response, including the time for reviewing instructions, searching existing data sources, gathering and maintaining the data needed, and completing and reviewing the collection of information. Send comments regarding this burden estimate or any other aspect of this collection of information, including suggestions for reducing this burden, to Department of Defense, Washington Headquarters Services, Directorate for Information Operations and Reports (0704-0188), 1215 Jefferson Davis Highway, Suite 1204, Arlington, VA 22202-4302. Respondents should be aware that notwithstanding any other provision of law, no person shall be subject to any penalty for failing to comply with a collection of information if it does not display a currently valid OMB control number. PLEASE DO NOT RETURN YOUR FORM TO THE ABOVE ADDRESS.								
1. REPORT DATE (DD-MM-YY) June 2003		2. REPORT TYPE Final		3. DATES COVERED (From - To) 06/17/2002 – 06/30/2003				
4. TITLE AND SUBTITLE NONDESTRUCTIVE EVALUATION (NDE) TECHNOLOGY INITIATIVE PROGRAM (NTIP) Delivery Order 0033: Magnetostrictive Shear Guided Wave Sensor Technology for Bond Line Monitoring				5a. CONTRACT NUMBER F33615-97-D-5271-0033				
				5b. GRANT NUMBER				
				5c. PROGRAM ELEMENT NUMBER 62102F				
6. AUTHOR(S) Glenn M. Light, Ph.D., Hegeon Kwun, Ph.D., Sang Kim, Ph.D., Robert Spinks, Martin J. Sablik, Ph.D., and Myoung Choi, Ph.D.				5d. PROJECT NUMBER 4349				
				5e. TASK NUMBER 40				
				5f. WORK UNIT NUMBER 01				
7. PERFORMING ORGANIZATION NAME(S) AND ADDRESS(ES) Southwest Research Institute Department of Sensor Systems and NDE Technology 6220 Culebra Road San Antonio, TX 78228				8. PERFORMING ORGANIZATION REPORT NUMBER				
9. SPONSORING/MONITORING AGENCY NAME(S) AND ADDRESS(ES) Materials and Manufacturing Directorate Air Force Research Laboratory Air Force Materiel Command Wright-Patterson AFB, OH 45433-7750				10. SPONSORING/MONITORING AGENCY ACRONYM(S) AFRL/MLLP				
				11. SPONSORING/MONITORING AGENCY REPORT NUMBER(S) AFRL-ML-WP-TR-2004-4282				
12. DISTRIBUTION/AVAILABILITY STATEMENT Approved for public release; release is unlimited.								
13. SUPPLEMENTARY NOTES Report contains color.								
14. ABSTRACT <p>The magnetostrictive sensor (MsS) consists of a 0.005-0.010-inch-thick nickel strip bonded to the aircraft structure and activated with an excitation coil to generate an ultrasonic guided wave in the structure. The MsS is fixed to the surface and can remain on the surface for many years, thus, allowing data to be collected periodically to be carefully compared to a reference data so small changes in the structure can easily be detected. During this project, SwRI studied temperature and stress effects on the MsS bonded with various adhesives to various materials, evaluated the MsS for a number of geometries, and developed a model to help characterize the reflected guided waves from various types of defects. Data acquisition and analysis software was demonstrated and the MsS was optimized.</p> <p>The results obtained showed that the MsS bonded onto aluminum structure with 3MTM467 adhesive can be used over a temperature range of -65°F to 150°F to detect 1/4 inch by 1/4 inch edge delaminations in adhesively bonded patches, changes in crack growth of approximately 0.1 inch in defects under the patch, and defects such as cracks and corrosion as small as 0.03 inch by 0.03 inch under fasteners.</p>								
15. SUBJECT TERMS Magnetostrictive, Sensors, Bonding, and Modeling								
16. SECURITY CLASSIFICATION OF: <table border="1" style="width: 100%; border-collapse: collapse; font-size: x-small;"> <tr> <td style="padding: 2px;">a. REPORT Unclassified</td> <td style="padding: 2px;">b. ABSTRACT Unclassified</td> <td style="padding: 2px;">c. THIS PAGE Unclassified</td> </tr> </table>			a. REPORT Unclassified	b. ABSTRACT Unclassified	c. THIS PAGE Unclassified	17. LIMITATION OF ABSTRACT: SAR		18. NUMBER OF PAGES 138
a. REPORT Unclassified	b. ABSTRACT Unclassified	c. THIS PAGE Unclassified						
19a. NAME OF RESPONSIBLE PERSON (Monitor) Thomas J. Moran			19b. TELEPHONE NUMBER (Include Area Code) (937) 255-9800					

TABLE OF CONTENTS

	<u>Page</u>
1. DESCRIPTION OF THE SCOPE OF WORK.....	1
2. TECHNICAL DISCUSSION.....	2
2.1 Sensor Issues	2
2.1.1 Bonding versus Temperature Range.....	2
2.1.1.1 Nickel on Steel.....	2
2.1.1.2 Nickel on Aluminum	3
2.1.2 Bonding versus Mechanical Stress Testing	11
2.1.2.1 Temperature Related Stress Issues and How Magnetostrictive Properties Are Affected.....	22
2.1.2.2 Discussion of Stress Effect Experiments.....	25
2.1.2.3 Results Obtained for the Stress Measurement Effects.....	27
2.1.2.4 Further Investigations on the Behavior of Nickel Strip During Stressing	32
2.1.2.5 Modeling Results -Effect of Stress on Nickel Films and Strips—Literature Survey	33
2.1.3 Investigation of Corrosion Issues with Bonded Nickel Strips on Steel and Aluminum	37
2.1.3.1 Nickel on Steel.....	37
2.1.3.2 Nickel on Aluminum	38
2.1.3.3 Experiments to Determine Whether the Nickel Strip Can Be Activated by a Coil Placed on the Other Side of the Aluminum Panel	38
2.1.3.4 Effects of Simulated Altitude on Bonding of Nickel to Aluminum	43
2.2 Data Acquisition and Analysis	43
2.3 Modeling	43
2.3.1 Modeling For Propagation in Pipe.....	48
2.3.2 Modeling for Plate (Two-dimensional Wave Motions)	50
2.3.3 Guided Wave Propagation by a Line Source.....	51
2.3.4 Guide Wave Echo Signal Reflected from a Line Defect.....	54

TABLE OF CONTENTS (cont'd)

	<u>Page</u>
2.4 Examples of Geometries Evaluated Using MsS	54
2.4.1 Bonded Thermal Protection for Shuttle	54
2.4.2 Flat Aluminum Plate with Adhesively Bonded Patch Using PC MsS	62
2.4.3 Work on Detection of Defect Growth Under the Patch Using MsS.....	76
2.4.4 Defects Under Fasteners	78
2.4.5 Cryogenic Fuel Lines for NASA	98
3. CONCLUSIONS	108
4. FUTURE WORK	109
5. REFERENCES	110
APPENDIX 1— Information on Epoxies Evaluated to Determine their Capability to Couple T-Waves through the Epoxy into the Plate	111
APPENDIX 2— Theoretical Method for Understanding the Coupling Efficiency for Magnetostrictive Generation of Elastic Waves and for Deciding How To Select the Best Materials for the Magnetostrictive Generation of Elastic Waves	113

LIST OF FIGURES

<u>Figure</u>	<u>Page</u>
Figure 1. Results of MsS monitoring (consisting of subtracting the reference signal I from the signal obtained for various conditions) of steel pipe subjected to a liquid nitrogen bath. The top scan shows no change in the pipe; middle scan is after a small notch has been introduced; bottom scan is after the notch has been increased in size.....	3
Figure 2. Data collected prior to thermal cycling, after one cycle, after two cycles, and after 100 cycles.....	6
Figure 3. Data obtained from 0.010-inch-thick nickel for only one temperature cycle (a-c) and for additional thermal cycling of up to 15 cycles (d).....	9
Figure 4. MsS data waveforms collected after various thermal cycles for nickel strip bonded to aluminum with 5-minute epoxy. The top waveform is the reference collected at approximately 70°F. The various waveforms are collected after different cycles (the temperature shown is the low temperature in the cycle which started at 70°F and returned to 70°F). The notation "after remag" denotes data collected after remagnetizing the nickel strip. From the data, it can be seen that the MsS signal begins to degrade after a thermal cycle of -40°F but can be brought back to reference level after remagnetization. However, after the -65°F cycle even remagnetization could not make the signal return.	12
Figure 5. MsS data waveforms collected after various thermal cycles for nickel strip bonded to aluminum with 3M™467 adhesive. The top waveform is the reference collected at approximately 70°F. The various waveforms are collected after different cycles (the temperature shown is the low temperature in the cycle which started at 70°F and returned to 70°F). The notation "after remag" denotes data collected after remagnetizing the nickel strip. From the data, it can be seen that the MsS signal does not degrade down to -65°F even after 17 cycles.....	13
Figure 6. MsS data waveforms collected after various thermal cycles for nickel strip bonded to aluminum with 5-minute epoxy. The top waveform is the reference, the second is the waveform after 17 cycles down to -65°F, the third is after remagnetization, the fourth is after 16 cycles up to 150°F, and the final waveform is after remagnetization. The MsS signal is degraded.....	14
Figure 7. MsS data waveforms collected after various thermal cycles for nickel strip bonded to aluminum with 3M™467 adhesive. The top waveform is the reference, the second is the waveform after 17 cycles down to -65°F, the third is after remagnetization, the fourth is after 16 cycles up to 150°F, and the final waveform is after remagnetization. The MsS signal remains unchanged through the cycling.	15
Figure 8. MsS data waveforms collected after various mechanical stresses produced by bending the aluminum plate over a mandrel for nickel strip bonded to the aluminum plate with 3M™467 adhesive. The top waveform is the reference; the second waveform is after one cycle at a compression equivalent to -37°F and -65°F. No degradation of the MsS signal was observed.	16
Figure 9. MsS data waveforms collected after various mechanical stresses produced by bending the aluminum plate over a mandrel for nickel strip bonded to the aluminum plate with 3M™467 adhesive. The top waveform is the reference; the second waveform is after one cycle at a tension equivalent to 183°F and 212°F. No degradation of the MsS signal was observed.	17

Figure 10. MsS data waveforms collected after large numbers of compression cycles equivalent to -65°F for nickel bonded to an aluminum plate with 3M™467 adhesive. The top waveform is the reference. Each successive waveform is after an additional 100 cycles of compression. Notice the waveform remains basically unchanged.	18
Figure 11. Same data as shown in Figure 10, but after remagnetization. Notice that the waveform remains basically unchanged.	19
Figure 12. MsS data waveforms collected after large numbers of tension cycles equivalent to 212°F for nickel bonded to an aluminum plate with 3M™467 adhesive. The top waveform is the reference. Each successive waveform is after an additional 400, 600, 800, and 1,000 cycles of tension with and without remagnetization. Notice the waveform remains basically unchanged.	20
Figure 13. MsS data waveforms collected after various thermal cycles for nickel strip bonded to aluminum with 5-minute epoxy. The top waveform is the reference, the second is the waveform after 17 cycles down to 150°F, the third is after remagnetization, the fourth is after 500 cycles of compressive stress equivalent to -66°F, and the final waveform is after remagnetization. The MsS signal is degraded.	21
Figure 14. Strain histories for the cooled and heated samples, respectively. The cooling range was from 73°F (23°C) to -65°F (-54°C), and the heating range was from 73°F (23°C) to 151°F (66°C).	23
Figure 15. Simplified depiction of magnetic domains in the nickel before application of the biasing magnetic field. The arrows represent the localized magnetic orientation of each domain.	24
Figure 16. Illustration showing that all the domains have a common orientation, thus, the nickel strip has been magnetized with a field along its longitudinal axis	24
Figure 17. Theorized orientation of the nickel domains after cooling cycle when compressive stress is applied. All are oriented perpendicular to the stress axis.	24
Figure 18. Magnetization curves of five test samples immediately after fabrication	29
Figure 19. Change in magnetization curves caused by strain history	30
Figure 20. Behavior of previously strained samples after demagnetization versus baseline.	30
Figure 21. Waveforms at (a) baseline, and (b) after strain and demagnetization of nickel sensor (waveforms are basically the same).	32
Figure 22. Plot of fractional change in length as a function of applied magnetic field strength (see Reference [1]).	35
Figure 23. Waveforms obtained from the nickel (top waveform), the iron-cobalt (50/50) alloy (middle waveform), and the iron-cobalt (50/50) with 20 dB more gain. All magnetostrictive material was bonded to a 1/8-inch-thick aluminum plate.	36
Figure 24. The top waveform is the reference waveform obtained with the nickel and coil on the same side of the aluminum plate with zero liftoff between the nickel and the coil; the middle waveform obtained with a 0.06-inch-thick aluminum plate placed between the nickel and the coil; and the lower waveform obtained with the coil placed on the opposite side of the nickel on the aluminum plate surface so that there was approximately 0.125 inch of aluminum between the coil and the nickel.	40
Figure 25. Top waveform obtained with the coil placed on the opposite side of the nickel on the aluminum plate surface so that there was approximately 0.125 inch of aluminum between the coil and the nickel; middle waveform obtained when an Al-5 magnet was placed across the nickel foil during data collection; and the lower waveform obtained under the same conditions as the middle waveform, except the pulser power was increased from 60 to 80 percent.	41

Figure 26. The top waveform is the baseline with the sensor on top of the nickel foil. The second waveform is with 1/8 inch of aluminum between the nickel and sensor with a magnet over the nickel foil. The third waveform is with the magnet over the coil but located over one edge of the nickel. The fourth waveform is with the magnet centered over the coil and over the location of the nickel. The fifth waveform is the same as the third waveform but with 60 dB gain versus 36 dB gain.	42
Figure 27. MsS data collected from a nickel strip bonded to an aluminum plate using the 3M™467 adhesive. The plate was subjected to a simulated altitude and thermal cycling. The plate started at 70°F and atmospheric pressure, dropped to –65°F and 40,000 feet pressure, and then returned to atmospheric pressure at 70°F and then heated to 150°F. As can be observed in the data, there is no significant change in the magnetostrictive sensor signals.	44
Figure 28. Reference data compared to another data set collected before disbonding.....	45
Figure 29. Inspection waveform (called monitoring data) showing a slight change at a distance of approximately 23 inches from the end of the plate.....	46
Figure 30. Defect cross section and its transmission line model representation	48
Figure 31. Examples of simulated defect signal waveforms	49
Figure 32. Cross section of defects in the axial direction (top–stepwise change in pipewall; bottom–circular corrosion pit)	49
Figure 33. Illustration of relative location of MsS probe and defect for guided wave simulation in plate.....	52
Figure 34. RF source signal (top) generated with MsS system and its frequency spectrum (bottom). f_c : frequency at peak amplitude in frequency spectrum, $\lambda_c = V/f_c$: wavelength at center frequency.....	52
Figure 35. Amplitude distribution along the distance perpendicular to the MsS probe	53
Figure 36. Amplitude lateral distribution at 40-times wavelength distance	54
Figure 37. Reflected amplitude variation at distances of 10λ (a) and 40λ (b) from the source as the defect size increases	55
Figure 38. Photograph showing the placement of the MsS nickel strip probes for propagating guided waves along the length of the test panel	56
Figure 39. Photograph showing the placement of the MsS nickel strip probes for propagating guided waves along the width of the test panel	56
Figure 40. Profile view of part of the test panel showing the pocket filled with honeycomb in relation to the flat aluminum panel	57
Figure 41. Bottom view of the test panel showing the pocket filled with honeycomb. The bottom face sheet appears to be brazed or welded to the edge of the plate.	57
Figure 42. Profile of the test panel.....	58
Figure 43. Data obtained from the placement of the MsS nickel strip probes along the length of the test panel in PE mode.....	58
Figure 44. Photograph of the space shuttle simulated door panel with the TPS bonded to the door panel. The shuttle tiles use a similar bonding technique.	59
Figure 45. Photograph of the debonded region of the space shuttle TPS on the door panel. This is designated as a small delamination in the data.	59
Figure 46. MsS data collected using the PC mode on the space shuttle door panel with the TPS (not the tile) bonded to the surface. The top waveform is the reference taken when the panel had the delamination shown in Figure 45.	60
Figure 47. MsS monitoring data obtained by subtracting the reference from another waveform collected with no additional damage (top waveform), subtracting the reference from the	

waveform where more delamination occurred (second waveform), subtracting the reference from the waveform where more delamination occurred (third waveform), and finally subtracting the reference from the waveform where the small TPS section was totally debonded.	61
Figure 48. Illustration of six different delamination steps.....	62
Figure 49. Inspection data obtained from the adhesively bonded patch illustrated in Figure 45 using the PC MsS mode. The first two waveforms are denoted as reference with no delamination. The next waveform shows the reference minus the data obtained when corner 1 was delaminated. The subsequent waveforms show the reference minus the data obtained from delamination processes 2 through 6. Notice that in this case, even the small delamination can be detected in the monitoring mode.	63
Figure 50. Monitoring data obtained from the adhesively bonded patch illustrated in Figure 45 using the PC MsS mode. The first two waveforms are denoted as reference with no delamination. The next waveform shows the reference minus the data obtained when corner 1 was delaminated. The subsequent waveforms show the reference minus the data obtained from delamination processes 2 through 6. Notice that in this case, even the small delamination can be detected in the monitoring mode.	64
Figure 51. Illustration of change in velocity as a function of bonding quality	65
Figure 52. Waveform data obtained from simulated bond structure (conditions 1 through 4) and bonded structure (conditions 5 through 8) with materials being removed to simulate debonding.....	66
Figure 53. Illustration of process used to evaluate the effect of bonding on guided wave velocity	67
Figure 54. Reference data compared to another data set collected before disbonding.....	68
Figure 55. Inspection waveform (called monitoring data) showing a slight change at a distance of approximately 23 inches from the end of the plate.....	69
Figure 56. Top trace is the reference signal with no delaminations and monitoring data is from step 2 of the delamination process. The subtracted RF signal is the difference between the reference signal and the step 2 delamination process, showing a difference but not what is the difference relative to step 1 of the delamination process.....	70
Figure 57. Top trace is data collected from step 1 of the delamination process and monitoring data is from step 2 of the delamination process. The subtracted RF signal is the comparison of the delamination data from delamination steps 1 and 2, clearly showing the difference and that the difference occurs at the back of the patch.	71
Figure 58. Top trace is the reference signal with no delaminations and monitoring data is from step 3 of the delamination process. The subtracted RF signal is the difference between the reference signal and the step 3 delamination process, showing a difference but not what is the difference relative to steps 1 or 2 of the delamination process. The data from steps 1 or 2 could be used to determine what is the difference relative to each of those steps.....	72
Figure 59. Top trace is the reference signal with no delaminations and monitoring data is from step 4 of the delamination process. The subtracted RF signal is the difference between the reference signal and the step 4 delamination process, showing a difference but not what is the difference relative to steps 1, 2 or 3 of the delamination process. The data from steps 1, 2 or 3 could be used to determine what is the difference relative to each of those steps.	73
Figure 60. Top trace is the reference signal with no delaminations and monitoring data is from step 5 of the delamination process. The subtracted RF signal is the difference between the reference signal and the step 5 delamination process, showing a difference but not what is	

the difference relative to steps 1, 3, or 4 of the delamination process. The data from steps 1, 2, 3 or 4 could be used to determine what is the difference relative to each of those steps.	74
Figure 61. Top trace is the reference signal with no delaminations and monitoring data is from step 6 of the delamination process. The subtracted RF signal is the difference between the reference signal and the step 6 delamination process. There is a large difference.	75
Figure 62. Top trace is the reference signal with no delaminations and monitoring data is from step 7 of the delamination process. The subtracted RF signal is the difference between the reference signal and the step 7 delamination process. There is a large difference.	76
Figure 63. Photograph of the adhesively bonded patch on an aluminum substrate showing the beveled edges. The patch is approximately 8 inches long, 4 inches wide, and 1/16 inch thick.....	77
Figure 64. MsS waveform and monitoring data comparing two data sets for the case of no defect under the adhesively bonded aluminum patch.....	79
Figure 65. MsS waveform and monitoring data comparing the case of no defect under the adhesively bonded aluminum patch to the case where a 0.5-inch-long, 1/8-inch-deep defect was placed below the adhesively bonded aluminum patch	80
Figure 66. MsS waveform and monitoring data comparing the case of no defect under the adhesively bonded aluminum patch to the case where a 0.6-inch-long, 1/8-inch-deep defect was placed below the adhesively bonded aluminum patch	81
Figure 67. MsS waveform and monitoring data comparing the case of no defect under the adhesively bonded aluminum patch to the case where a 0.7-inch-long, 1/8-inch-deep defect was placed below the adhesively bonded aluminum patch	82
Figure 68. MsS waveform and monitoring data comparing the case of no defect under the adhesively bonded aluminum patch to the case where a 0.8-inch-long, 1/8-inch-deep defect was placed below the adhesively bonded aluminum patch	83
Figure 69. MsS waveform and monitoring data comparing the case of no defect under the adhesively bonded aluminum patch to the case where a 0.9-inch-long, 1/8-inch-deep defect was placed below the adhesively bonded aluminum patch	84
Figure 70. MsS waveform and monitoring data comparing the case of no defect under the adhesively bonded aluminum patch to the case where a 1.0-inch-long, 1/8-inch-deep defect was placed below the adhesively bonded aluminum patch	85
Figure 71. MsS waveform and monitoring data comparing the case where a 0.5-inch-long, 1/8-inch-deep defect was placed below the adhesively bonded aluminum patch to the case where the defect length was increased by 0.1 inch to 0.6 inch.....	86
Figure 72. MsS waveform and monitoring data comparing the for the case where a 0.5-inch-long, 1/8-inch-deep defect was placed below the adhesively bonded aluminum patch to the case where the defect length was increased by 0.2 inch to 0.7 inch.....	87
Figure 73. Photograph of the test plate showing holes and fasteners	88
Figure 74. Waveforms obtained for no defects in the holes (top) and another case of no defects in the holes (middle). The lower waveforms show the difference data and it is clear that the difference is basically a flat line except where the sensor output signal was saturated.....	89
Figure 75. Waveforms obtained for no defects in the holes (top) and with a defect that is approximately 0.003 inch by 0.02 inch diameter inch and in the hole 20 inches from the sensor. The lower waveforms show the difference data and it is clear that the small defect can be seen at 20 inches.	90
Figure 76 Waveforms obtained for no defects in the holes (top) and with a defect that is approximately 0.01 inch by 0.03 inch diameter and in the hole 20 inches from the sensor.	

The lower waveforms show the difference data and it is clear that the small defect can be seen at 20 inches.	91
Figure 77. Photograph of the 0.02 inch by 0.05 inch by 0.10 inch defect in the tapered hole	92
Figure 78. Photograph of the 0.006 inch by 0.05 inch by 0.1 inch defect in the tapered hole	92
Figure 79. Waveforms obtained for no defects in the holes (top) and with a defect that is approximately 0.02 inch by 0.05 inch by 0.1 inch and in the hole 20 inches from the sensor. The lower waveforms show the difference data and it is clear that the small defect can be seen at 20 inches.	93
Figure 80. Waveforms obtained for no defects in the holes (top) and with a defect that is approximately 0.025 inch by 0.08 inch in diameter and in the hole 20 inches from the sensor. The lower waveforms show the difference data and it is clear that the small defect can be seen at 20 inches.	94
Figure 81. The top waveform (reference) was from the case where the large defect was in the hole 20 inches from the MsS. The middle (monitoring) waveform is from the case where the 0.003 inch by 0.01 inch by 0.01 inch defect was introduced into the fastener hole approximately 32 inches from the MsS. Again, it is impossible to visually detect any difference between the monitoring data and baseline data. However, when the difference is obtained, the defect clearly is detected at approximately 32 inches from the MsS.	95
Figure 82. The top waveform (reference) was from the case where the large defect was in the hole 20 inches from the MsS. The middle (monitoring) waveform is from the case where the 0.006 inch by 0.03 inch by 0.03 inch defect was introduced into the fastener hole approximately 32 inches from the MsS. Again, it is impossible to visually detect any difference between the monitoring data and baseline data. However, when the difference is obtained, the defect clearly is detected at approximately 32 inches from the MsS.	96
Figure 83. The top waveform (reference) was from the case where the large defect was in the hole 20 inches from the MsS. The middle (monitoring) waveform is from the case where the 0.006 inch by 0.05 inch by 0.05 inch defect was introduced into the fastener hole approximately 32 inches from the MsS. Again, it is impossible to visually detect any difference between the monitoring data and baseline data. However, when the difference is obtained, the defect clearly is detected at approximately 32 inches from the MsS.	97
Figure 84. The top waveform (reference) was from the case where the defect was in the hole 23 inches from the MsS. The middle (monitoring) waveform is from the case where a defect approximately 0.01 inch deep by 0.03 inch diameter was introduced into the fastener hole approximately 23 inches from the MsS. Again, it is impossible to visually detect any difference between the monitoring data and baseline data. However, when the difference is obtained, the defect clearly is detected at approximately 23 inches from the MsS.	99
Figure 85. The top waveform (reference) was from the case where the defect was in the hole 23 inches from the MsS. The middle (monitoring) waveform is from the case where a defect size was increased to approximately 0.02 inch deep by 0.05 inch diameter. Again, it is impossible to visually detect any difference between the monitoring data and baseline data. However, when the difference is obtained, the defect clearly is detected at approximately 23 inches from the MsS.	100
Figure 86. The top waveform (reference) was from the case where the defect was in the hole 23 inches from the MsS. The middle (monitoring) waveform is from the case where a defect size was increased to approximately 0.025 inch by 0.065 inch in diameter. Again, it is impossible to visually detect any difference between the monitoring data and baseline data. However, when the difference is obtained, the defect clearly is detected at approximately 23 inches from the MsS.	101

Figure 87. Photograph of the ample pipe used in study. Monitoring MsSs were bonded on each end of the pipe.....	102
Figure 88. Photograph illustrating the placement of the transducers on the sample pipe	102
Figure 89. Comparison of normalized baseline waveform data with normalized monitoring waveform data taken after temperature excursion for the continuous MsS.....	104
Figure 90. Comparison of baseline waveform data with monitoring waveform data taken after temperature excursion for the segmented MsS	105
Figure 91. Waveform data collected with the continuous band nickel MsS showing that the notch is detectable in the data after waveform subtraction is performed.	106
Figure 92. Waveform data collected using the segmented nickel MsS showing that the notch is apparent after subtraction, but less so than in the continuous nickel sensor data.	107

FINAL REPORT
for
Contract No. F3361597D5271, SwRI Project No. 14.05736,
“Magnetostrictive Shear Guided Wave Sensor Technology
for Bond Line Monitoring”

1. DESCRIPTION OF THE SCOPE OF WORK

The scope of the funded work includes the following tasks.

Task 1. Investigation of Environmental Effects on Nickel Foil

Under this task, the subcontractor shall investigate the effect of temperature changes by using a magnetostrictive sensor guided wave probe (MsSGWP) on an aluminum plate placed in an environmental chamber. The MsSGWP data will be collected as the probe is cycled over a range of temperatures representing anticipated in situ conditions. Temperature cycles shall be conducted, and the MsSGWP data shall be correlated as a function of cycle. In addition, the material on which the MsSGWP probe is mounted shall be subjected to a number of impacts that do not damage the material. Survivability and durability of the MsSGWP and its mounting adhesive will be estimated.

Task 2. Determination of Defect Detection Sensitivity Using Monitoring Mode

A key issue to the successful application of monitoring technology is the ability to develop a calibration and defect detection sensitivity method. The parameters that affect wave propagation, including plate thickness, plate material, plate bonding to thermal protection systems (TPS) and other structures, and frequency shall be investigated. Wave attenuation will also be affected by the frequency and bonding of structures. Tests to determine the extent of these effects shall be conducted on several aluminum plates of various thickness ranges.

Task 3. Optimization of Signal Processing Technology for Monitoring

Under this task, the subcontractor shall provide a computerized data analysis process that provides an easy-to-understand monitoring result, i.e., a simple-to-interpret determination of bonding quality and defect growth.

Task 4. Investigation of Signal Processing Technology for Characterizing Defect Signals

The subcontractor shall develop signal-processing tools that will allow characterization of the observed changes in the guided-wave signal. These tools shall capture changes in area of bond, location of bond, quality change, change in defect area, and location of change of defect.

Task 5. Optimize the Transmitter/Receiver Design

Under this task, the subcontractor shall (1) optimize the probe design to allow it to work on a structure with complex curvature as well as on a flat structure and (2) develop a capability to remotely (but in close proximity) activate the sensor and to remotely transmit and receive data.

2. TECHNICAL DISCUSSION

2.1 Sensor Issues

The sensor technology evaluated in this work was the magnetostrictive sensor strip with an excitation coil. Most of the work was conducted using nickel, although some work was also conducted using Permendur (iron/cobalt alloy, 50/50).

2.1.1 Bonding versus Temperature Range

SwRI has been working for over three years with nickel strip bonded to steel using 5-minute epoxy. For most of this work, the nickel was bonded on to steel that experience a temperature range approximately 20°F to 130°F under normal atmospheric conditions (sun, clouds, rain, some ice, and humidity levels ranging from perhaps 10% to 100%RH). The bond quality was not adversely affected by any of these conditions. However, under this project a number of applications on different substrates and in harsh operating environments were studied. The applications included: (1) steel pipe exposed to cryogenic liquids, (2) aluminum pipe exposed to cryogenic liquids, (3) simulated aircraft structure exposed to temperature extremes ranging from -65°F to 150°F, and (4) stress extremes ranging from 28,000 psi compression to 28,000 psi tension. For each of these cases, experiments were conducted to determine the ability of the MsS probe to operate under these simulated conditions.

2.1.1.1 Nickel on Steel

One application that was of interest under this project was the ability to inspect and monitoring with the nickel strip MsS probe on a steel pipe that was subjected to liquid nitrogen temperatures (approximately -300°F). SwRI conducted tests that consisted of bonding a nickel strip onto a 2-inch-diameter steel pipe using Adhesive 440 (supplied by Clock Spring Co.). The lap shear strength of this epoxy was estimated to be greater than 1,200 psi. The strip was activated with a sensor coil and data were collected at ambient conditons. Then, the end of the pipe where the nickel strip was bonded was dipped into a bath of liquid nitrogen. The sensor was allowed to stay in the liquid nitrogen bath for approximately 15 minutes. Once the pipe and sensor were removed from the bath, they were allowed to return to room temperature, and MsS data were collected. A difference in the MsS signal before and after the nitrogen bath was observed and traced to a change in the magnetic properties of the nickel possibly caused by the thermal shock of dipping the strip in the liquid nitrogen. However, once the nickel strip was remagnetized on the pipe in accordance with a procedure used previously by SwRI, the signal strength returned to the level observed prior to the nitrogen bath.

Next, a small notch was placed in the pipe and MsS data collected again. Then, the MsS nickel strip was again dipped into liquid nitrogen for 15 minutes and data collected. Once the nickel strip was remagnetized, MsS data was again collected. A

comparison of the data obtained before and after the notch was placed into the pipe clearly showed that the notch could be detected. Then the notch was made larger, the data again showed detection with a larger defect size. The data obtained from these three conditions are illustrated in Figure 1.

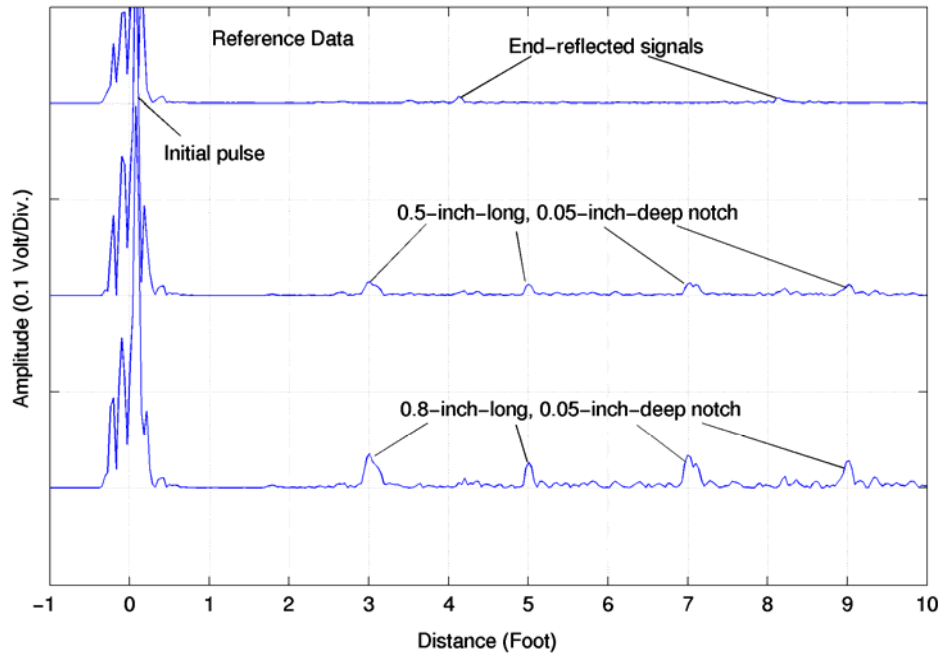


Figure 1. Results of MsS monitoring (consisting of subtracting the reference signal I from the signal obtained for various conditions) of steel pipe subjected to a liquid nitrogen bath. The top scan shows no change in the pipe; middle scan is after a small notch has been introduced; bottom scan is after the notch has been increased in size.

Through previous testing, the bonding characteristics for the Clock Spring[®] 440 epoxy and the Devcon 5-minute[®] Epoxy were shown to be approximately the same. These tests therefore clearly showed that nickel bonded to steel could withstand temperature extremes down to approximately -300°F and still function properly.

2.1.1.2 Nickel on Aluminum

Most of the work conducted on this project was aimed directly at using the nickel bonded to aluminum. The applications and results obtained for these applications using the MsS technology will be described in Section 4 of this report. The purpose of this section of the report is to describe the work conducted with nickel (and other alternative ferromagnetic materials) bonded onto aluminum using 5-minute epoxy or 3MTM467 adhesive. The key parameters in making the magnetostrictive sensor concept successful for monitoring include having an adhesive that (1) can transmit the shear horizontally polarized guided wave from the nickel into the aluminum and (2) maintain the bond of the nickel to the aluminum in various types of environment (mechanical and thermal).

(1) Epoxy Bonding

Previously reported SwRI data collected from over 20 different epoxies and adhesives showed that the Devcon 5-Minute® Epoxy was optimum based on effectiveness in transmitting the shear wave into structure geometry and in terms of ease of application to the structure. This list of epoxies and adhesives evaluated and information about them are contained in Appendix 1. In addition, SwRI has used Devcon 5-Minute® Epoxy for more than 3 years on steel pipe for temperatures ranging from approximately 20°F to 150°F without any failures.

To evaluate the nickel strip bonded to aluminum under expected flying aircraft thermal conditions, the following tests were conducted. The initial test consisted of bonding a nickel strip on one end of an aluminum plate that was approximately 34 inches long, 12 inches wide, and 1/8 inch thick. The 0.005-inch-thick nickel strip that was approximately 1 inch wide by 8 inches long was bonded with Duralco 4537N adhesive that had a similar shear lap strength of approximately 6000 psi and a 4-hour cure time. This test plate was then subjected to limited thermal cycling consisting of placing the test panel in a thermal chamber and having the temperature go from 70°F to 150°F to –65°F and then back to 70°F in one hour. Data were collected prior to thermal cycling, after one cycle, after two cycles, and after 100 cycles. Data are shown in Figure 2. The waveform shown in Figure 2(a) was obtained prior to thermal cycling. After one thermal cycle, the nickel strip MsS exhibited approximately 13 dB less amplitude [waveform shown in Figure 2(b)] than it had prior to thermal cycling. The nickel strip was remagnetized and the signal increased by approximately 4 dB [as shown in Figure 2(c)]. The nickel strip was then subjected to the second thermal cycle [shown in Figure 2(d)] and the data obtained showed a reduction in signal strength similar to that observed after the first thermal cycle. Again, the nickel strip was remagnetized [waveform shown in Figure 2(e)] and the magnetostrictive properties were restored to approximately the sensitivity shown in Figure 2(c).

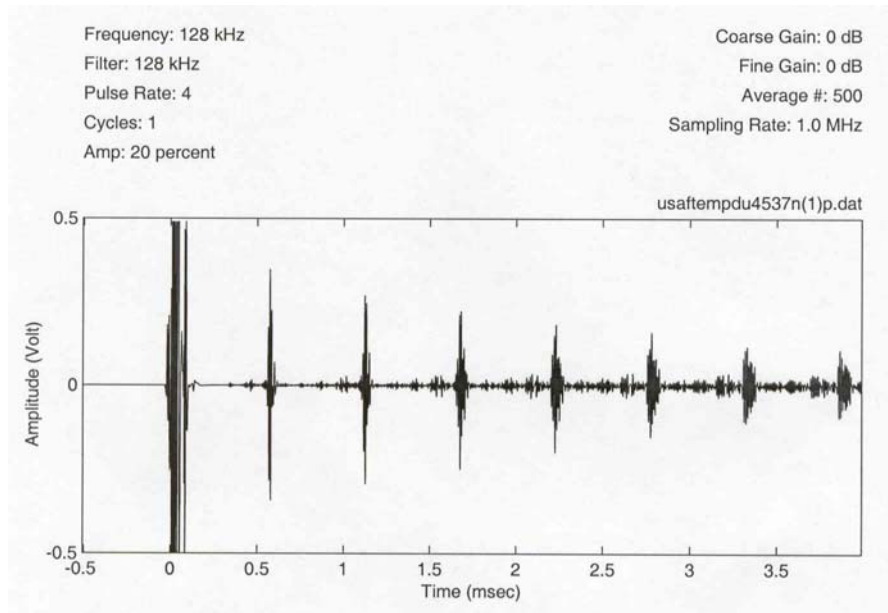


Figure 2(a). Waveform obtained prior to thermal cycling

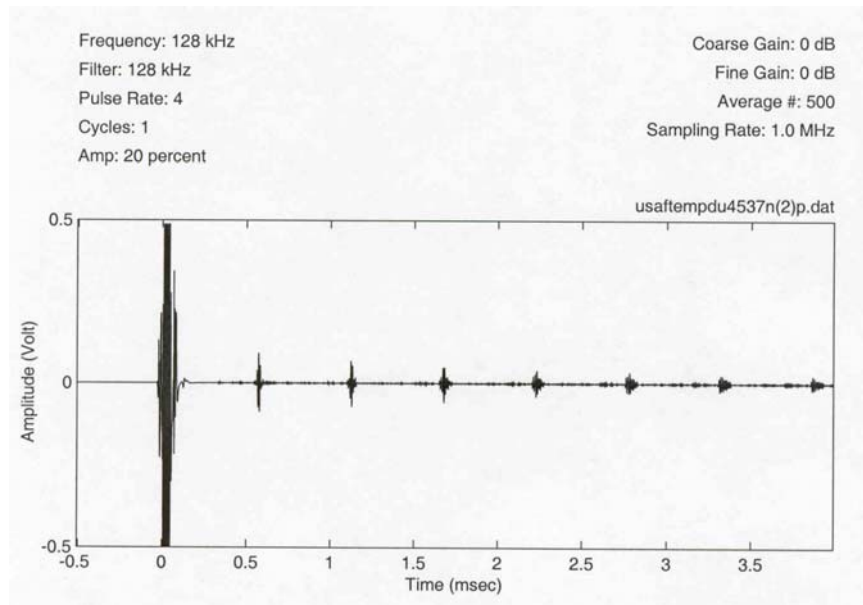


Figure 2(b). Waveform obtained after one thermal cycle

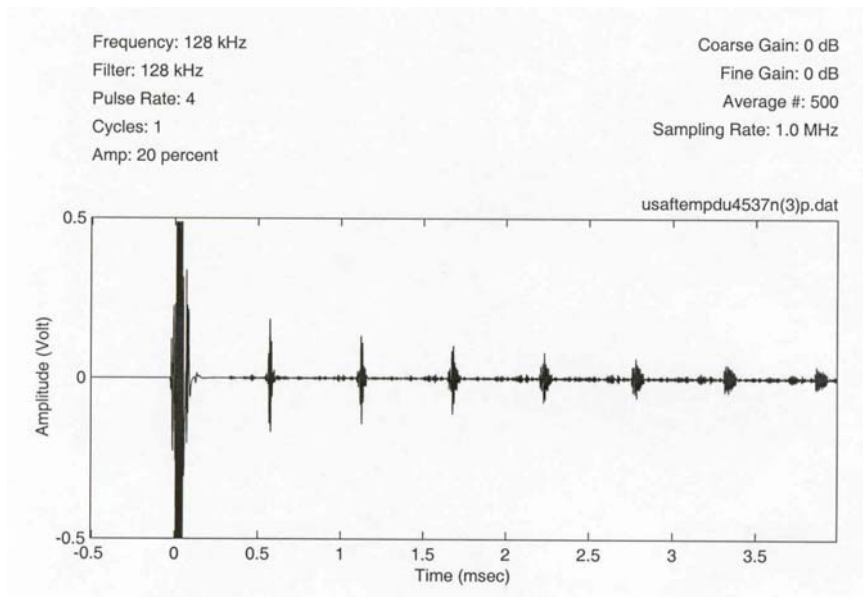


Figure 2(c). Waveform obtained after nickel strip was remagnetized and gained approximately 4 dB

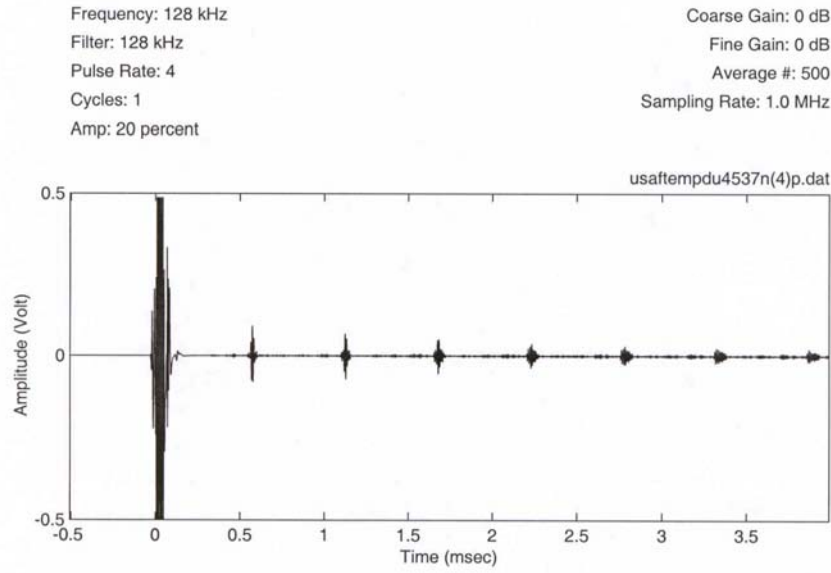


Figure 2(d). Waveform obtained after two thermal cycles

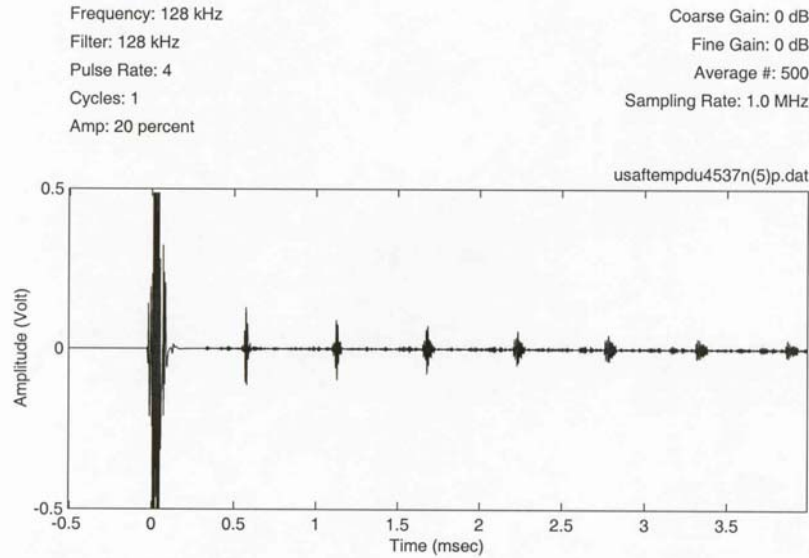


Figure 2(e) Waveform obtained after nickel strip was remagnetized and the magnetostrictive properties were restored to approximately the sensitivity shown in Figure 2(c)

Figure 2. Data collected prior to thermal cycling, after one cycle, after two cycles, and after 100 cycles

After careful consideration of the possible causes of the observed MsS sensitivity loss, the primary cause was hypothesized to be the plastic deformation of the nickel strip under the thermal stress induced by the thermal expansion coefficient (TEC)

mismatch between nickel and aluminum and the resulting degradation in the magnetostrictive properties of the nickel strip. The TEC of three materials are shown in Table 1.

Table 1. Thermal Expansion Coefficients

Aluminum	$23.5 \times 10^{-6}/^{\circ}\text{C}$
Nickel	$13.3 \times 10^{-6}/^{\circ}\text{C}$
Steel	$12.1 \times 10^{-6}/^{\circ}\text{C}$

The test panels used for the initial tests were prepared at room temperature (25°C). The temperature differential for the hot part of the thermal cycle was from 25°C to 65°C, a difference of 40°C. The differential for the low temperature part of the cycle was from 25°C to -54°C, a difference of 79°C. The corresponding strain caused by the TEC mismatch between the aluminum and the nickel strip was:

$$79^{\circ}\text{C} \times (23.5 - 13.3) \times 10^{-6}/^{\circ}\text{C} = 806 \times 10^{-6}.$$

The corresponding stress in nickel strip would have been approximately:

$$\text{Young's modulus} \times \text{strain} = 29.7 \times 10^6 \text{ psi} \times 806 \times 10^{-6} = 23,938 \text{ psi}.$$

This thermal stress is higher than the yield strength of the nickel strip that was approximately 20,000 psi. Under the high thermal mismatch stress on the cold side of the thermal cycle, the nickel strip yielded and was plastically deformed in compression. The mechanical deformation demagnetized the nickel strip and at the same time degraded the magnetostrictive properties of the nickel strip.

A nickel strip bonded to a steel substrate does not lose the MsS sensitivity and is not significantly degraded even after quenching the MsS probe in liquid nitrogen (-196°C) from the room temperature.

The reason that quenching in liquid nitrogen (a much more severe thermal treatment than the thermal cycling used for the aluminum sample) did not cause degradation in the magnetostrictive properties of the nickel strip is due to the good TEC match between the nickel and the steel, the difference in TEC is $1.2 \times 10^{-6}/^{\circ}\text{C}$. The thermal strain between the steel and the nickel strip due to temperature change from ambient room temperature to liquid nitrogen temperature is approximately $[25 - (-196)] \times (13.3 - 12.1) \times 10^{-6} = 265 \times 10^{-6}$. The corresponding stress in nickel is approximately $29.7 \times 10^6 \text{ psi} \times 265 \times 10^{-6} = 7,870 \text{ psi}$, which is substantially lower than the yield strength of the nickel strip. Since no plastic deformation beyond the yield strength of the nickel strip occurred in this case, the nickel strip retained good magnetostrictive properties and the original MsS sensitivity.

Additional preliminary data collected on 0.010-inch-thick nickel bonded onto the same test sample using Duralco 4537 showed similar results. The data obtained from this test sample for only one temperature cycle are shown in Figure 3. Figure 3(a) is prior to thermal cycling, Figure 3(b) is after thermal cycling, and Figure 3(c) is after thermal cycling and remagnetization. However, this clearly shows that the reduction in magnetostrictive properties

caused by the thermal cycle is approximately 2 dB (versus 13 dB for the 0.005-inch-thick nickel) and that after remagnetization, the magnetostrictive properties return completely as compared to continued loss of magnetostrictive properties for the 0.005 inch thick material. Additional thermal cycling of up to 15 cycles showed that the 0.010-inch-thick nickel did not lose its magnetostrictive properties as shown in Figure 3(d).

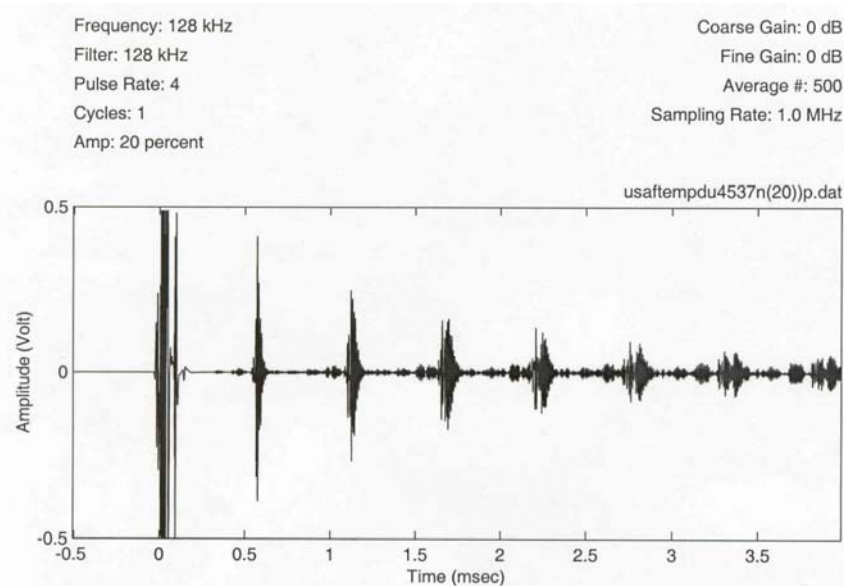


Figure 3(a). Waveform obtained prior to thermal cycling from test sample bonded with Duralco 4537

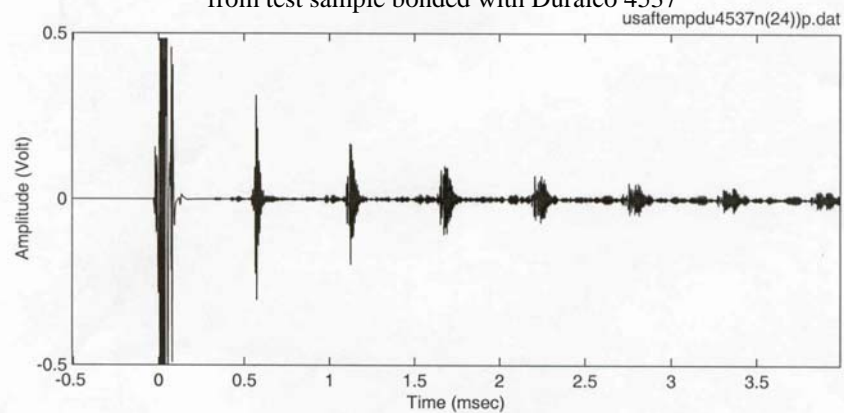


Figure 3(b). Waveform obtained after thermal cycling from test sample bonded with Duralco 4537

Frequency: 128 kHz
Filter: 128 kHz
Pulse Rate: 4
Cycles: 1
Amp: 20 percent

Coarse Gain: 0 dB
Fine Gain: 0 dB
Average #: 500
Sampling Rate: 1.0 MHz

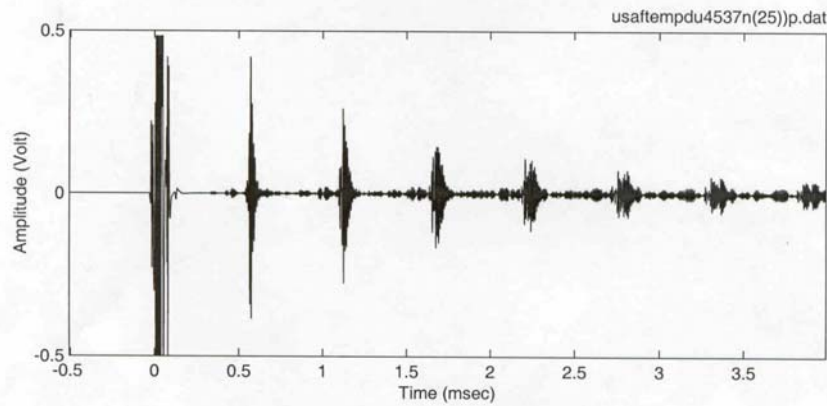


Figure 3(c). Waveform obtained after thermal cycling and remagnetization from test sample bonded with Duralco 4537

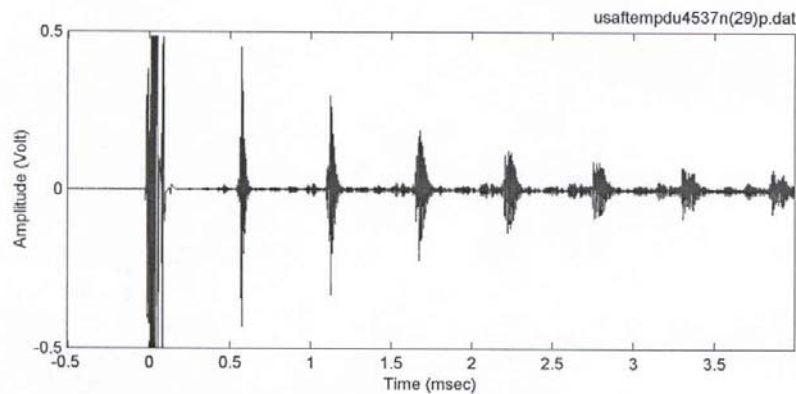


Figure 3(d). Waveform obtained showing that the 0.010-inch-thick nickel did not lose its magnetostrictive properties after 15 thermal cycles

Figure 3. Data obtained from 0.010-inch-thick nickel for only one temperature cycle (a-c) and for additional thermal cycling of up to 15 cycles (d)

Based on these experiments, nickel bonded to aluminum with 5-minute (or similar) epoxy appeared to exhibit questionable properties for monitoring aircraft structure subjected to the expected aircraft thermal cycle of -65°F to 150°F . There are two approaches to solve this potential problem:

- Find a better adhesive that would adequately bond the nickel to the aluminum, couple the guided wave from the nickel into the aluminum, and not effectively transmit the stress, and
- Find a ferromagnetic strip that can withstand the thermal stress caused by the TEC mismatch.

A literature review identified the (1) 3M™467 adhesive as a potential alternative to bond nickel to aluminum aircraft structure and (2) iron cobalt alloys as possible replacement materials for nickel. Iron cobalt alloys have a wide range of magnetostrictive properties based upon the alloy percentage [1].

(2) 3M™467 Adhesive

3M™467 adhesive is used to bond aircraft decals onto airplanes. A comparison of the properties between Devcon 5-Minute® Epoxy and 3M™467 adhesive for bonding nickel to aluminum for use in an expected aircraft thermal and stress environment was conducted. These tests were conducted with two nickel strips bonded to one aluminum panel that is 36 inches long by 12 inches wide by 1/8 inch thick. A 0.010-inch-thick nickel strip was bonded using Devcon 5-Minute® Epoxy on one end of the panel. On the other end, a 0.005-inch-thick nickel strip was bonded to the panel using the 3M™467 adhesive. (Through laboratory tests, it has been previously observed that the 0.010-inch-thick nickel strip bonded with Devcon 5-Minute® Epoxy is more robust to temperature changes and the 0.005-inch-thick nickel strip adhered better to a substrate than a 0.010-inch-thick nickel strip when using the 3M™467 adhesive.) Baseline data were collected with each nickel strip using the same activator coil probe.

The panel was cycled from 70°F to -20°F to 70°F in one hour and MsS data were collected. There was very little effect on either the 5-minute or 3M™467 bonded MsS strips as shown in Figure 4 for the Devcon 5-Minute® Epoxy and Figure 5 for the 3M™467 adhesive (approximately 1 dB). The nickel strip properties were restored when the nickel strip was remagnetized.

The panel was then cycled from 70°F to -40°F to 70°F in one hour and MsS data were collected again. As can be seen in Figure 4, the 5-minute epoxy nickel strip signal was down approximately 2.5 dB, but remagnetization restored the signal to approximately the original level. For the 3M™467 bonded nickel strip, as shown in Figure 5, the signal dropped by about 1 dB, but remagnetization again brought it back to the original level.

However, after cycling the panel from 70°F to -65°F to 70°F, the epoxy bonded nickel showed large degradation (of approximately 5 dB) while the 3M™467 bonded nickel had only a slight change (approximately 1 dB), as shown in Figures 4 and 5. Remagnetization of the Devcon 5-Minute® Epoxy bonded nickel did not restore the signal to the original level after the temperature extremes, while remagnetization of the 3M™467 bonded nickel did return the signal to the original level.

The panel then was subjected to 17 cycles of 70°F to -65°F to 70°F and MsS data were collected. The 5-minute epoxy bonded nickel strip was degraded by another 2.5 dB and remagnetization did not restore the signal level. For the 3M™467 bonded

nickel strip, the signal dropped slightly, but remagnetization returned it to the original level. Note that the initial 3MTM467 bonded nickel strip data are taken with an instrument gain of 10 dB, then reduced to 8 dB, and finally reduced to 6 dB because the signals were increasing.

The panel then was subjected to 16 cycles of 70°F to 150°F to 70°F. The epoxy bonded nickel strip never returned to the original signal level (shown in Figure 6) while the 3MTM467 bonded nickel strip signal remained constant within approximately 1 dB as illustrated in Figure 7.

2.1.2 Bonding versus Mechanical Stress Testing

Tests were conducted for mechanical stresses by bending the same sample used for the thermal testing over wooden mandrels. These mandrels produced equivalent stresses of approximately 18,000 and 24,000 psi in both compression and tension. These tests were conducted primarily for the 3MTM467 adhesive because similar tests previously conducted on the 5-minute epoxy bonded nickel showed the compression cycle significantly degraded the MsS signal. Figure 8 shows the MsS signal after compression of approximately 18,000 and 24,000 psi, and no signal degradation is observed. Similarly, Figure 9 shows the MsS signal after approximately 24,000 psi tension is applied, and again no MsS signal degradation is observed.

The same panel then was subjected to approximately 1,000 cycles of compression of approximately 24,000 psi and MsS data were collected. The reference data (taken prior to cycling) and the data after every 100 cycles up to 1,000 are shown in Figure 10. These data are with no remagnetization of the nickel strips during the test. These data show a slight degradation of the MsS signal between the reference and the first 100 cycles (approximately 2 dB). However, after the first 100 cycles the data clearly show that the MsS signal does not significantly change even up to 1,000 cycles of approximately 24,000 psi compressive stress. Similar data are shown in Figure 11 with the nickel strip being remagnetized accept even after the first 100 cycles, there is no 2 dB difference after the remagnetization. Similar data are shown in Figure 12 for tension. This shows that all the data are within approximately 0.5 dB.

Additional compression data (estimated to be 24,000 psi) were taken on 0.010-inch-thick nickel strip bonded to aluminum using 5-minute epoxy. Data obtained after 500 cycles are shown in Figure 13, traces 4 and 5. This degradation of the MsS signal was expected.

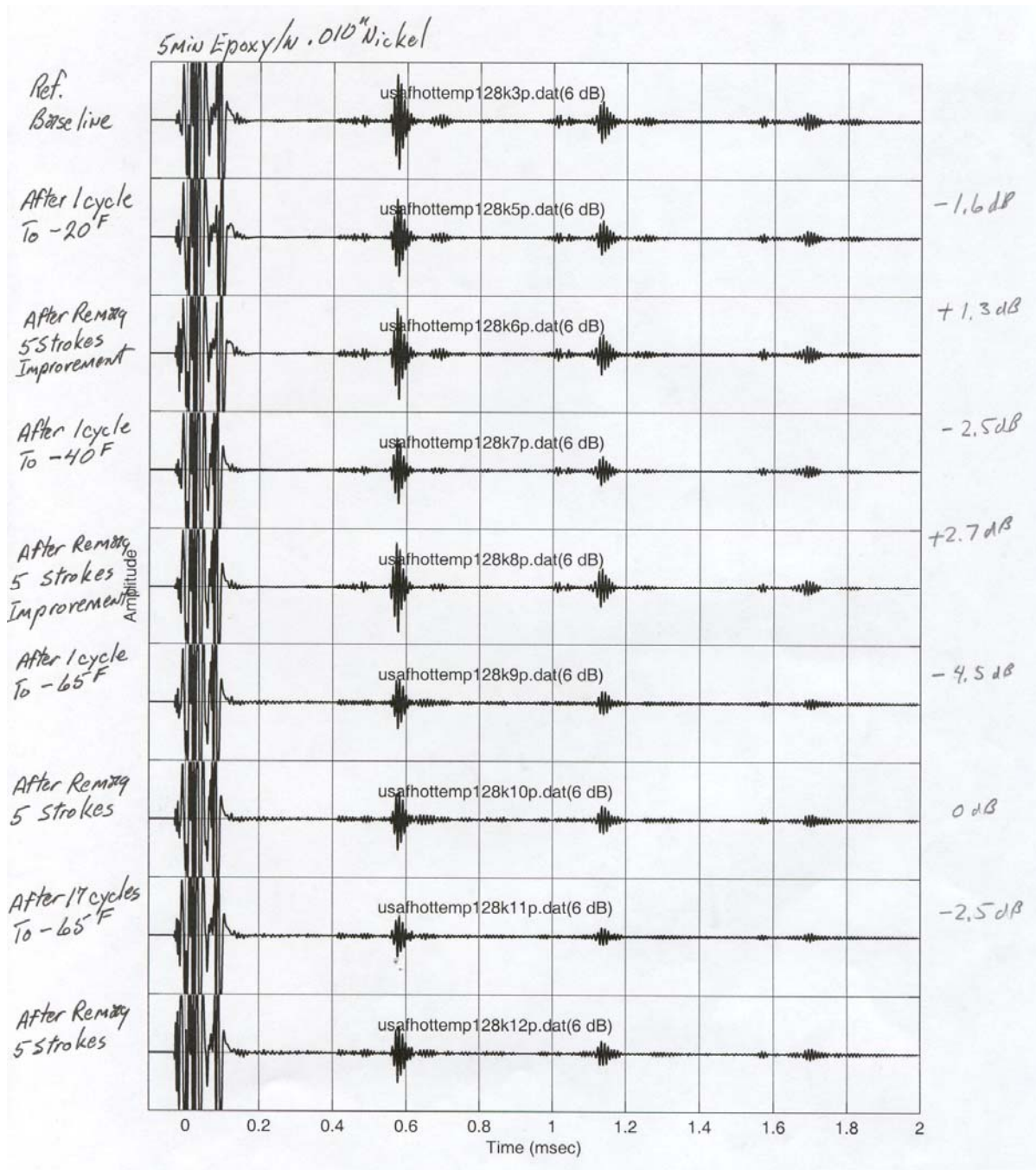


Figure 4. MsS data waveforms collected after various thermal cycles for nickel strip bonded to aluminum with 5-minute epoxy. The top waveform is the reference collected at approximately 70°F. The various waveforms are collected after different cycles (the temperature shown is the low temperature in the cycle which started at 70°F and returned to 70°F). The notation "after remag" denotes data collected after remagnetizing the nickel strip. From the data, it can be seen that the MsS signal begins to degrade after a thermal cycle of -40°F but can be brought back to reference level after remagnetization. However, after the -65°F cycle even remagnetization could not make the signal return.

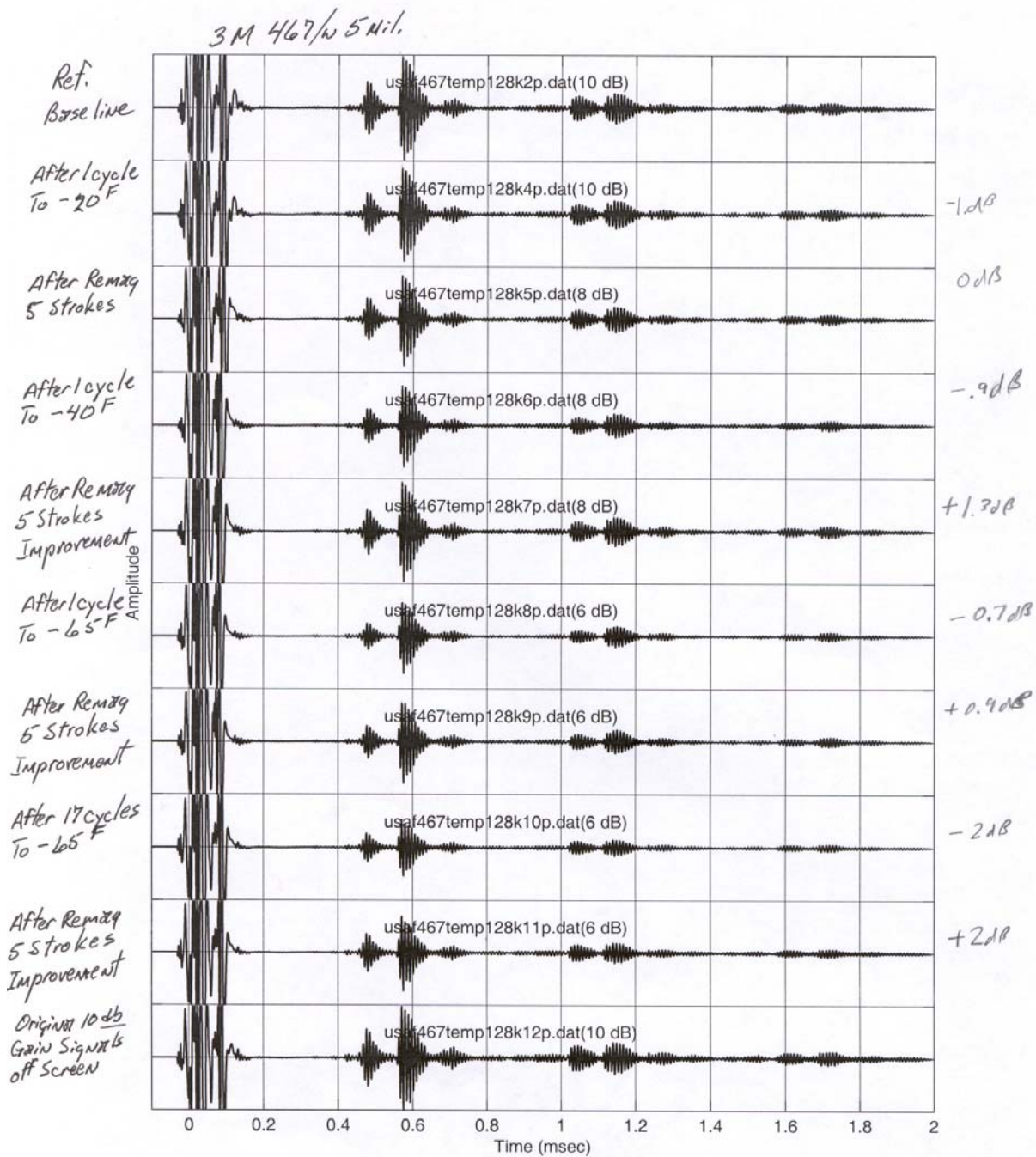


Figure 5. MsS data waveforms collected after various thermal cycles for nickel strip bonded to aluminum with 3M™467 adhesive. The top waveform is the reference collected at approximately 70°F. The various waveforms are collected after different cycles (the temperature shown is the low temperature in the cycle which started at 70°F and returned to 70°F). The notation "after remag" denotes data collected after remagnetizing the nickel strip. From the data, it can be seen that the MsS signal does not degrade down to -65°F even after 17 cycles.

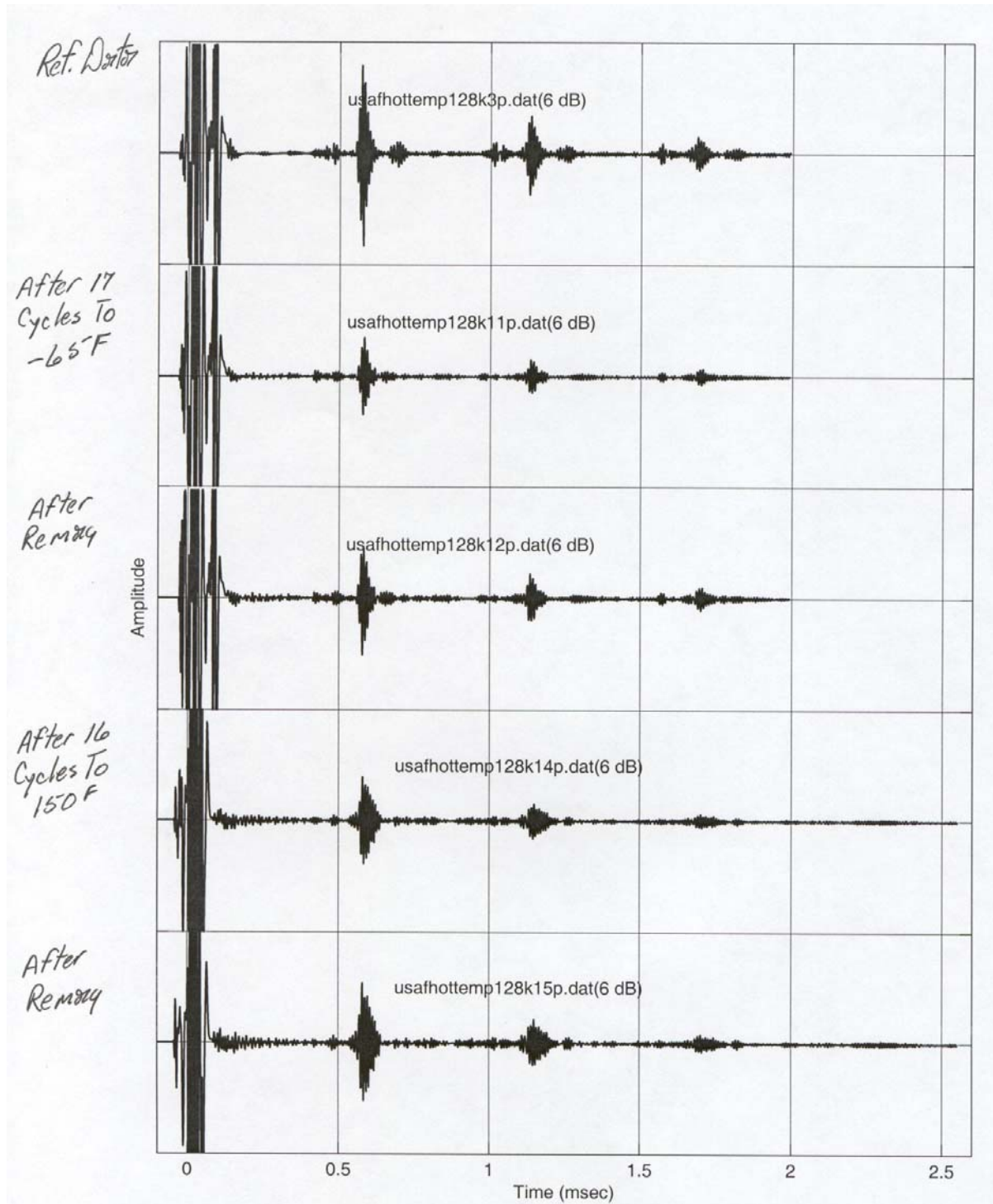


Figure 6. MsS data waveforms collected after various thermal cycles for nickel strip bonded to aluminum with 5-minute epoxy. The top waveform is the reference, the second is the waveform after 17 cycles down to -65°F, the third is after remagnetization, the fourth is after 16 cycles up to 150°F, and the final waveform is after remagnetization. The MsS signal is degraded.

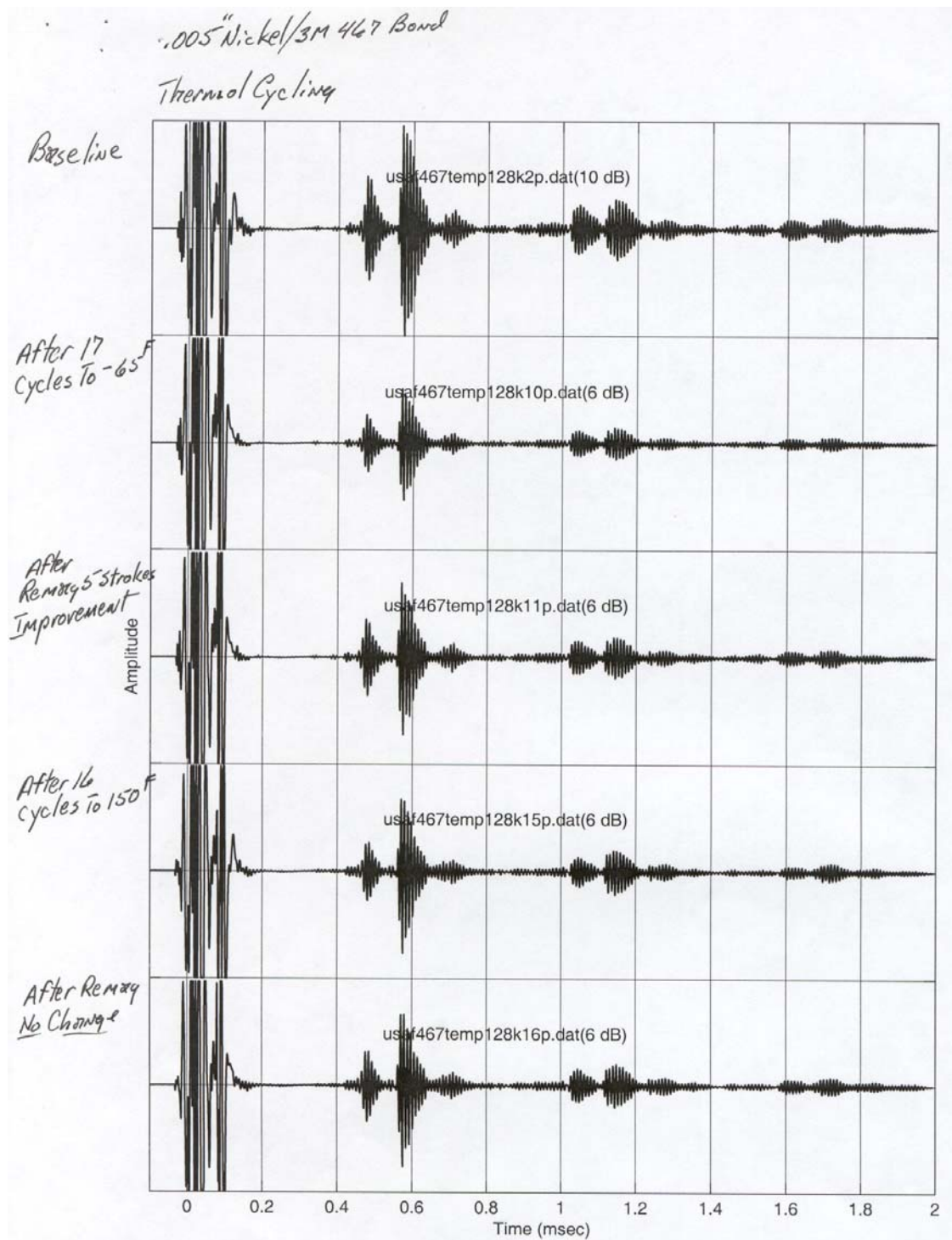


Figure 7. Mss data waveforms collected after various thermal cycles for nickel strip bonded to aluminum with 3M™467 adhesive. The top waveform is the reference, the second is the waveform after 17 cycles down to -65°F, the third is after remagnetization, the fourth is after 16 cycles up to 150°F, and the final waveform is after remagnetization. The Mss signal remains unchanged through the cycling.

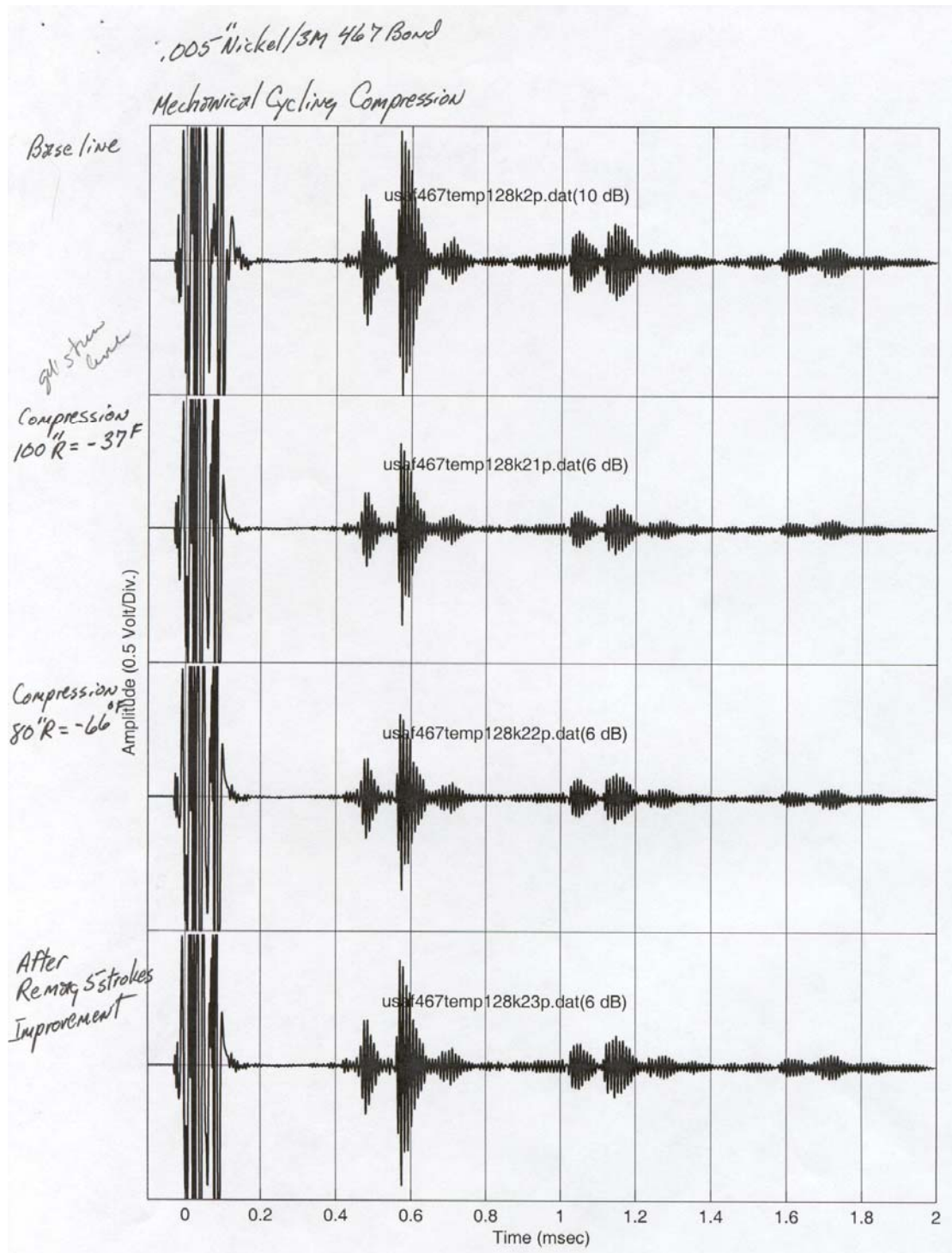


Figure 8. MsS data waveforms collected after various mechanical stresses produced by bending the aluminum plate over a mandrel for nickel strip bonded to the aluminum plate with 3M™467 adhesive. The top waveform is the reference; the second waveform is after one cycle at a compression equivalent to -37°F and -65°F. No degradation of the MsS signal was observed.

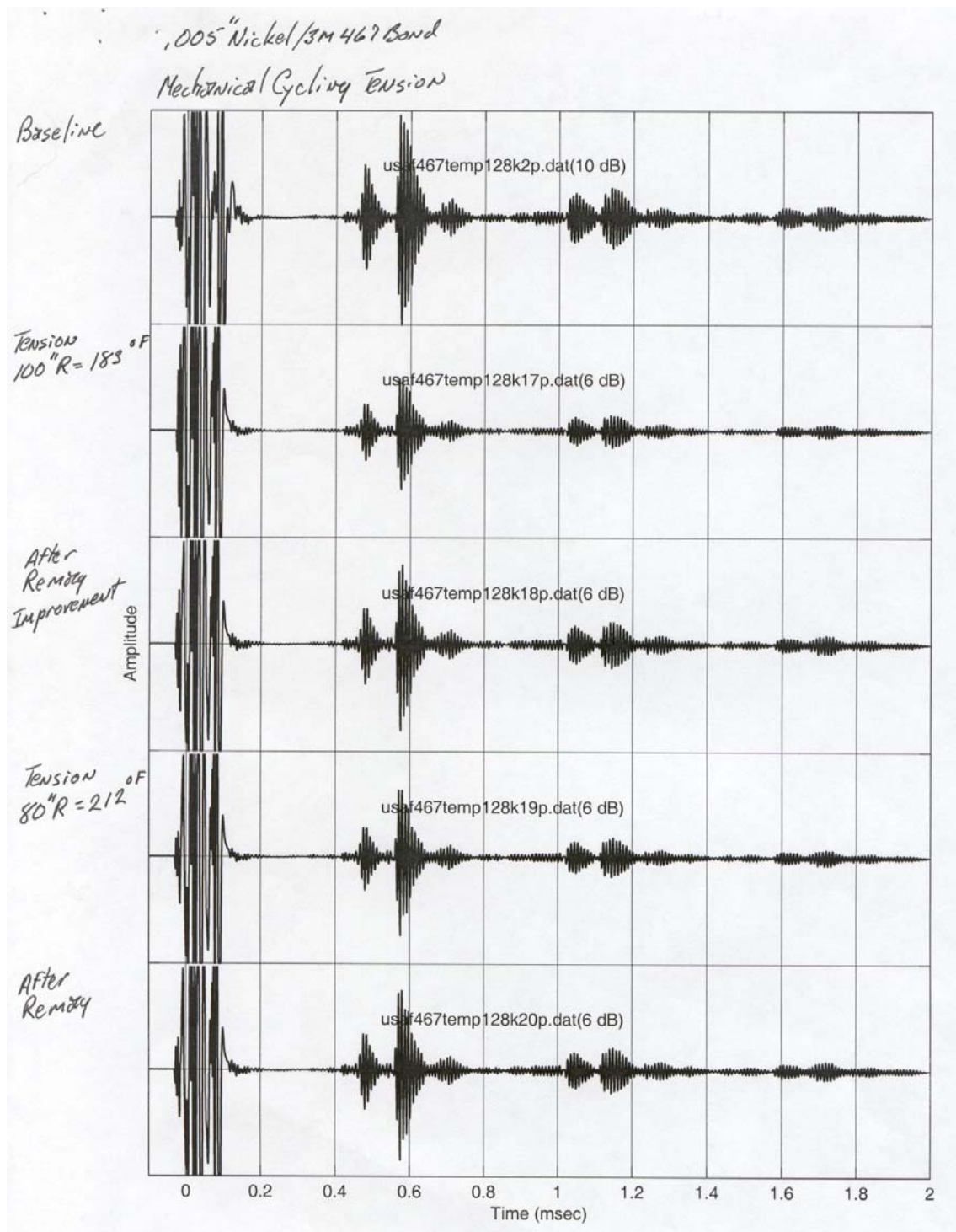


Figure 9. MsS data waveforms collected after various mechanical stresses produced by bending the aluminum plate over a mandrel for nickel strip bonded to the aluminum plate with 3M™467 adhesive. The top waveform is the reference; the second waveform is after one cycle at a tension equivalent to 183°F and 212°F. No degradation of the MsS signal was observed.

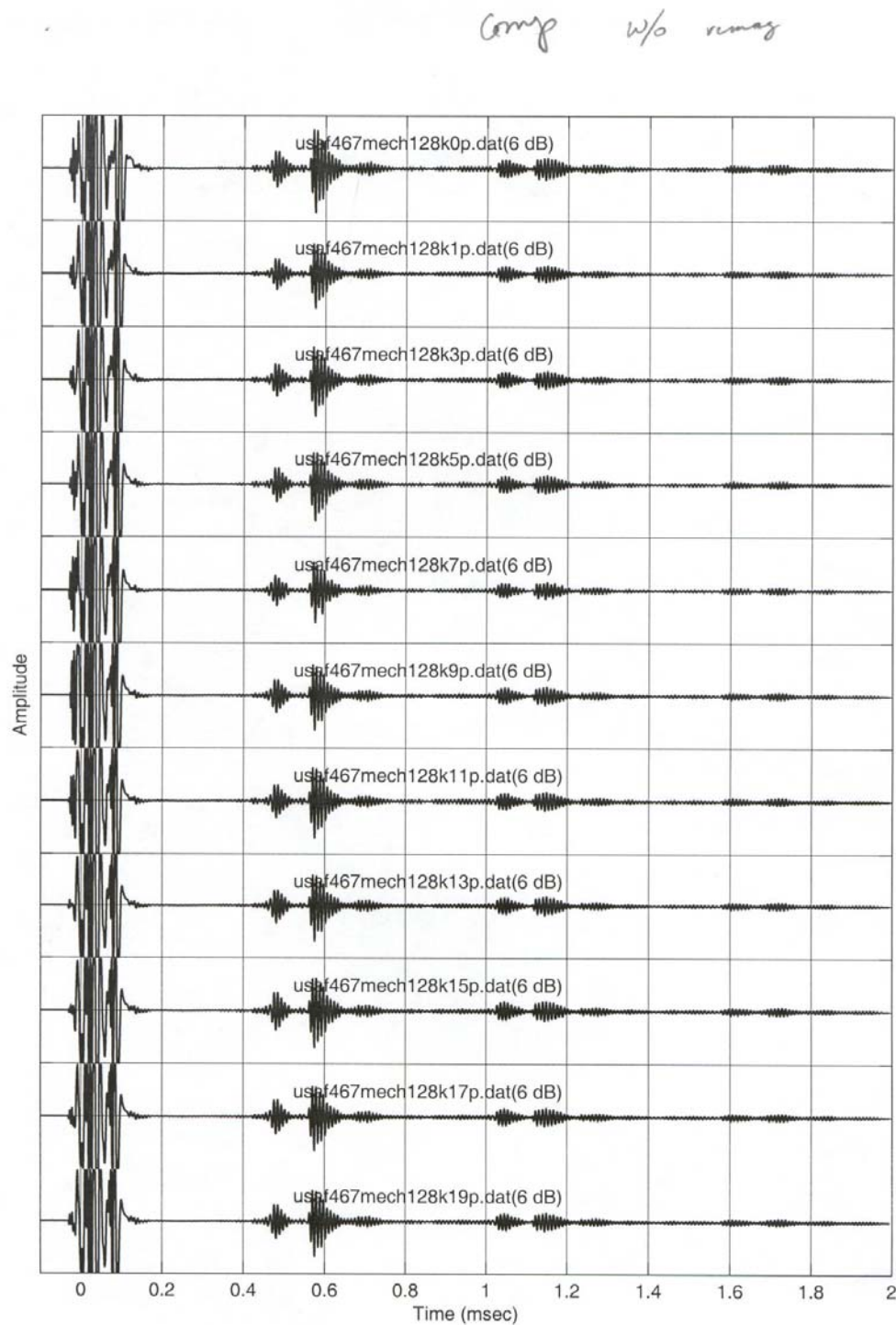


Figure 10. MsS data waveforms collected after large numbers of compression cycles equivalent to -65°F for nickel bonded to an aluminum plate with 3M™467 adhesive. The top waveform is the reference. Each successive waveform is after an additional 100 cycles of compression. Notice the waveform remains basically unchanged.

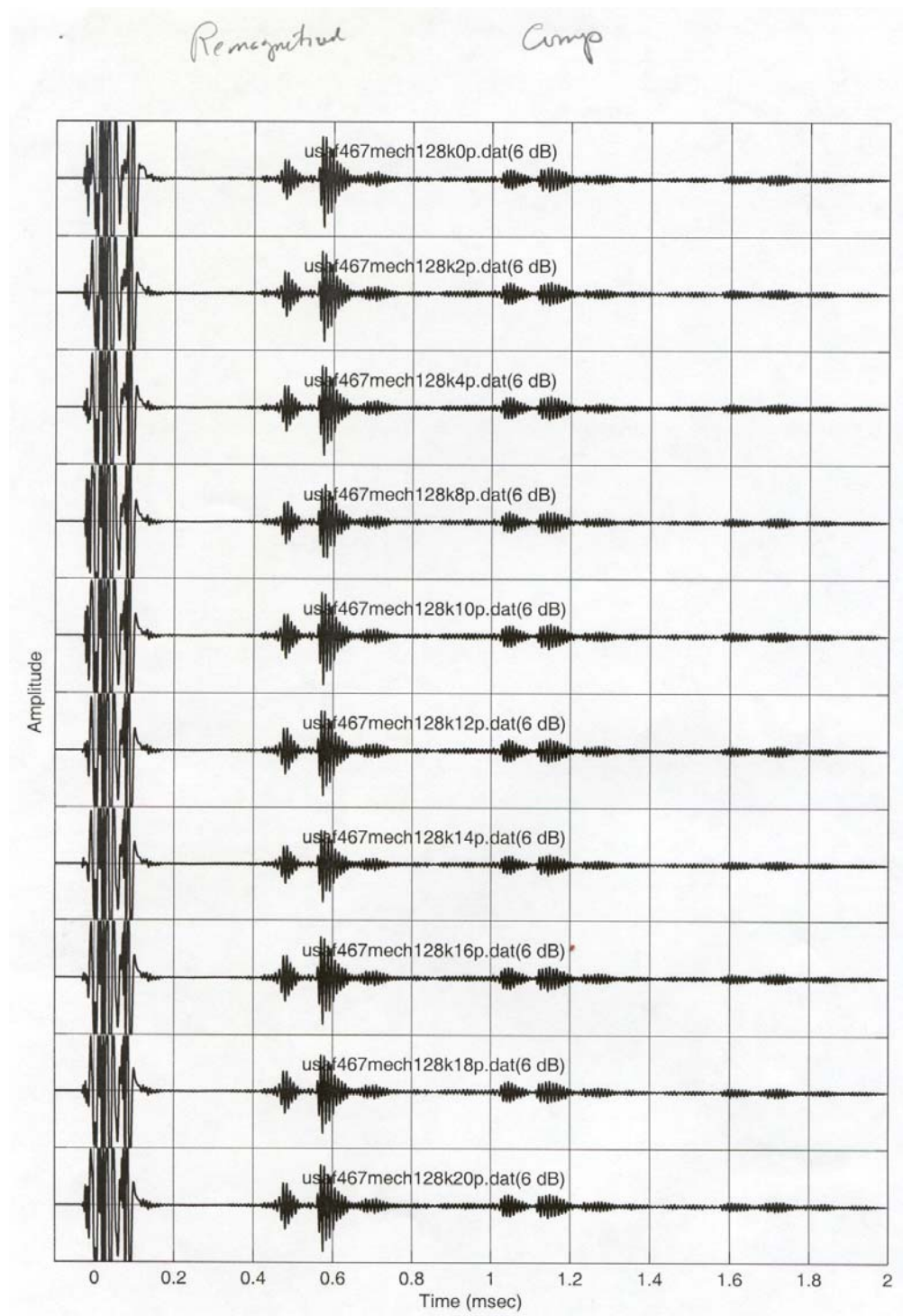


Figure 11. Same data as shown in Figure 10, but after remagnetization. Notice that the waveform remains basically unchanged.

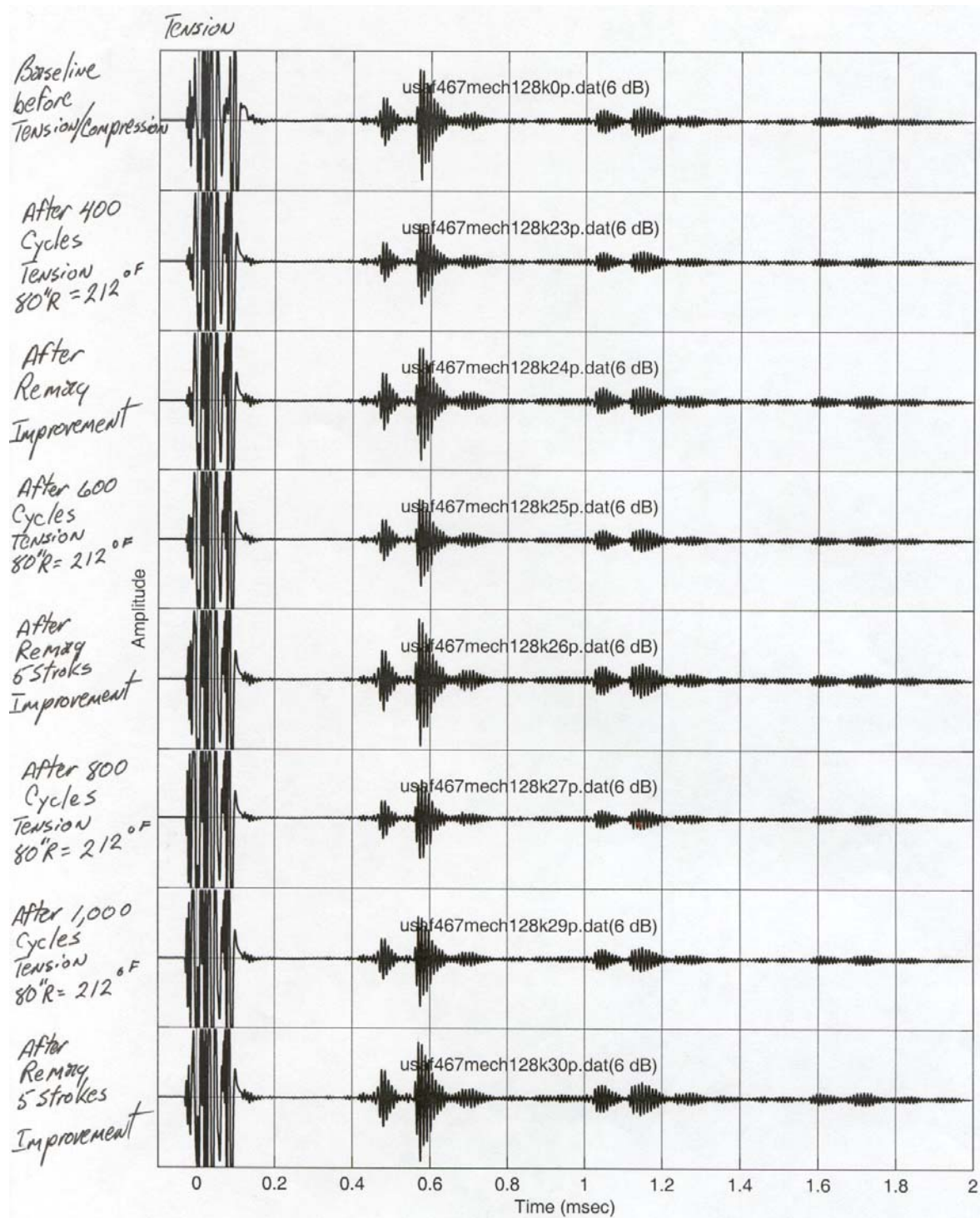


Figure 12. MsS data waveforms collected after large numbers of tension cycles equivalent to 212°F for nickel bonded to an aluminum plate with 3M™467 adhesive. The top waveform is the reference. Each successive waveform is after an additional 400, 600, 800, and 1,000 cycles of tension with and without remagnetization. Notice the waveform remains basically unchanged.

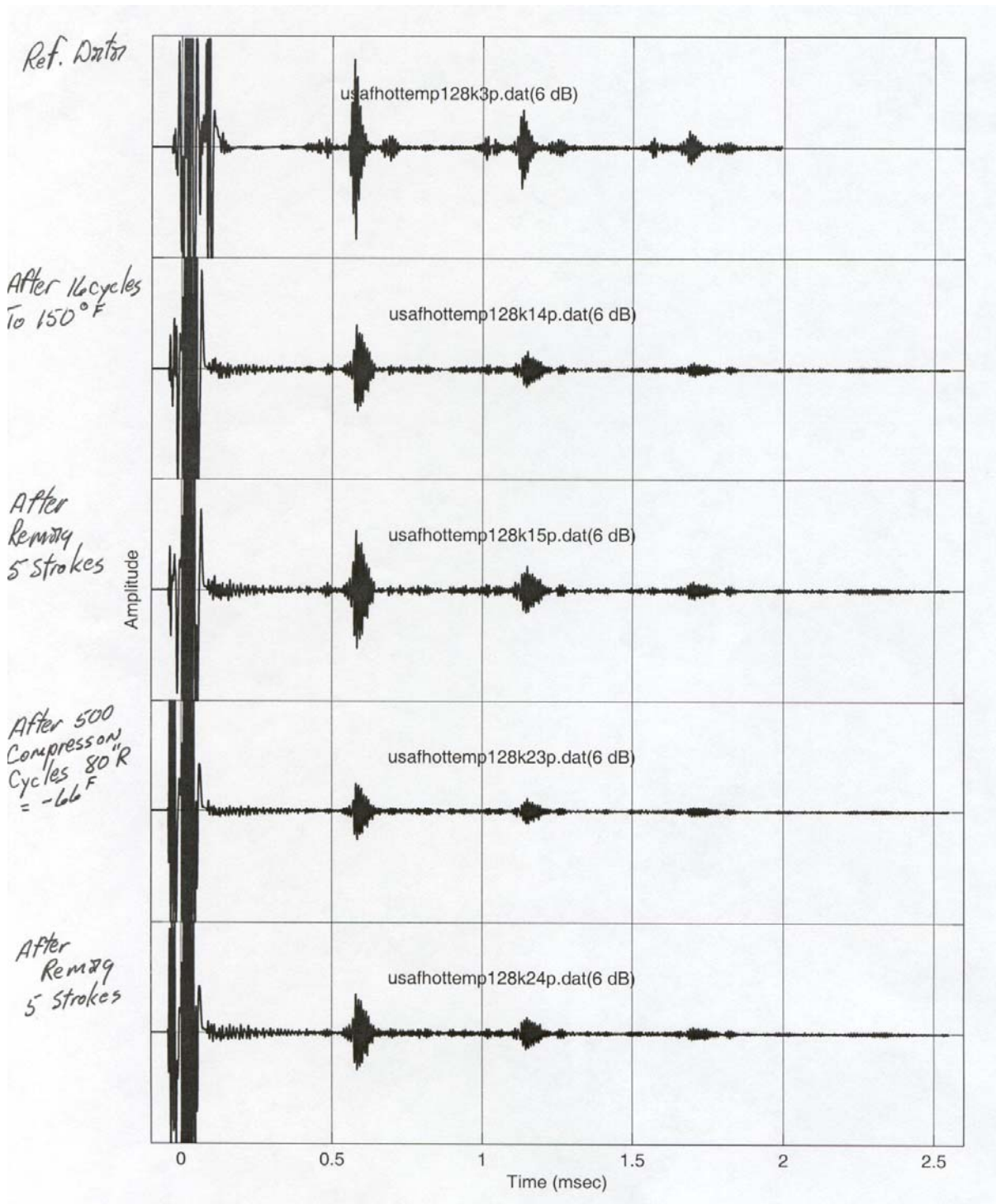


Figure 13. MsS data waveforms collected after various thermal cycles for nickel strip bonded to aluminum with 5-minute epoxy. The top waveform is the reference, the second is the waveform after 17 cycles down to 150°F, the third is after remagnetization, the fourth is after 500 cycles of compressive stress equivalent to -66°F, and the final waveform is after remagnetization. The MsS signal is degraded.

2.1.2.1 Temperature Related Stress Issues and How Magnetostrictive Properties Are Affected

To investigate the epoxy bond issue, two test samples were fabricated using aluminum plates with nickel strips bonded to them. To isolate temperature effects as being related to either extreme heat or extreme cold, each sample was placed separately in a temperature controlled environmental chamber. Before testing, the samples were instrumented with resistance strain gages on the nickel strips and on the adjacent aluminum to determine the magnitude of thermal expansion of each component and any other induced strains. The first sample was placed in the chamber and heated from 73°F (23°C) to 151°F (66°C) and the induced strains were allowed to stabilize. The sample temperature was maintained for 5 minutes and cooled back to 73°F. Strain was monitored at thirty-second intervals. The second sample was cooled from 73°F to -65°F (-54°C), held, and returned to room temperature. Upon completion of the thermal cycles, each sample was examined closely for any signs of significant bond failure of the epoxy. No evidence of bond failure was found in the heat-cycled sample. In fact, guided wave data were taken again on this sample and matched well with the baseline, indicating that the heat had not deteriorated the MsS capability of the strip. However, when attempting to take data on the cooled sample, the signal showed a complete absence of the reflections found in the baseline. This indicated that cooling of the samples was responsible solely for the loss of performance of the nickel strip. It was hypothesized that this complication may be due to the mismatch in the coefficients of thermal expansion (CTE) between aluminum and nickel, $23.5 \times 10^6 / ^\circ\text{C}$ and $13.3 \times 10^6 / ^\circ\text{C}$, respectively. This could further be used to explain why the nickel performance on steel pipe is recoverable, because the CTE of steel is $12.1 \times 10^6 / ^\circ\text{C}$ (as previously reported). However, it was not certain whether this mismatch caused an undesirable condition in the nickel, or if it caused failure in the epoxy bond.

The strain history data for each sample are shown in Figure 14. For the cooled sample, there is a noticeable jog in the strain data at approximately 11 minutes into the test and at a compressive strain of 770 $\mu\text{in/in}$. This could happen because under compression, the nickel strip will attempt to bow away from the aluminum plate with only the epoxy keeping it bonded. The sudden drop in strain suggests that at some locations along the strip length, there were localized failure of the bonding. However, the strain is well behaved following the jog, suggesting that there is still considerable bonding of the epoxy, sufficient to maintain a compressive strain on the nickel throughout the remainder of the test. At return to room temperature, the nickel strain returns almost to 0, indicating that there is no significant residual stress in the strip. While it appears from the strain data that there was some slippage of the epoxy bond, it does not seem sufficient to explain the complete loss of signal after cooling, and the inability of recovering the signal with remagnetization of the nickel strip. Therefore, based on this experiment, the epoxy bond appeared not to be the primary cause of the problem.

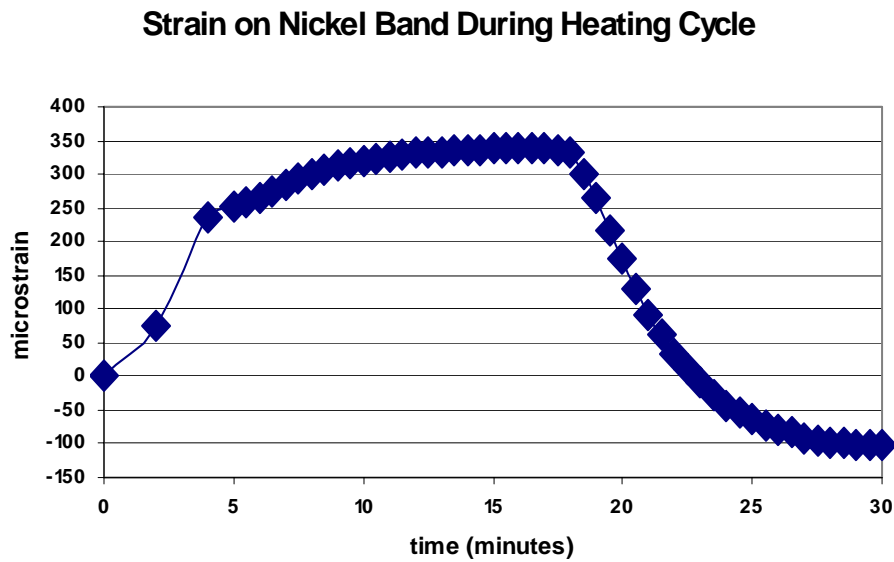
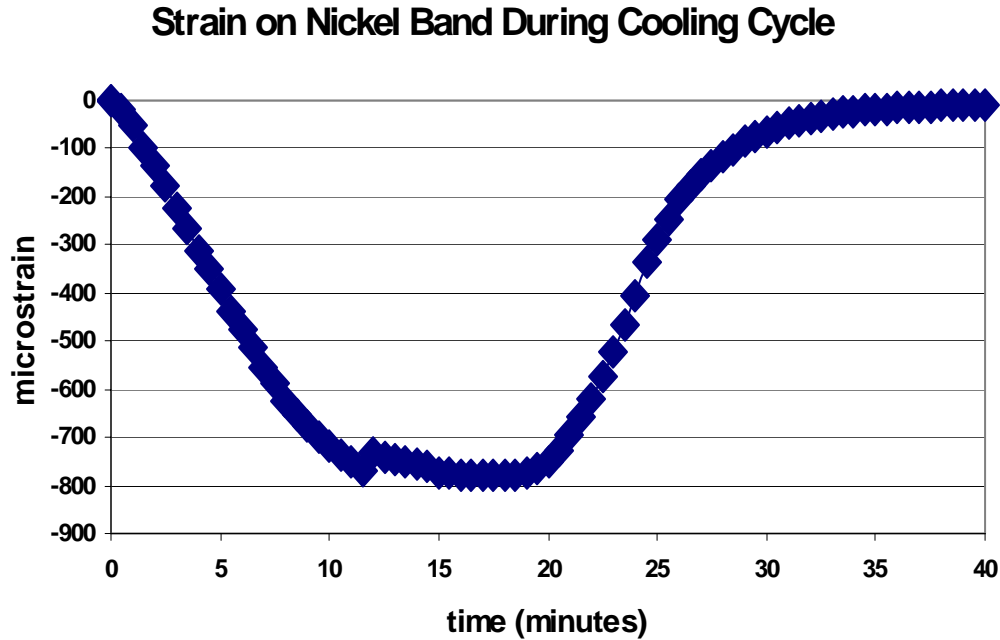


Figure 14. Strain histories for the cooled and heated samples, respectively. The cooling range was from 73°F (23°C) to -65°F (-54°C), and the heating range was from 73°F (23°C) to 151°F (66°C).

This led to the investigation of the change in magnetic properties of the nickel strip as a function of the temperature cycling. Perhaps the most plausible reason for loss of the nickel strip effectiveness after cooling is that of the effect of thermally induced strains on the orientation of the magnetic domains in the nickel strip. Interactions between domains and mechanical stresses are a complex issue, but a simple model may explain the phenomenon being observed in this study. The magnetostrictive process requires that an alternating magnetic field be applied in the presence of a larger bias magnetic field. When the alternating and bias fields are specifically oriented, mechanical strain is produced along the desired material axis and, thus, guided wave energy is supplied to the inspected material. From

this study, it is proposed that the heating cycle does not affect the applied bias magnetic field on the nickel, while the cooling cycle considerably reduces the bias field. Figure 15 depicts the theorized orientation of the nickel's magnetic domains when the nickel strip is initially bonded to the aluminum panel before magnetizing the nickel.

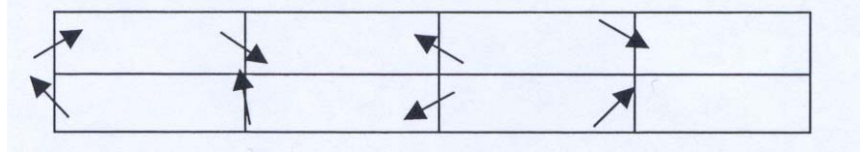


Figure 15. Simplified depiction of magnetic domains in the nickel before application of the biasing magnetic field. The arrows represent the localized magnetic orientation of each domain.

As shown in Figure 15, there is a random orientation of domains, indicating no net permanent magnetization of the nickel strip. However, when the bias field is applied by swiping the strip with a permanent magnet, the domains are organized as shown in Figure 16. The domains in nickel respond to the application of mechanical stresses. In bulk sections, the application of a tensile stress will cause the domains to effectively orient themselves perpendicular to the stress axis. However, it has been shown that the opposite may be true [2-5] in thin films. The application of tensile stress orients the domains parallel to the stress axis. As shown in the strain time history above, the heated sample undergoes tensile stresses during heating and, thus, the domains are likely to remain longitudinally oriented during the heating cycle. This could potentially explain why there seems to be no effect on signal quality for the heated sample. In contrast, nickel film domain orientation may be forced perpendicular to the stress axis when a compressive stress is applied, as would be the case in the cooled sample. Figure 17 illustrates this possibility.

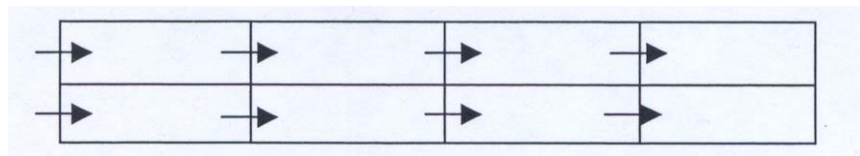


Figure 16. Illustration showing that all the domains have a common orientation, thus, the nickel strip has been magnetized with a field along its longitudinal axis

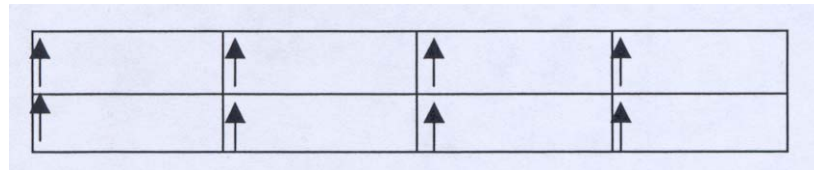


Figure 17. Theorized orientation of the nickel domains after cooling cycle when compressive stress is applied. All are oriented perpendicular to the stress axis.

With a perpendicular domain orientation, there effectively would be no net bias magnetization on the nickel strip in the desired longitudinal direction for magnetostriction. Therefore, no mechanical energy could be produced in the desired direction using the strip. This would further explain the inability for remagnetization of the strip in the longitudinal direction because although a small permanent magnet was sufficient to supply the energy needed to orient the domains from a previously random state, the same magnet is not enough to rotate all domain orientations ninety degrees. A further consideration is that there is a definite effect of mechanical stress on magnetic permeability. Permeability is the resulting magnetization in a material from an applied magnetic field. It is possible that the cooling cycle reduces the permeability of the nickel, thus making it harder to magnetize using the same applied field.

From this study, several approaches may enable the nickel strip to be subjected to extreme temperature deviations without sacrificing performance for such applications as airplane skins. Preliminarily, it appears that the most direct solutions will deal with minimizing or eliminating compressive stress on the nickel either by modifying the geometry of the nickel strip or by using a new bonding material.

One approach investigated was to segment the nickel strip before or after bonding to the aluminum. Rather than applying a continuous strip of nickel to the sample aluminum pipe, the strip was cut at one to two inch intervals so that there would be essentially several transmitter elements. This approach should minimize the flexure stress of the nickel strip bowing away from the surface of the pipe during the compressional stresses of the cold cycle.

Another approach to minimize the compressive stresses applied to the nickel strip during cold temperature excursions is to use a bonding agent that can tolerate shear stress. Epoxy tends to be very rigid and thus transmits nearly all of the thermal contraction strain of the aluminum to the nickel. If a bonding agent (such as 3M™467) could be found that will minimize the amount of transmitted strain at cold extremes, while retaining its ability to transmit mechanical strain at room temperature, this would greatly reduce the stress effects on the nickel.

2.1.2.2 Discussion of Stress Effect Experiments

Experiments were designed to more carefully evaluate effects of both compressive and tensile stress and sensor materials thickness. The maximum stress levels were approximately 24,000 psi. In addition, another material was also investigated. All experimental work was performed on aluminum test samples that were 1/8 inch thick plates consisted that were 34 inches long by 12 inches wide. Near one end of the each plate a sensor strip, 7 to 8 inches in length by 1 inch in width was bonded. The strips had two thicknesses, 0.005 inch and 0.010 inch. The strips were bonded with a 5-minute epoxy to the aluminum with adequate preparation of the bonded surfaces to ensure a durable bond. To provide the initial required bias magnetic field to the strips, a small permanent magnet was swiped along the length of the bonded strip several times.

Key to this investigation was the understanding that a permanently mounted sensor would experience both tensile and compressive stress cycles due to temperature cycling of the aircraft panel and in-flight aerodynamic stresses. Assuming that the most severe stresses would be thermally induced, an experimental method was developed to

simulate thermal strains on the sensors using mechanical means. Due to the significant difference in thermal expansion coefficients of aluminum and the nickel sensor material, the strain on a sensor strip that experiences a change in temperature from the temperature at which it was bonded can be predicted by the following relation:

$$\varepsilon = \Delta\alpha \cdot \Delta T,$$

where ε is the induced strain in inches per inch, $\Delta\alpha$ is the difference in expansion coefficients (for aluminum and nickel, $\alpha_{Al} - \alpha_{Ni} = 23.5 \times 10^{-6} / ^\circ\text{C} - 13.3 \times 10^{-6} / ^\circ\text{C} = 1.02 \times 10^{-5} / ^\circ\text{C}$), and ΔT is the difference between the environment temperature and the temperature at the time of bonding of the sensor. Previous thermal cycling experiments were conducted on nickel sensors that were bonded onto the aluminum plate at a temperature of approximately 73°F (23°C) for thermal extremes of 150°F (66°C) and -65°F (-54°F). This induced strains on a nickel sensor of approximately +439 micro-inches per inch (yielding a calculated stress of approximately 13,200 psi) and -785 micro-inches per inch (yielding a calculated stress of approximately 24,000 psi), respectively, where a positive number indicates tensile strain while negative indicates compressive strain. Equivalent strains can be produced by inducing a curvature on the aluminum plate by adhering to the following relation:

$$R = \frac{c}{\Delta\alpha \cdot \Delta T},$$

where R is the induced radius of curvature measured to the mid-thickness of the aluminum plate, and c is the half-thickness of the plate. To achieve a simulated hot cycle and a cold cycle, the instrumented aluminum plates were forced to conform instantaneously to wooden mandrels of fixed radii and then released back to a zero strain condition. The fact that this occurs instantaneously may tend to better simulate thermal shock than a normal thermal cycle.

To simulate a heating cycle the sensor side of the plate was external to the curvature (convex), while for a cold cycle the sensor side was internal (concave). This method of thermal strain simulation was accepted after the performance of mechanically stressed test samples closely matched those of samples cycles in an environmental test chamber of changing temperature. In most cases during these experiments, signals were taken at a zero strain condition following a strain cycle, but little data was taken while under significant stress due to the complications in coupling the electromagnetic coils to a curved surface. This was considered to be acceptable because of the assumption that most monitoring testing would be done under maintenance depot temperature conditions.

Two sensor thicknesses, 0.005 inch and 0.010 inch, were used to investigate the sensitivity of each to applied mechanical stresses. During the course of the experiments, it was decided that 0.010 inch thick material would be used exclusively because of availability of this gage in alternate materials to nickel.

One additional material was chosen for investigation that has a higher magnetostrictive saturation strain than nickel, called Permendur 49. Its composition is 49% iron, 49% cobalt, and 2% vanadium by weight. Its maximum magnetostrictive strain is reported as approximately +70 microinch per inch compared to -40 microinch per inch for nickel. This sign change indicates that under an identical magnetic field, one material would expand while the other would contract along any given direction. In these tests, 0.010 inch-thick

nickel and Permendur 49 were bonded to aluminum test plates and magnetized in identical fashion.

2.1.2.3 *Results Obtained for the Stress Measurement Effects*

It was observed that the strain history developed by the mechanical stressing of the test samples was extremely important to the performance of the sensors. It was shown numerous times during the experiments that any data taken at zero strain after either a tension or compression cycle that exceeded approximately 20,000 psi, or a succession of each, yielded signal strength considerably less than that of a sample that was not cycled.

The Permendur sensors exhibited a similar behavior (with the exception that the tensile stress affected the Permendur more than compressive stresses). This was expected because it has a positive magnetostrictive coefficient while nickel has a negative magnetostrictive coefficient. This suggests a magnetomechanical phenomenon related to domain orientation under stress. However the Permendur's signal strength was much less than that of the nickel, even in samples that had not been cycled. This will be discussed in further detail below.

As mentioned above, the Permendur-based sensors exhibited lower signal strengths than the nickel. Initially, it was believed that selection of a material with maximal magnetostrictive strain would help alleviate any problems caused by stress cycles. However, after learning of the poor performance of the Permendur, literature was reviewed to better understand the observed behavior [6] suggests that the coupling of magnetic energy to mechanical energy in an elastic material with applied magnetostrictive sensor is governed by the following proportional relation:

$$h_{\lambda} \propto \frac{\partial \lambda}{\partial M},$$

where h_{λ} is a coupling effectiveness constant, λ is the linear magnetostriction, and M is the magnetization of the sensor material in amperes per meter. However, the chain rule of derivatives yields,

$$\frac{\partial \lambda}{\partial M} = \frac{\partial \lambda}{\partial H} \cdot \frac{\partial H}{\partial M},$$

where H is the applied magnetic field in amperes per meter. By definition, the susceptibility, χ , of a material is the derivative of its magnetization with respect to applied magnetic field. Thus,

$$h_{\lambda} \propto \frac{\partial \lambda}{\partial H} \cdot \frac{1}{\chi},$$

which shows that the effectiveness of coupling of a ferromagnetic material to an elastic material is proportional to its linear magnetostriction and inversely proportional to its susceptibility. This helps explain why annealed Permendur (λ approximately 70 microstrain and χ approximately 800) has less signal strength than nickel ($\lambda = -40$ microstrain, and χ of 110). Thus even though the magnetostriction of Permendur is almost twice that of nickel, the permeability of Permendur is about 8 times higher than the permeability of nickel. Therefore, the effectiveness of the Permendur to produce guided waves approximately 4 times less than the effectiveness of nickel.

A more robust derivation of the magnetostrictive coefficient and how to determine which magnetostrictive material might be the best for a given application is provided in Appendix 2.

After learning of the difficulty in maintaining repeatable signal strength after various strain history scenarios, a different approach to magnetization of the nickel sensors was briefly examined. After a compressive stress cycle was applied to a test sample the signal was severely degraded and repeated attempts to remagnetization with a small permanent magnet did not improve the signal. A neodymium-iron-boron permanent magnet (strength not measured but observed to be much stronger than the small magnet) was put in position on the test sample to maintain the previously used flux line direction. Data taken with the large resulting magnetic field in place showed a similar signal strength before and after stressing. Removal of the magnet again yielded a severely degraded signal similar in strength to the signal before the large magnet was applied. This suggests that the ability of the nickel to retain and hold a bias magnetic field is hindered as it experiences stress cycles. Furthermore, this may make the case for future work focusing on application of a known external bias field to produce repeatable data in light of the stress conditions that the sensor will experience.

One approach might be the use of an externally applied bias magnetic field to the nickel. Preliminary test indicate that this approach appears promising for attaining repeatable signal strengths after in-flight stress environments. The bias field could be applied using a permanent magnet in a fixture, or more practically, an electromagnet that is either applied at the time of inspection or permanently with the sensor on the aircraft.

The level of statistical significance of the external bias field effects versus the strain history effects was not measured. To answer the question definitively whether bias field application can eliminate the strain problem, additional testing was conducted.

An experimental apparatus was set up to immerse samples of nickel bonded to aluminum in a controllable magnetic field, H , using a solenoid driven with a function generator and amplifier. The induced magnetic flux, B , was monitored during the testing using a coil directly surrounding the samples and connected to a signal integrator. A sinusoidal H field of 0.2 Hz frequency and maximum magnitude of approximately 3500 amperes per meter was applied to each sample being tested. Following four complete cycles, the solenoid was driven with a decaying sinusoidal input to render the samples demagnetized after the completion of the run. Comparison of each test sample was performed by analysis of the initial magnetization curve before magnetic saturation and the beginning of hysteresis behavior. Magnetic permeability is equal to the slope of the magnetization curve. Therefore, the slopes of the curves between approximately 500 and 1500 A/m were calculated and used as a test statistic to compare the results of each test run.

To parallel the past work done with nickel sensors bonded to an aluminum plate, five test samples were fabricated that consisted of a 0.375-inch wide strip of 0.010-inch gage nickel strip bonded with epoxy to a 0.125-inch thick aluminum strip of the same width as the nickel. The length of the nickel strip was three inches and was centered longitudinally along a face of the twelve-inch long aluminum strip. Baseline magnetic data were collected for each test sample immediately following fabrication, then each sample was subjected to bending over a wood mandrel and releasing to induce tensile or compressive strain histories in the samples. Following application of strain, the samples' magnetic behavior was again measured using the experimental setup.

The magnetization curves for the samples immediately after fabrication showed very little variation, which indicates that the state of the sensors initially is fairly independent of any deviance occurring during application of the nickel sensors. Figure 18 is a plot of baseline magnetization curves of the five test samples.

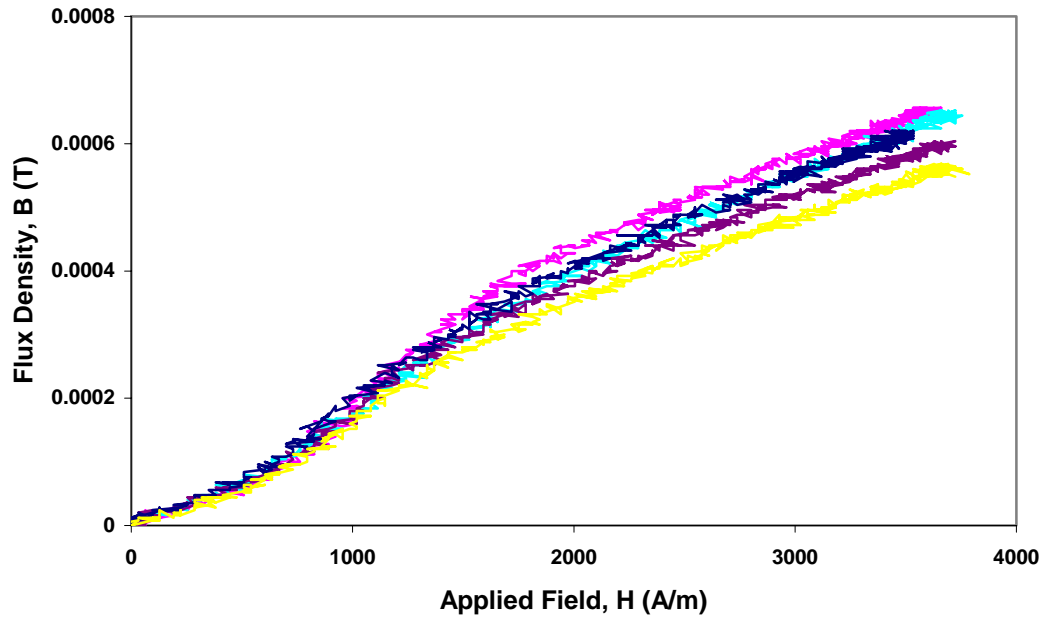


Figure 18. Magnetization curves of five test samples immediately after fabrication

However, when magnetic behavior was measured on samples after undergoing a tensile strain cycle, the magnetization curve shifted up. Contrary to this, a sample having undergone a compressive strain cycle showed a downshift in the magnetization curve. These are shown in Figure 19.

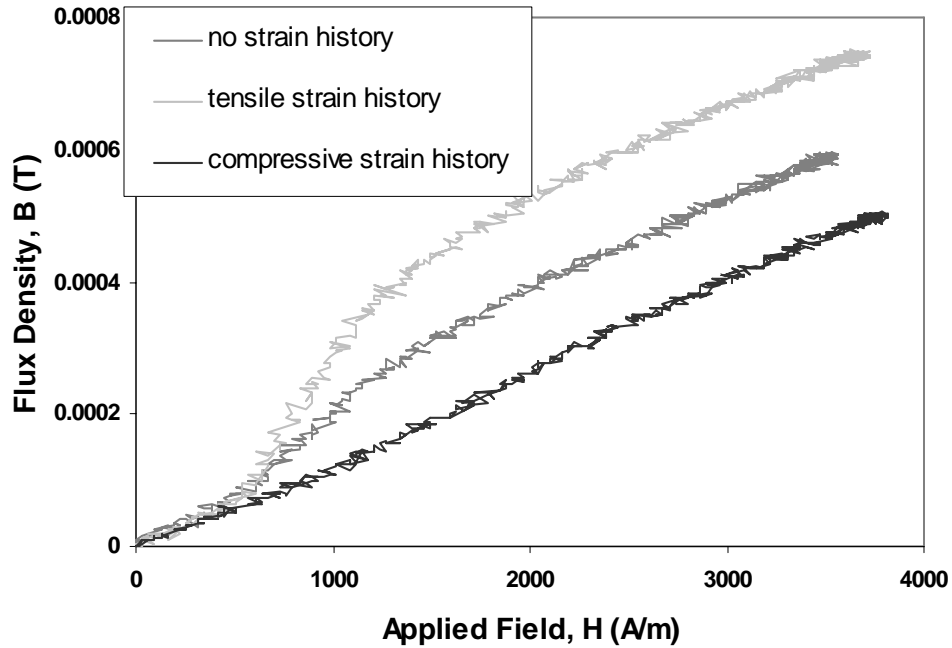


Figure 19. Change in magnetization curves caused by strain history

However, when magnetic behavior was measured on samples after undergoing a tensile strain cycle, the magnetization curve shifted up. Contrary to this, a sample having undergone a compressive strain cycle showed a downshift in the magnetization curve. These are shown in Figure 20.

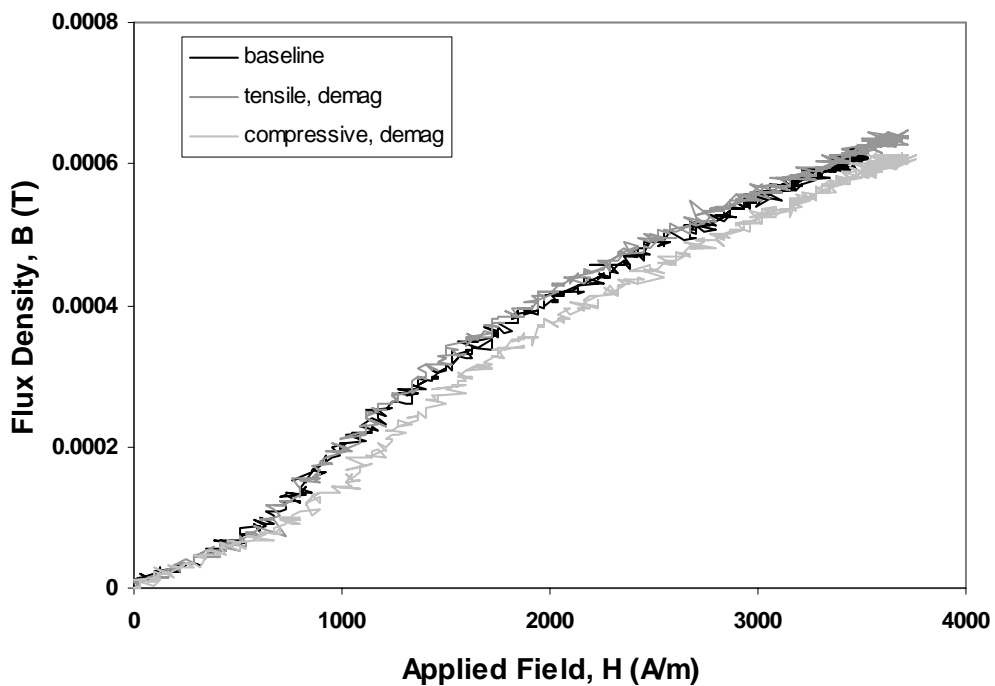


Figure 20. Behavior of previously strained samples after demagnetization versus baseline

Each test sample underwent a demagnetization following collection of the magnetic data. After demagnetization of the samples with either tensile or compressive strain history, magnetization curves were acquired again immediately to note any changes. Figure 20 shows that demagnetization of the previously strained samples tends to return their magnetization curves to the baseline levels.

The results from Figure 20 show that previously compressed or tensioned nickel sensors can potentially be returned to their original performance by the use of a demagnetization process just before acquisition of the inspection data.

To determine the relevance of the magnetic measurement results, additional testing was performed using the nickel strip sensors bonded to the large aluminum panels. An electromagnet driven by a function generator and amplifier was used to demagnetize the bonded nickel strip. This was accomplished by applying a decaying sinusoidal magnetic field across the strips longitudinally. An active magnetic field was then applied across the strip using a current of 1 ampere through the electromagnet's coils. A guided wave was then induced in the aluminum plate using the magnetostrictive inspection instrumentation while the electromagnet was energized across the nickel. A baseline signal was recorded. Following this, the magnetic field was removed and the nickel sensor was subjected to a mechanical strain simulating a temperature drop of 139°F (77°C) and then returned to a zero strain condition. The nickel strip bonded to the aluminum was demagnetized using the electromagnet. Inspection data was again taken with an active field applied to the nickel during acquisition. The field strength was equivalent to the baseline field strength, 1 ampere. The strength of a reference reflection in the signal was within 0.5 decibels of the baseline signal strength. This is well within the observed experimental variation of the inspection setup. Figure 21 shows the inspection data before and after compressive strain was applied.

From these observations it appears that application of an active bias magnetic field during the inspection, coupled with demagnetization of the sensor before inspection, has the potential to minimize or eliminate the effects of strain history on sensor performance. It is likely that a hand-held or stand-mount fixture incorporating an electromagnet and power supply could be used at the sensor location to achieve these two requirements. Further development of this approach would involve accurate measurement of the H field being produced by the magnetostrictive inspection system coils. Furthermore, the application of the bias magnetic field would need tighter control to ensure repeatable results. This might involve the use of a feedback control approach using a hall probe and electronics to precisely control the current applied to the electromagnet's coils during inspection.

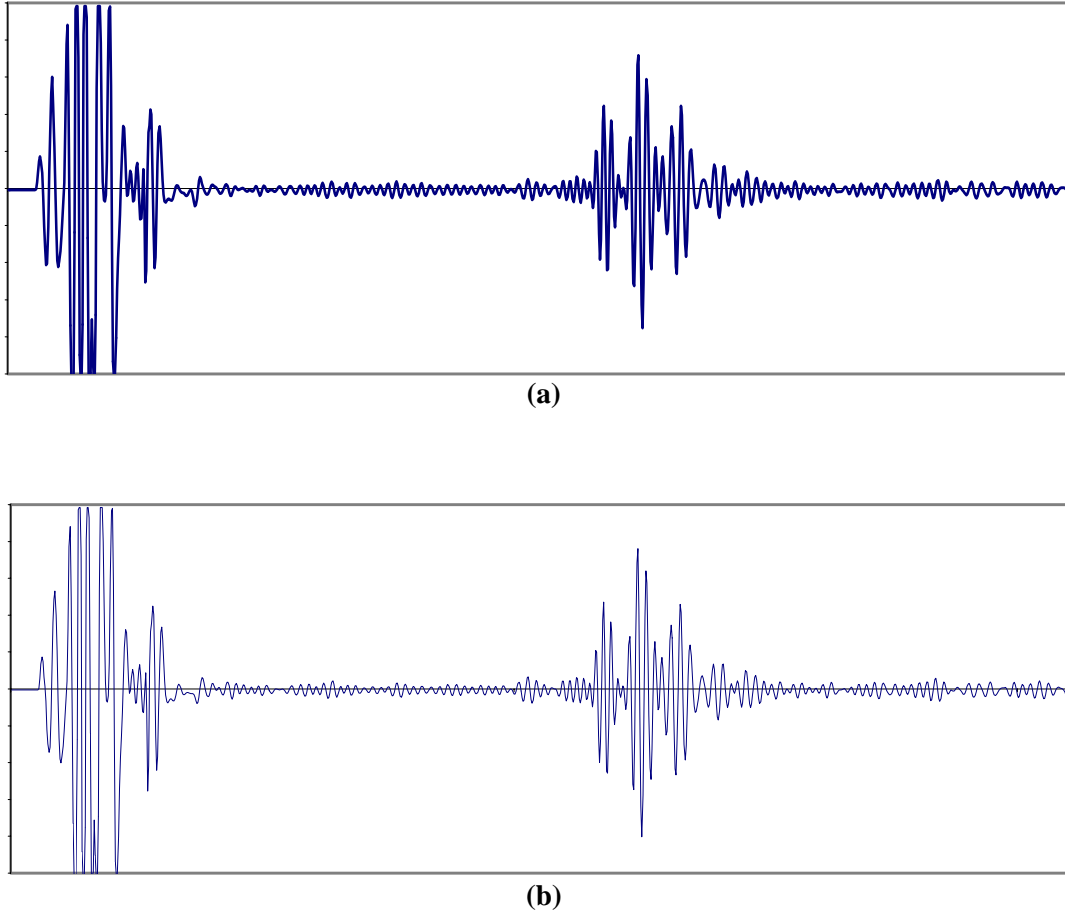


Figure 21. Waveforms at (a) baseline, and (b) after strain and demagnetization of nickel sensor (waveforms are basically the same)

2.1.2.4 Further Investigations on the Behavior of Nickel Strip During Stressing

Based on the results of previous work, three concepts were investigated in this study to eliminate or minimize the deleterious effects of thermal cycling: (1) a 0.005-inch-thick strip with 45-degree slits cut every 2 inches on center, (2) a 0.005-inch-thick strip with slits perpendicular to the strips long edges cut every 2 inches, and (3) a continuous strip of 0.010-inch-thick nickel strip.

Test samples were fabricated using 8 inch x 1 inch nickel strips bonded with 5-minute curing epoxy bonded to 1/8-inch-thick aluminum panels. The aluminum and nickel strips were cleaned well before applying the epoxy. Baseline data were taken for all three sensor types. In the case of the 0.005-inch-thick strips, data were taken before and after placing the slits, and it was verified that there was little effect on the signal caused by placement of the slits. The test samples were then cycled mechanically to simulate thermal stress effects. Initially, each panel was stressed over a 60-inch radius wooden mandrel to simulate an aluminum panel temperature of 155°F, then the same panel was inverted and placed over a 30-inch radius

mandrel to simulate the compression on the nickel at -84°F . Following one simulated temperature cycle, data were taken on all three sensors for comparison to the baseline. Both 0.005-inch-thick strip sensors showed almost complete loss of signal amplitude after the stress cycle. It was hypothesized that the use of the slits would lower the compressive strains applied to the strips during simulated cooling, but from these results the slits appear to provide no benefit. Inspection of the baseline data from the 0.010-inch nickel strip sensor revealed the presence of a “ringing” quality that often indicates a poor bond. After cycling, much of the signal strength remained, but the ringing became worse and spurious indications invaded the signal.

The sensor strips were carefully peeled away from the aluminum to investigate bond quality. It was noticed immediately that the epoxy bond to the 0.005-inch strips was fairly weak compared to the bond to the substrate aluminum, which had a somewhat roughened surface. However, in the case of the 0.010-inch strip, the epoxy had a very poor bond to the aluminum (in this case, a very smooth surface), which would explain the poor signal at baseline. Based on these observations, extra steps were taken to prepare the aluminum and nickel surfaces for epoxy bonding before application of the sensors. Initially, 320-grit sandpaper was used in a circular motion to abrade the aluminum enough to remove its milled finish in the region to be bonded. To avoid the complications of a bond failure due to flaking of aluminum oxide to the base aluminum after the epoxy was applied, a technique was used to remove the oxide layer before bonding. Epoxy resin was dissolved in acetone, and the solution was poured liberally on the aluminum, which was scrubbed with a Scotch-Brite® pad to abrade the oxide and leave a thin film of resin on the base aluminum surface to avoid further oxidation. The surface was allowed to dry, and isopropanol was used to cleanse the area. The nickel strip was also abraded with 320-grit paper to remove its mill finish and cleaned with isopropanol. This procedure was first performed on a 0.005-inch-thick continuous strip then on a 0.010-inch strip.

The prepared sensors were retested using the simulated thermal cycle. Performance of the 0.005-inch strip after simulated thermal cycling showed no improvement over the previously collected data. This strongly suggests that the problem is not a result of an epoxy or bond failure. This evidence is bolstered by the fact that removal of the strip was more difficult than in the initial case of minimal surface preparation. The baseline data taken on the 0.010-inch strip assured that a strong bond was accomplished with the surface preparation technique, and in the retest, there was no ringing in the signal and no effect on the guided wave data.

2.1.2.5 Modeling Results -Effect of Stress on Nickel Films and Strips — Literature Survey

Nickel has a negative magnetostriction in the bulk. This negative magnetostriction means that a nickel bar will shorten slightly under the application of a magnetic field parallel to the axis of the bar. The sign of the magnetostriction affects the action of stress on magnetic properties [2]. In nickel, this means that tension will cause an increase in the coercivity and a decrease in remanence and maximum differential permeability, and further that compression will cause a decrease in coercivity and increase in remanence and maximum differential permeability, both effects of which are just opposite to the effect of tension and compression in steels [3]. On the other hand, in films of sufficiently small thickness, these stress effects behave oppositely again to the way they behave in bulk [4, 5]. The question thus arises as to how magnetic properties in nickel strips will behave in response to stress.

The issues to consider are twofold: (1) There are no systematic studies as to how nickel strips behave with respect to stress, and thus we must either do a study ourselves, or try to predict what will happen based on work with films or based on inferences from what little work does exist on strips; (2) Although there are studies in bulk nickel on magnetic behavior in the presence of constant stress, there is little or no work done in nickel on the effect of varying stress on magnetic properties in the presence of constant field [7], which is an effect known as the magnetomechanical effect [8]. Both issues need investigation if we are to understand the effect of using nickel strips instead of electromagnets in the magnetostrictive generation of elastic waves in pipes and plates.

It is known that bulk nickel has face-centered cubic (fcc) crystal structure and has a lattice constant $a = 0.352$ nm, a Curie temperature of 630 K, and a saturation magnetic moment $\mu_s = 0.6 \mu_B$, where μ_B is the Bohr magneton. The Curie temperature and the saturation magnetic moment are smaller than in either iron or cobalt. Like nickel, cobalt also has a negative magnetostriction [9]. Iron exhibits positive magnetostriction until the field gets sufficiently high, and then the magnetostriction starts decreasing, eventually going negative [10]. The magnitude of nickel's magnetostriction, ignoring sign, is considerably larger than in iron, which is a reason for using it in combination with magnetostrictive wave generation.

Nickel films on the other hand display somewhat different properties. As mentioned earlier [5], nickel films in the range 15 nm- 200nm display a magnetic effect of applied stress that is opposite to that in the bulk. This may be related to magnetic anisotropy effects observed in nickel films. For example, one research group [11] finds that in the range of 7-10 ML (monolayers) to 35-70 ML, the film has a perpendicular magnetic anisotropy, which means that the easy axis of magnetization is perpendicular to the film. Since in fcc nickel, a monolayer will be half the lattice constant in thickness, one finds that 70 ML corresponds to 12.3 nm, and we see that the films with stress properties opposite to those in bulk have in-plane magnetic anisotropy. It has been shown however that the perpendicular anisotropy is produced by perpendicular magnetoelastic anisotropy [12]. Normally, if stress is in-plane and if the stress axis is parallel to the field axis and if the magnetostrictive sign is negative, then the coercive field H_c increases with increased stress. However if the stress anisotropy (i.e. magnetoelastic anisotropy) is out-of-plane (even if the net magnetic anisotropy is in plane), then the coercive field will decrease with increased stress, which is opposite to behavior in bulk.

Callegaro and Puppini [5] found that a film of 10 μm thick (0.0004 inches thick) approached bulk behavior of nickel. SwRI used a Ni strip that is of the order of 0.005 inches (or 12 times the thickness of the bulk-behaving Ni film which is 10 μm thick), so it would seem that the strip should have bulk behavior. This behavior is for constant stress in a time varying field.

Nevertheless, seemingly aberrant behavior occurs in this nickel strip in the case of varying stress and constant field, which is the stress-affected magnetic behavior that is little studied in nickel, and which needs to be studied further if the stress effects in nickel are to be better understood. It is already known that in steels, this type of magnetization behavior with varying stress can exhibit unusual excursions, [7] so the case must be treated in detail in order to gain understanding of the behavior.

A sample of 0.010-inch-thick iron-cobalt alloy was purchased to evaluate its magnetostrictive properties and also to evaluate its behavior under compressive and tensile stress. The magnetostrictive coefficient of the alloy compared to the nickel alloy is shown

in Figure 22. A $\frac{3}{4}$ inch by 8 inch piece was cut from the sample and bonded onto an $\frac{1}{8}$ inch thick aluminum plate. An initial reference waveform was collected. Then the plate was subjected to a compressive stress and another waveform obtained. Then a tensile stress was applied to the plate and another waveform obtained. These waveforms are shown in Figure 23.

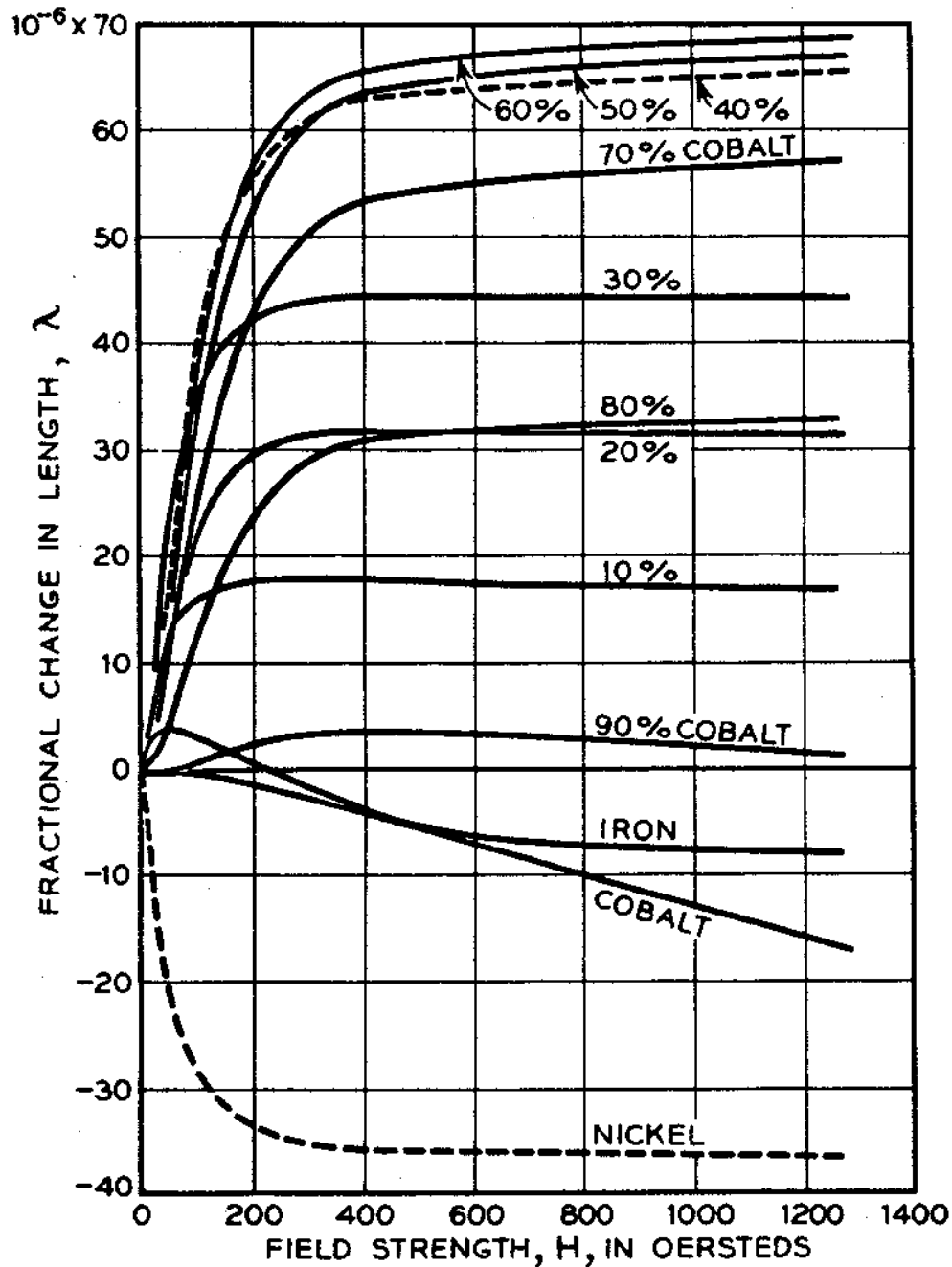


Figure 22. Plot of fractional change in length as a function of applied magnetic field strength (see Reference [1])

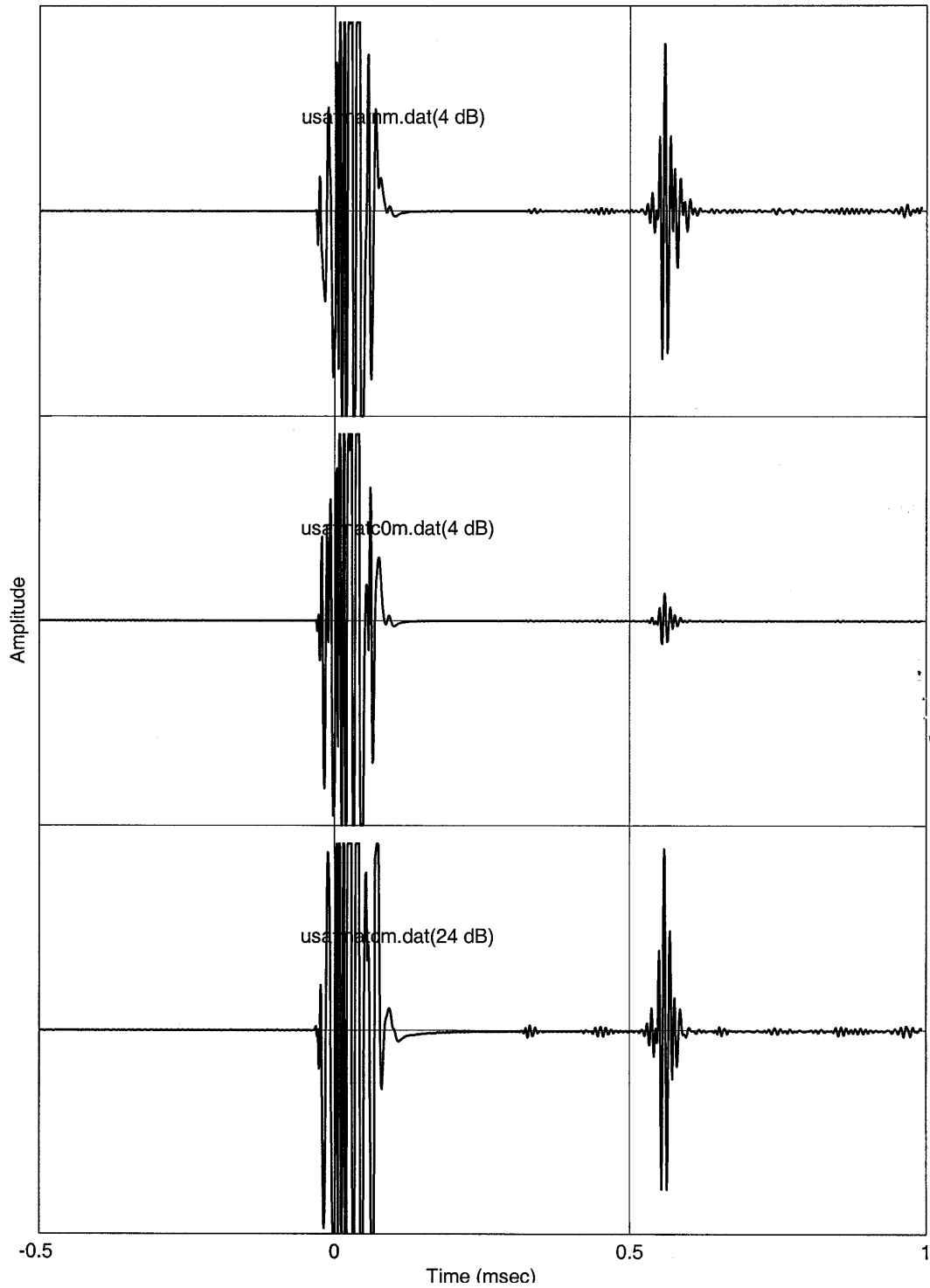


Figure 23. Waveforms obtained from the nickel (top waveform), the iron-cobalt (50/50) alloy (middle waveform), and the iron-cobalt (50/50) with 20 dB more gain. All magnetostrictive material was bonded to a 1/8-inch-thick aluminum plate.

2.1.3 *Investigation of Corrosion Issues with Bonded Nickel Strips on Steel and Aluminum*

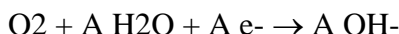
If a nickel strip bonded to a structure is used to monitor that structure, it is important that the nickel not serve as a potential corrosion source. The following discussion addresses direct contact between nickel and steel or aluminum structure materials and is the worst case. It is expected that the epoxy layer or adhesive layer between the nickel and steel or aluminum will mitigate the corrosion potential.

The primary cause of potential corrosion is moisture egress through the edge of the bond interface. Careful application of the nickel to the steel or aluminum should minimize this moisture egress. However, in the event of moisture egress into the bond interface, the following discussion provides insight into the potential problems that need to be considered.

The possibility for electrolytic corrosion exists in any system of dissimilar metals. Every metal has an electrical driving potential for oxidation following the simple reaction:



This means that in an electrolyte, such as water, a metal, M, will oxidize into a positive ion based on its valence number, A, and the corresponding number of electrons. If submersed in an electrolyte, the metal ions will be removed, or corroded, from the metal surface and enter the electrolyte. The electrons will travel through the metal to another region on the surface of the metal and reduce the water to yield hydroxyl ions following the reaction:

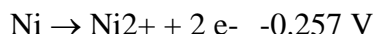
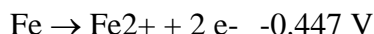


where A is the valence number of the metal.

2.1.3.1 *Nickel on Steel*

In steel, the free Fe^{2+} ions react with the free OH^{-} ions in the water and create $Fe_2O_3 \cdot H_2O$, red rust. The reaction will cease in a given location as long as the rust shields the underlying iron; however, rust tends to flake and crumble thus allowing further corrosion.

When two metals are in close proximity in an electrolyte, electrolytic potential voltages of the oxidation reactions determine which of the metals will corrode and which will be protected. With nickel and iron, the oxidation reactions have the following potentials:

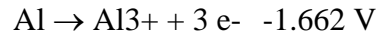
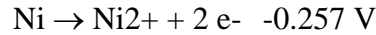


In electrolytic cells, the reaction with the more negative voltage potential is forced into the role of the corroded metal, while the higher voltage is the protected metal. Therefore, in a system with nickel and iron (the chief component in carbon steel) the iron will oxidize or corrode, and the freed electrons serve to ensure that the nickel is prevented from oxidizing. This reaction has a total electrolytic potential of 0.190 V, making it a very weak galvanic cell.

The extent of corrosion over time depends on the amount of water and oxygen available to the interface between the two metals. In very humid climates, electrolytic potentials greater than 0.15 V are not acceptable. However, in highly moisture-controlled environments (i.e. indoor climate control), potentials up to 0.50 V are allowable because electrolyte, water, is not likely to encounter the metal interface and remain there.

2.1.3.2 *Nickel on Aluminum*

The oxidation reactions and electrolytic potentials for aluminum and nickel are:



This indicates that aluminum has a far more negative potential than nickel and would corrode more quickly than would steel in the presence of water. The total electrolytic potential of this system is 1.405 V, making it a fairly strong galvanic cell. However, aluminum quickly deposits a protective layer of aluminum oxide and is highly resistant to corrosion, typically, and this would minimize the potential for galvanic reaction. If the nickel strip is bonded to aluminum that already has the protective aluminum oxide layer or is painted, the potential for corrosion should be very low.

2.1.3.3 *Experiments to Determine Whether the Nickel Strip Can Be Activated by a Coil Placed on the Other Side of the Aluminum Panel*

To answer this question, the following tests were conducted using a 0.010-inch-thick nickel strip on the edge of a 1/8-inch-thick aluminum plate. A coil with a ferrite core and coils forms a plane normal to the plate (not parallel as with the thin film coil we had once used) was used to generate the shear horizontally (SH) polarized guided wave in the nickel strip. The inspection frequency was 128KHz. The purpose of this question was the scenario where the nickel strip would be placed on the inside surface of a wing skin (to keep it out of the air flow and to minimize potential debonding issues) and to activate the MsS nickel probe using a coil on the outside surface of the wing skin.

First, a reference waveform was obtained with the nickel and coil on the same side of the aluminum plate with zero lift off between the nickel and the coil (shown in top waveform in Figure 24). The baseline gain was set at 6dB and the pulser power was set at 20%. Then a 0.06 inch thick aluminum plate was placed between the nickel and the coil and the waveform shown in middle of Figure 24 was obtained. The gain was raised to 26dB and the pulser power was set at 20%. Then the coil was placed on the opposite side of the nickel on the aluminum plate surface so that there was approximately .125 inch of aluminum between the coil and the nickel (lower waveform in Figure 24). The gain was raised to 40dB and the pulser power raised to 60%. The results showed that there was a 20dB loss of signal strength with the 0.06 inch of aluminum between the nickel and the coil (which was easily compensated by the instrument). In addition, the basic signal characteristics remained the same in both cases. When 1/8 inch aluminum was placed between the nickel and the coil, a large amount of signal loss was observed. However, when an Al-5 magnet was placed across the nickel strip during the data collection, the original signal strength was still almost achieved with the gain set to 40dB and the pulser power set to 60%. This signal is shown as the middle waveform in Figure 25. The

lower waveform in Figure 25 was obtained by increasing the pulser power to 80%. A more practical scenario would have been to place the magnet around the coil (not the nickel) and determine whether this process would improve the capability to look through the wing skin.

Additional experiments using a ¼ inch aluminum standoff were conducted and it was found that high frequency data (ie, 128KHz) could not be obtained through the ¼ aluminum standoff even with 50dB instrument gain and pulser power of 100%. However, some data could be obtained by lowering the frequency to 64KHz and by using 50dB gain and 80% pulser power.

Additional data were collected with the magnet located over the sensor side of the aluminum (which is a more realistic scenario). The results are shown in Figure 26. The top waveform is the baseline with the sensor on top of the nickel strip. The second waveform is with 1/8-inch aluminum between the nickel and sensor with a magnet over the nickel strip. The third waveform is with the magnet over the coil but located over one edge of the nickel. The fourth waveform is with the magnet centered over the coil and center over the location of the nickel. The fifth waveform is taken under the same conditions as the third waveform, but the instrument gain has been increased from 36 dB to 60dB.

These results were encouraging. However, in practice, if the nickel strip is placed on the inside surface of the wing skin, some method for locating the nickel strip from the top surface of the wing skin will be required. One approach would be use a magnetic flux meter to locate it and then mark the location on the top wing skin during installation.

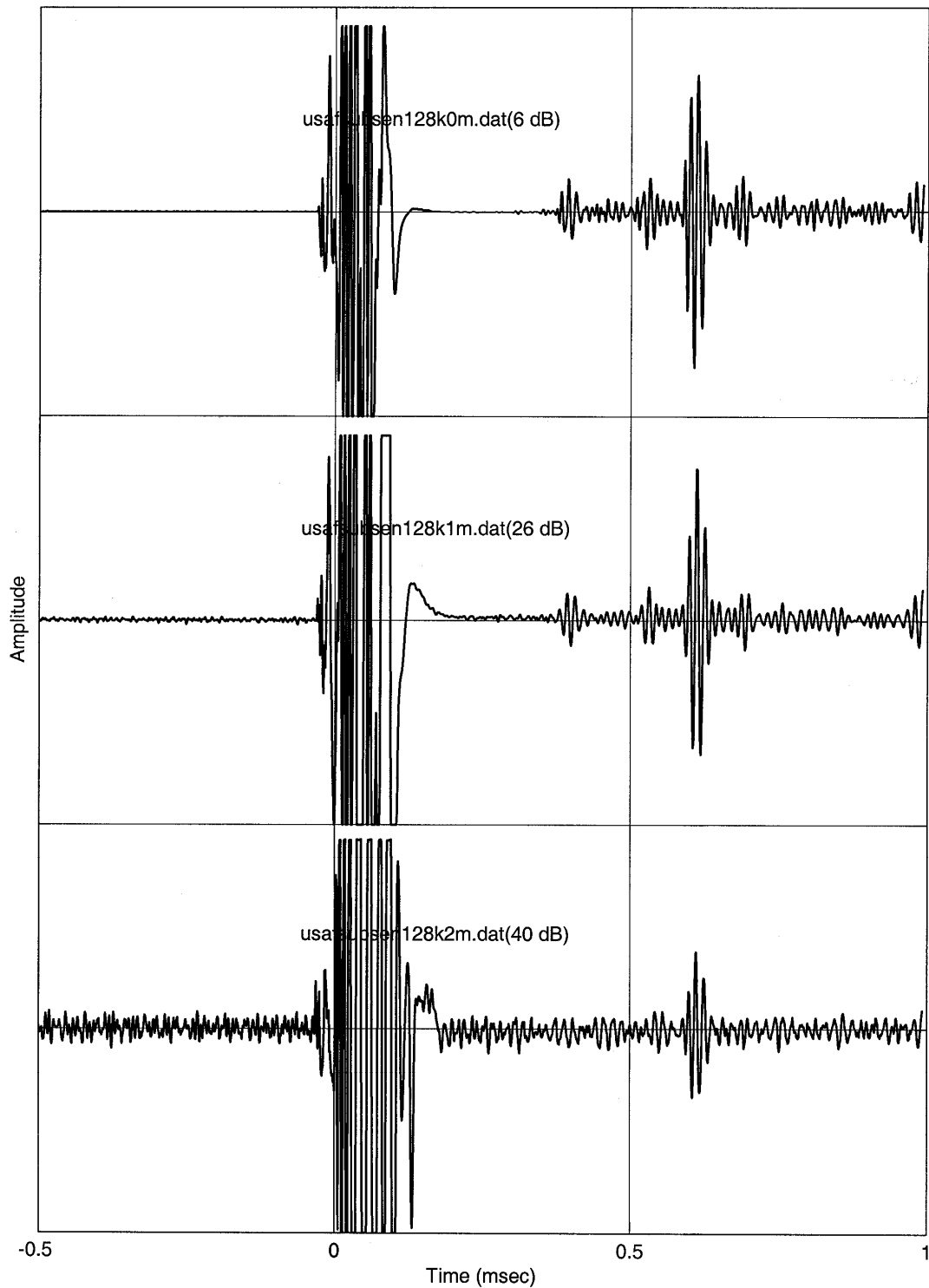


Figure 24. The top waveform is the reference waveform obtained with the nickel and coil on the same side of the aluminum plate with zero liftoff between the nickel and the coil; the middle waveform obtained with a 0.06-inch-thick aluminum plate placed between the nickel and the coil; and the lower waveform obtained with the coil placed on the opposite side of the nickel on the aluminum plate surface so that there was approximately 0.125 inch of aluminum between the coil and the nickel.

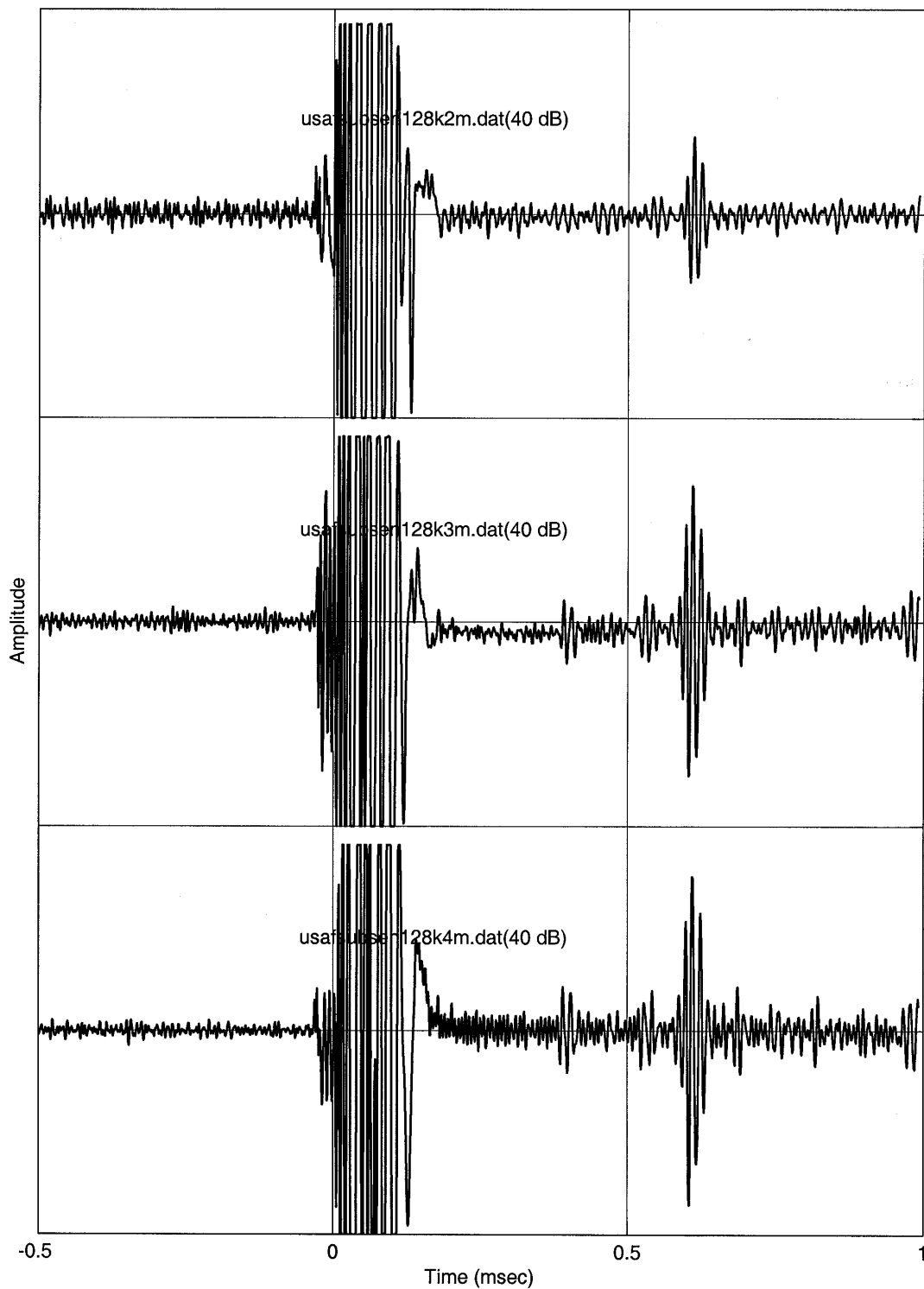


Figure 25. Top waveform obtained with the coil placed on the opposite side of the nickel on the aluminum plate surface so that there was approximately 0.125 inch of aluminum between the coil and the nickel; middle waveform obtained when an A1-5 magnet was placed across the nickel foil during data collection; and the lower waveform obtained under the same conditions as the middle waveform, except the pulser power was increased from 60 to 80 percent.

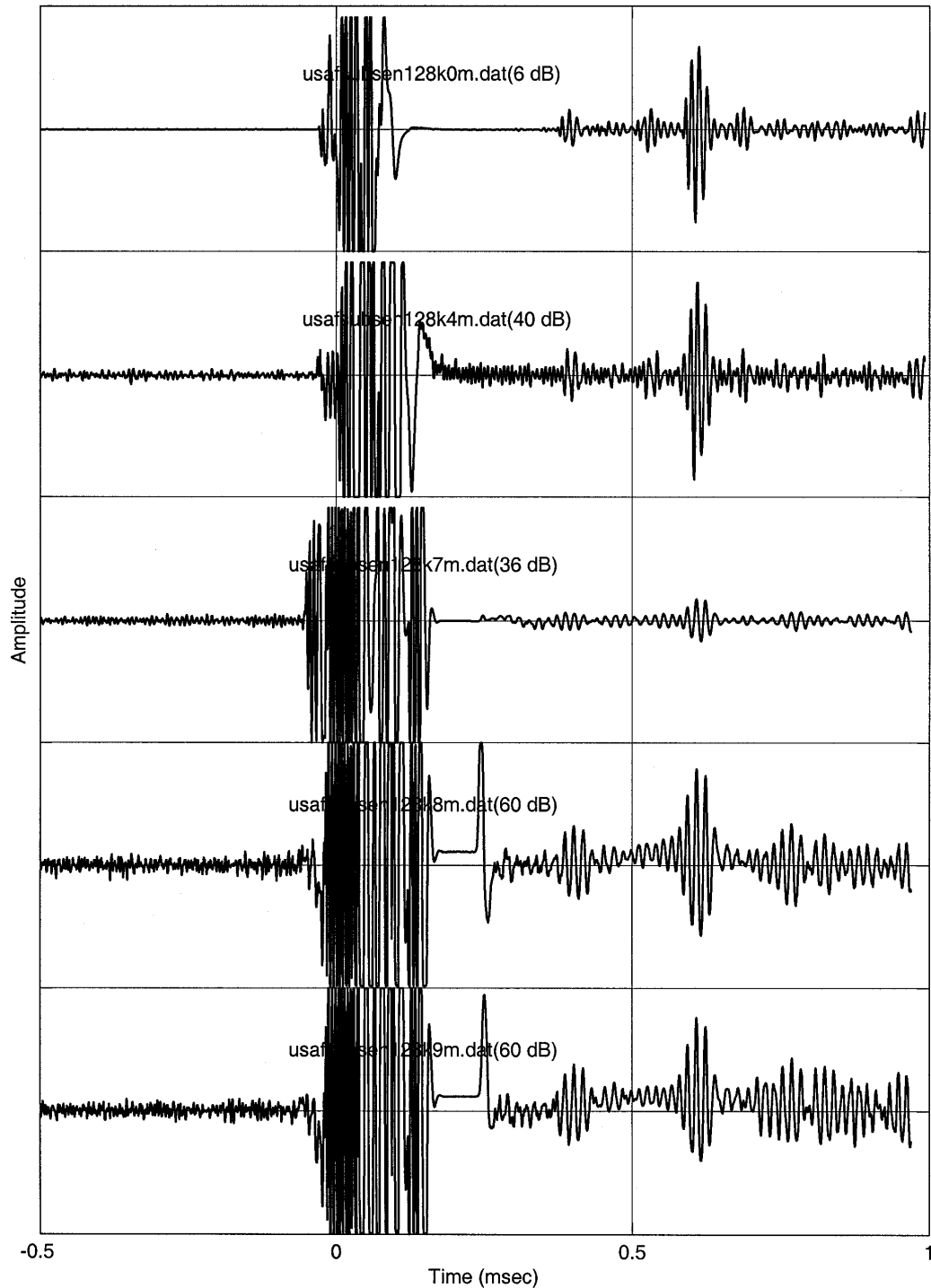


Figure 26. The top waveform is the baseline with the sensor on top of the nickel foil. The second waveform is with 1/8 inch of aluminum between the nickel and sensor with a magnet over the nickel foil. The third waveform is with the magnet over the coil but located over one edge of the nickel. The fourth waveform is with the magnet centered over the coil and over the location of the nickel. The fifth waveform is the same as the third waveform but with 60 dB gain versus 36 dB gain.

2.1.3.4 Effects of Simulated Altitude on Bonding of Nickel to Aluminum

The same plate used to evaluate thermal and stress effects on nickel bonded to aluminum using the 3M™467 adhesive was used to do an initial investigation on the potential effects of low pressure (high altitude) on the magnetostrictive properties of the nickel sensor. Testing consisted of placing the test sample into a pressure/temperature chamber. The starting pressure and temperature were atmospheric and approximately 150°F, respectively. The chamber was then brought down in pressure and temperature to a pressure equivalent to 40,000 feet and a temperature of –65°F and then returned to atmospheric and 70°F in a one hour cycle. Then this process was repeated for 65 cycles. The data obtained are shown in Figure 27 and it is clear that the temperature and pressure did not significantly affect the magnetostrictive properties of the nickel strip bonded to aluminum.

2.2 Data Acquisition and Analysis

SwRI developed a software package that allows MsS data waveforms to be used for monitoring changes in the waveforms. The software performs a comparison of the reference waveform with subsequent waveforms with a comparison and subtraction (monitoring) routine. This is illustrated in Figure 28 and Figure 29. In addition, as can be seen in these figures, the subtracted signals are provided in both the rf and video versions so that the difference can be viewed. The important features of this software are that when two signals are subtracted that should have no change in the physical conditions of the pipe or plate, that the subtracted signal be basically a flat line except where the initial pulse is (due to saturation of the pulse and inability for the digital version of the pulse to be repeatable). If there is constant reflector in the field of the MsS that appears in the waveform (such as a plate edge, that reflector can be used to compensate for any velocity changes due to change in temperature on the part and amplitude changes that might be caused by variations in the instrument.

2.3 Modeling

To effectively use the MsS technology, it is important to be able to model the interaction of the guided wave generated by the MsS and how it interacts with reflectors. It is hoped that this will provide insight into the ultimate goal of being able to look at a reflected signal in the data and, knowing the basic parameters of the wave propagation, be able to characterize the reflected signal as to its defect type and size.

The wave behavior in pipes and flat plate are similar, yet have some major differences. The purpose of this section is to provide a concept to model the MsS generated guided wave and how it interacts with reflectors for the pipe wall (basically a one dimensional problem) and for flat plate (a two dimensional problem). The basic modeling tool is the transmission line model.

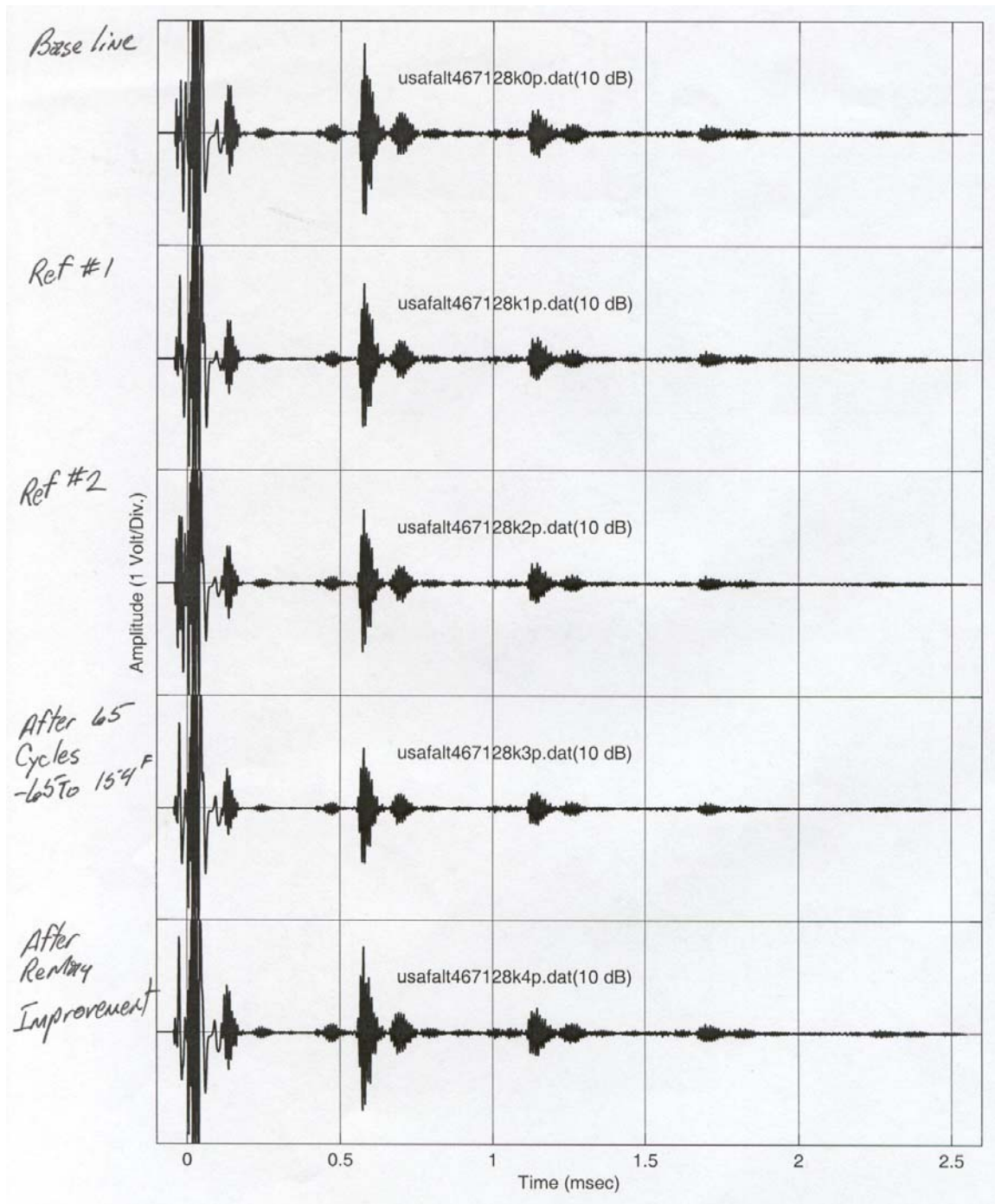


Figure 27. MsS data collected from a nickel strip bonded to an aluminum plate using the 3M™467 adhesive. The plate was subjected to a simulated altitude and thermal cycling. The plate started at 70°F and atmospheric pressure, dropped to -65°F and 40,000 feet pressure, and then returned to atmospheric pressure at 70°F and then heated to 150°F. As can be observed in the data, there is no significant change in the magnetostrictive sensor signals.

Compensation Method: No Reference
Reference Signal Location: --
Velocity Difference: -- %
Amplitude Difference: -- %
Origin: -1.00 ft
Velocity: 127.95 ft

Frequency: 128 kHz
Filter: 128 kHz
Total Gain: 10 dB
Pulse Rate: 16
Cycles: 1
Amp: 20 percent

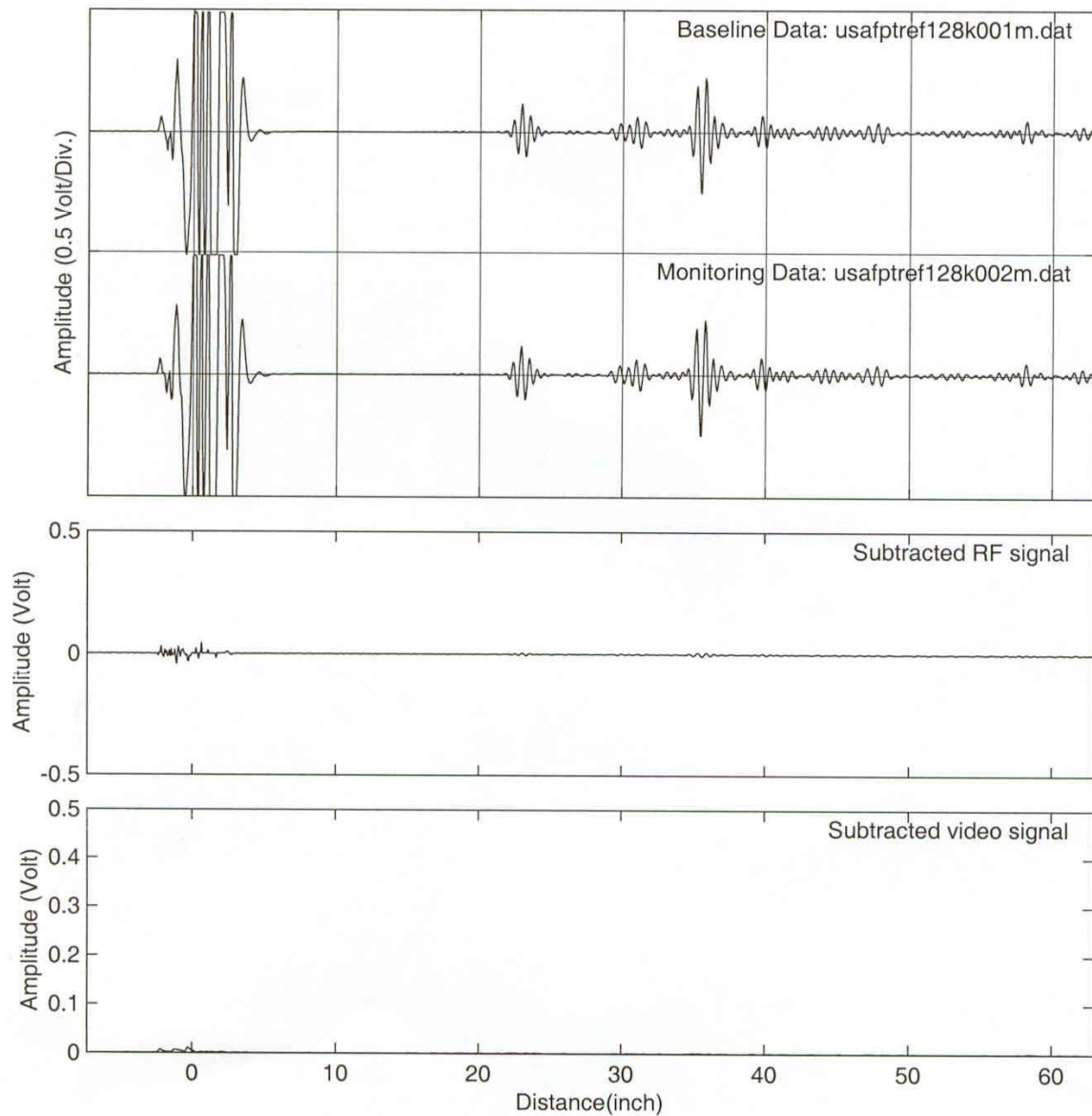


Figure 28. Reference data compared to another data set collected before disbonding

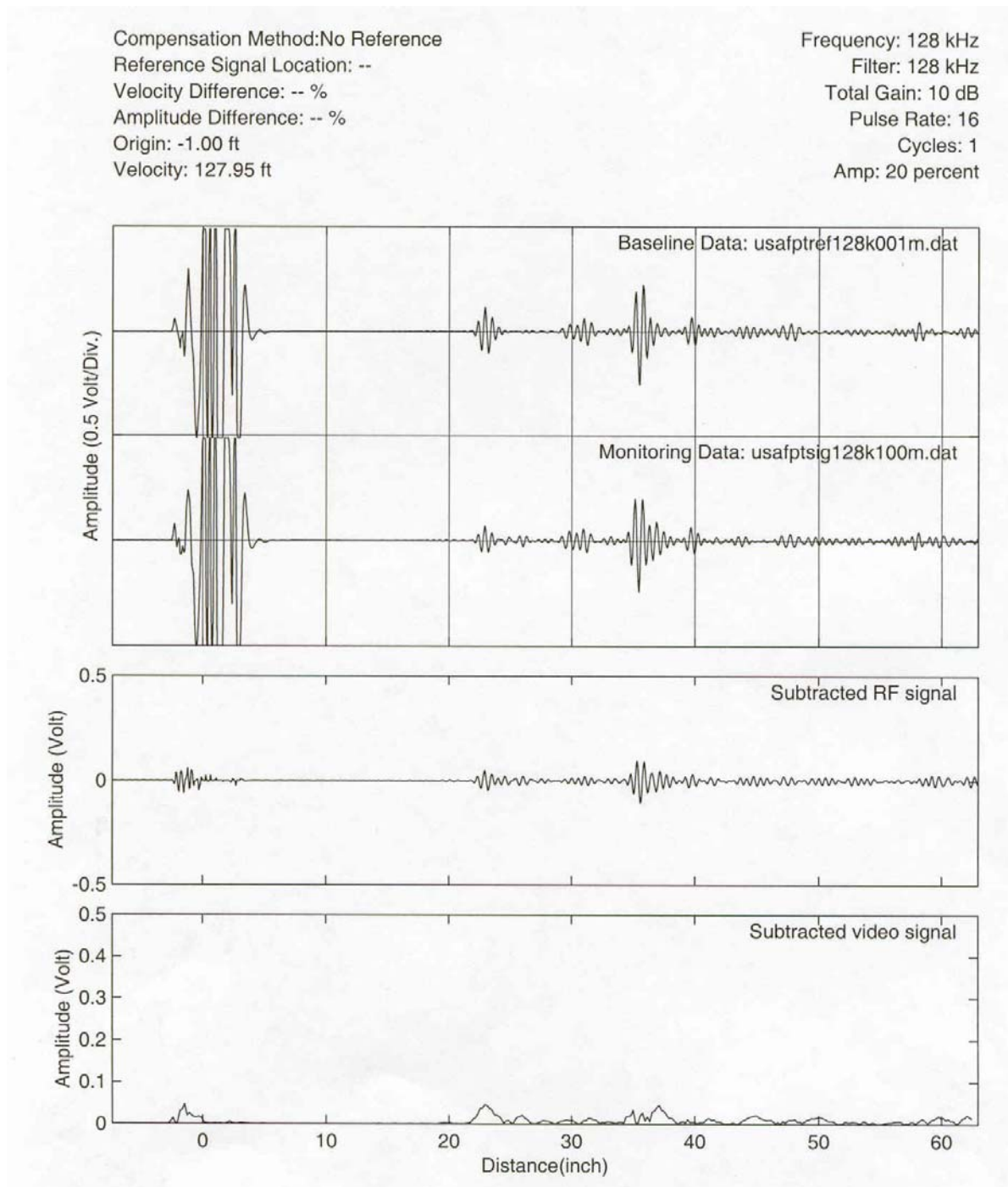


Figure 29. Inspection waveform (called monitoring data) showing a slight change at a distance of approximately 23 inches from the end of the plate

Phenomenologically, the interaction of guided waves with defects in pipe might be treated as the one-dimensional problem of plane wave reflection and transmission at boundaries of different mechanical impedances [7]. The reflection coefficient, R , from a planar defect in pipe could then be conveniently expressed as:

$$R = \frac{Z_d - Z_p}{Z_d + Z_p} = \frac{A_d - A_p}{A_d + A_p} \quad \text{Eq. 1}$$

where $ZX = \rho VAX$, ρ is the density of pipe material, V is the velocity of guided waves in pipe, AX is the cross-sectional area of the pipewall at location X , d denotes defect location, and P denotes the pipe with no defect. The above simple expression is found to be useful for relating the defect signal amplitude and the cross-sectional area of a planar defect [7].

The above phenomenological description of guided-wave interaction with defects is now expanded to treat arbitrary volumetric defects by using the transmission line model [8]. With the transmission line (TL) model, a volumetric defect is treated as a transmission line consisting of a total of N layers of different mechanical impedances, as illustrated in Figure 30. The reflection coefficient, $R(\omega)$, from the defect at angular wave frequency ω can then be expressed as:

$$R(\omega) = \frac{Z_d^{eff} - Z_p}{Z_d^{eff} + Z_p} \quad \text{Eq. 2}$$

where Z_d^{eff} is the effective impedance of the defect and is equal to the input impedance of the overall layer, Z_{N+1}^I . According to the TL model, Z_{N+1}^I is obtained using the recursion relation for the input impedance of the two successive layers:

$$Z_{n+1}^I = Z_n \frac{Z_n^I + j Z_n \tan(k \zeta_n)}{Z_n + j Z_n^I \tan(k \zeta_n)} \quad \text{Eq. 3}$$

where Z_n^I is the complex input impedance of layers of up to n , where $n = 1, 2, \dots, N$, and Z_n is the mechanical impedance of the n th layer, k is the wave number, ζ_n is the thickness of the n th layer, and $Z_1^I = Z_p$.

The time-domain waveform of a defect signal, $A_d(t)$, produced by a pulse of incident wave of waveform, $A_0(t)$, is given as:

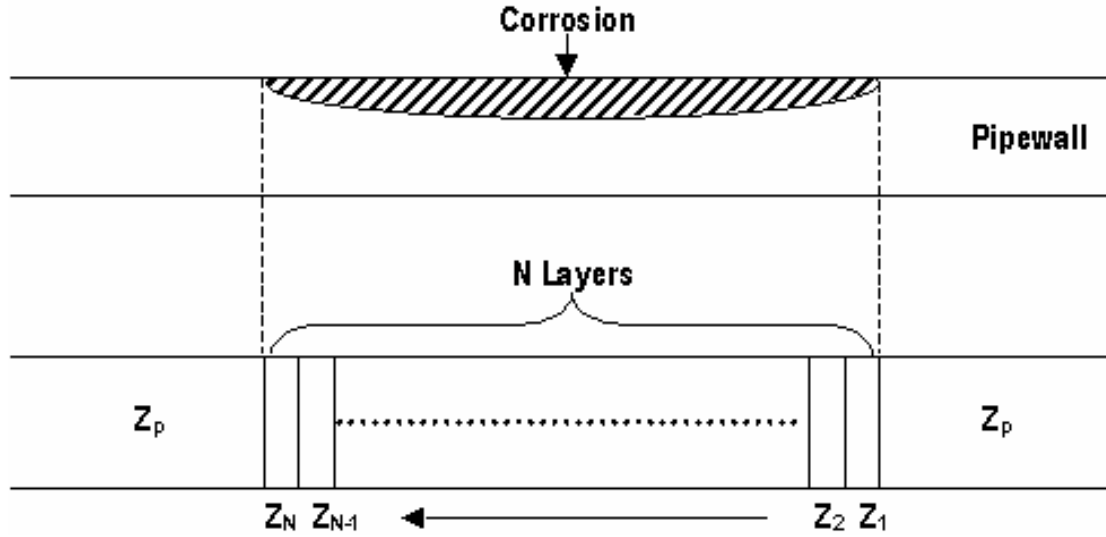


Figure 30. Defect cross section and its transmission line model representation

$$A_d(t) = \frac{1}{2\pi} \int R(\omega) A_0(\omega) e^{j\omega t} d\omega \quad \text{Eq. 4}$$

where $A_0(\omega)$ is the ω component of the Fourier transformation of the incident pulse.

2.3.1 Modeling For Propagation in Pipe

Utilizing the TL model, signal waveforms of volumetric defects of different shapes were simulated. Examples of such waveforms are shown in Figure 31. In this case, the pipe was 4.5 inches in outside diameter and had a 0.336-inch-thick wall, and two types of defects as illustrated in Figure 32 were considered, a stepwise change in the pipewall and a circular corrosion pit. All defects had the same maximum depth, $D = 0.3$ inch; the same maximum width in the circumferential direction, $W = 3.23$ inches; and thus the same maximum cross-sectional area that was approximately 11 percent of the total pipewall cross-sectional area. Calculations of the simulated waveforms were then performed for 64-kHz longitudinal wave and 32-, 64-, and 128-kHz torsional wave modes.

In all four sets of simulated waveform plots in Figure 30, the first waveform is for the stepwise change in the pipewall. The second through fifth waveforms are for the circular corrosion pits whose axial lengths (L) were 0.5, 1, 2, and 4 inches, respectively. The waveform of the incident pulse was the same as the waveform for the stepwise change except that the amplitude was larger. The value of the apparent reflection coefficient, r , of each defect, which was calculated by dividing the maximum amplitude of the simulated defect signal with that of the incident pulse, is also given in the figures.

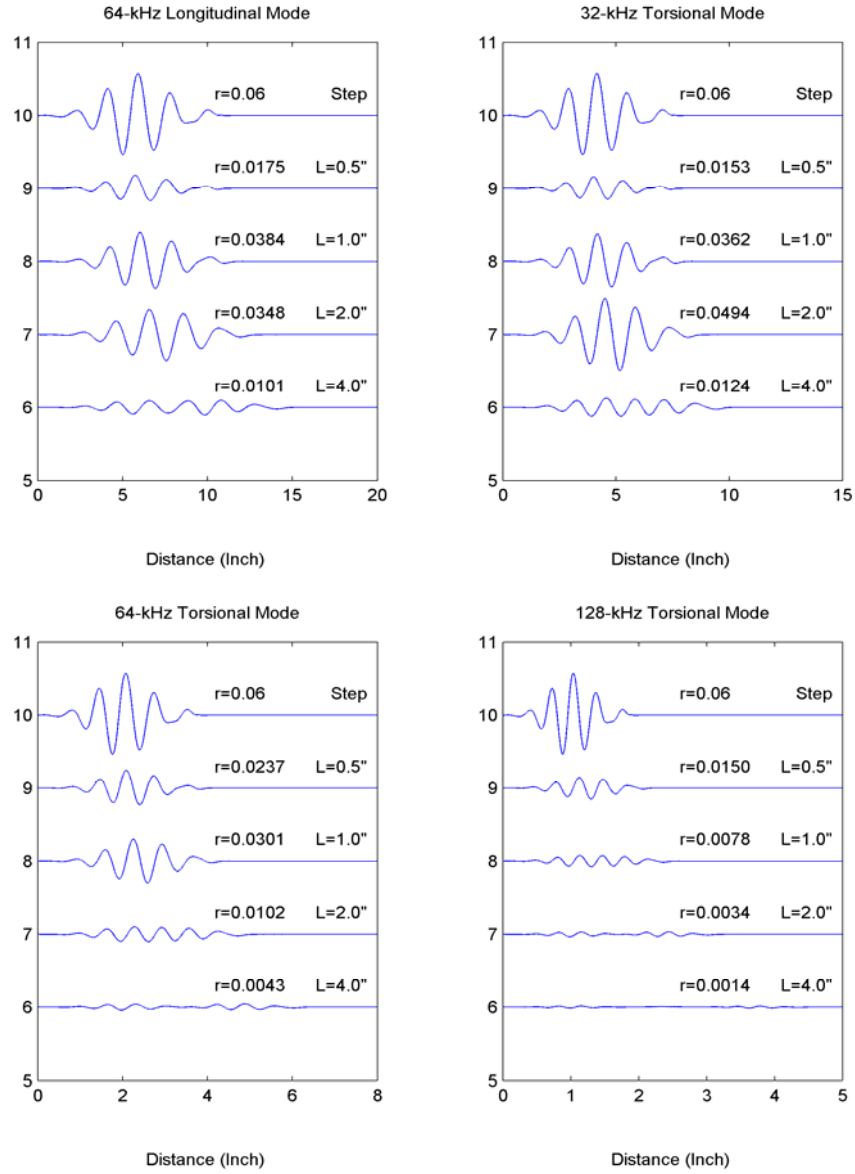


Figure 31. Examples of simulated defect signal waveforms

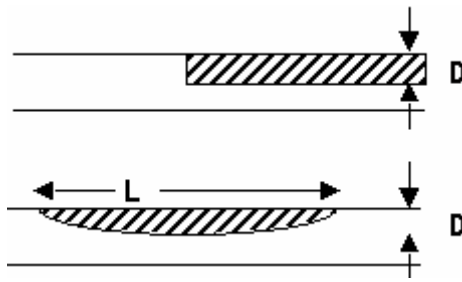


Figure 32. Cross section of defects in the axial direction (top—stepwise change in pipewall; bottom—circular corrosion pit)

From the plots, it can be observed that the waveform from a given defect and the apparent reflection coefficient vary, depending on wave frequency and wave mode, and that this dependence varies with defect shape and size. There is a high potential for achieving defect characterization based on this interdependence between the defect waveform and the defect shape and size.

Qualitatively, the behavior of the waveform change with wave frequency and axial length of the corrosion pit agree very well with what has been experimentally observed. More rigorous and detailed experimental validation of the TL model and refinement of the model should be pursued so that the capability for accurately simulating signals from defects of arbitrary shape and size could be developed. Using the simulation model, algorithms for charactering defects could be developed to achieve the ultimate goal of developing the defect characterization capability.

A wave propagation theory for plate was developed and is provided in this section. The purpose of this theory is to attempt to understand how the shear horizontally polarized (SH-wave) guided wave interacts with a defect as a function of distance from the source and size of the source.

2.3.2 *Modeling for Plate (Two-dimensional Wave Motions)*

At relatively low frequencies satisfying $\lambda > 2t$, where λ is wavelength and t is plate wall thickness, the guided waves such as fundamental shear horizontal wave (SH0) and symmetric Lamb wave (S0) can be treated as a wave propagation in two dimensions because the amplitude of particle displacement is nearly constant along thickness direction.

The plate is assumed to be a linear, homogeneous, and isotropic elastic medium of wave propagation. In vector notation the displacement equation of motion can be written as

$$\mu \nabla^2 + (\lambda + \mu) \nabla \nabla \cdot \mathbf{u} = \rho \ddot{\mathbf{u}} \quad \text{Eq. 5}$$

The wave motion in plate can be obtained by solving the displacement equation with a point source in a system of cylindrical coordinates (r, θ, z) having symmetry of the axial coordinate z and the angular coordinate θ .

For S0 Lamb wave, the radial motions are governed by

$$u = \frac{\partial \phi}{\partial r} \quad \text{Eq. 6}$$

$$\frac{\partial^2 \phi}{\partial r^2} + \frac{1}{r} \frac{\partial \phi}{\partial r} = \frac{1}{V_L^2} \frac{\partial^2 \phi}{\partial t^2} \quad \text{Eq. 7}$$

where u is displacement along r -direction, ϕ is scalar potential, and V_L is velocity of S0 Lamb wave.

For SH wave, the rotary shear motions are governed by

$$v = -\frac{\partial \psi_z}{\partial r} \quad \text{Eq. 8}$$

$$\frac{\partial^2 \psi_z}{\partial r^2} + \frac{1}{r} \frac{\partial \psi_z}{\partial r} = \frac{1}{V_T^2} \frac{\partial^2 \psi_z}{\partial t^2} \quad \text{Eq. 9}$$

where v is displacement along θ -direction, ψ_z is z -component of vector potential, and V_T is velocity of SH0 wave.

Since the general solutions of (3) and (5) are the same form having different velocity, the only SH0 wave will be considered. The solution for a wave diverging from a point source at $r=0$ is

$$\psi_z = B e^{i\omega t} H_0^{(2)}(k_T r) \quad \text{Eq. 10}$$

where $k_t \left(= \frac{\omega}{V_T} \right)$ is wave vector and $H_0^{(2)}(k_T r)$ is a Hankel function of the second type.

The asymptotic representation of the Hankel function for large value of $k_T r$ given as

$$H_0^{(2)}(k_T r) \sim \left(\frac{2}{\pi k_T r} \right)^{\frac{1}{2}} e^{i(k_T r - \pi/4)} \quad \text{Eq. 11}$$

So, the displacement at any location r from a point source at $r=0$ will be represented by

$$v \sim (r)^{-\frac{1}{2}} e^{-i(k_T r - \omega t)} \quad \text{Eq. 12}$$

2.3.3 Guided Wave Propagation by a Line Source

Now let us consider the specific wave motions that are generated by a line source in a homogeneous, isotropic, linearly elastic plate (see Figure 33). The amplitude of displacement at a defect location by the line source is calculated by the integration of all source elements.

Since there are considerable differences in the sound fields generated by long oscillations or by pulses, the signal for simulation was obtained by using 2-cycle, 64-kHz electric pulse by using MsSR system. Figure 34 shows the RF signal of source and its frequency spectrum. The amplitude signals were plotted with dimensionless quantities of distance and the operating frequency, respectively. The RF signal looks like a 3-cycle signal due to the transfer function from electric signal to mechanical wave in transmitting and receiving MsS probe. The frequency spectrum is very similar to the Gaussian form.

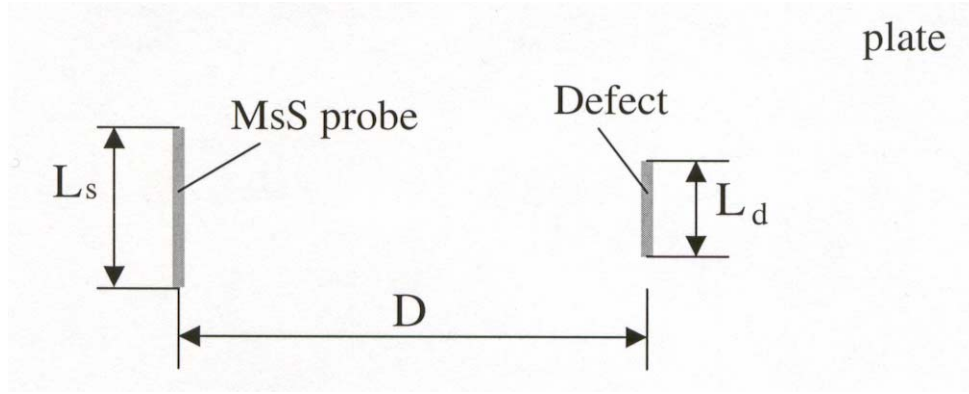


Figure 33. Illustration of relative location of MsS probe and defect for guided wave simulation in plate

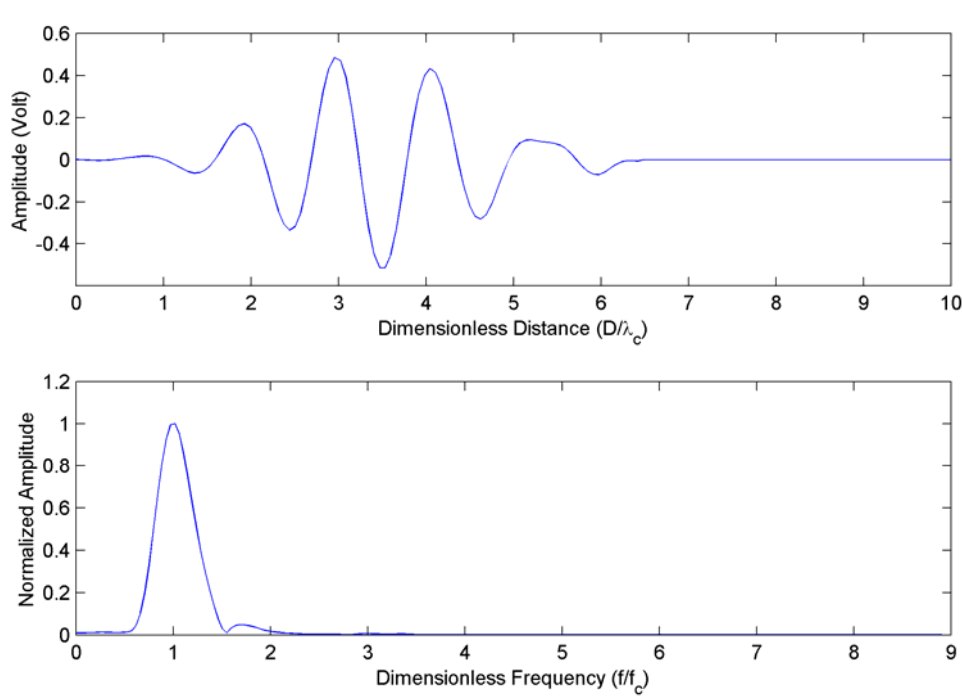


Figure 34. RF source signal (top) generated with MsS system and its frequency spectrum (bottom). f_c : frequency at peak amplitude in frequency spectrum, $\lambda_c = V/f_c$: wavelength at center frequency

Figure 35 shows the amplitude distribution along the distance perpendicular to the MsS probe. The amplitude is normalized with probe size, i.e. the amplitude at more than about 40 times the wavelength will be proportional to the probe size. All the signals show similar pattern: first the increasing stage with an oscillation and second decreasing with exponential function.

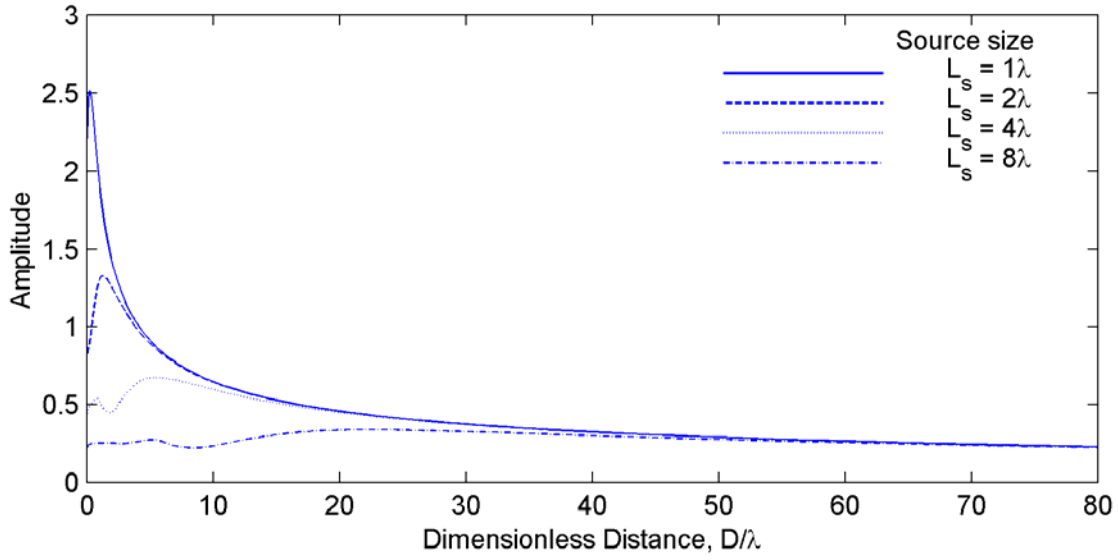


Figure 35. Amplitude distribution along the distance perpendicular to the MsS probe

The distance that the amplitude has a maximum value is called as near field length, N . The near field length is calculated with MsS probe size, L_s , and wavelength, λ .

$$N = \frac{1}{2\sqrt{2}} \lambda \left(\left(\frac{L_s}{\lambda} \right)^2 - 1 \right) \quad \text{Eq. 13}$$

The near field length is proportional to the square of the probe size and to the reciprocal of the wavelength. The amplitude distribution suggests that the quantitative estimate of defect size can be done for the data measured from the defect placed beyond the field distance. This plot shows that the measurement at shorter distance from the MsS probe should be done with small length of probe.

Figure 36 shows the amplitude lateral distribution at 40-times wavelength distance. The beam divergence increases as longer probe size gets bigger. From the lateral distribution it may be calculated that the edge of the beam (the first axial minimum which defines the main lobe) occurs at the angle of divergence α_o given by

$$\alpha_o = \sin^{-1}(\lambda / L_s) \quad \text{Eq. 14}$$

Since the sine function is increasing function of angle, the beam divergence angle is approximately proportional to the wavelength and to the reciprocal of probe size. In ultrasonic testing the use of a narrow ultrasonic beam is desirable for good resolution. But this requirement conflicts with a need for a wide monitoring with minimal probe number installed in the structure under test. So, the probe size and the frequency should be selected on the consideration of the defect size, monitoring area, and resolution.

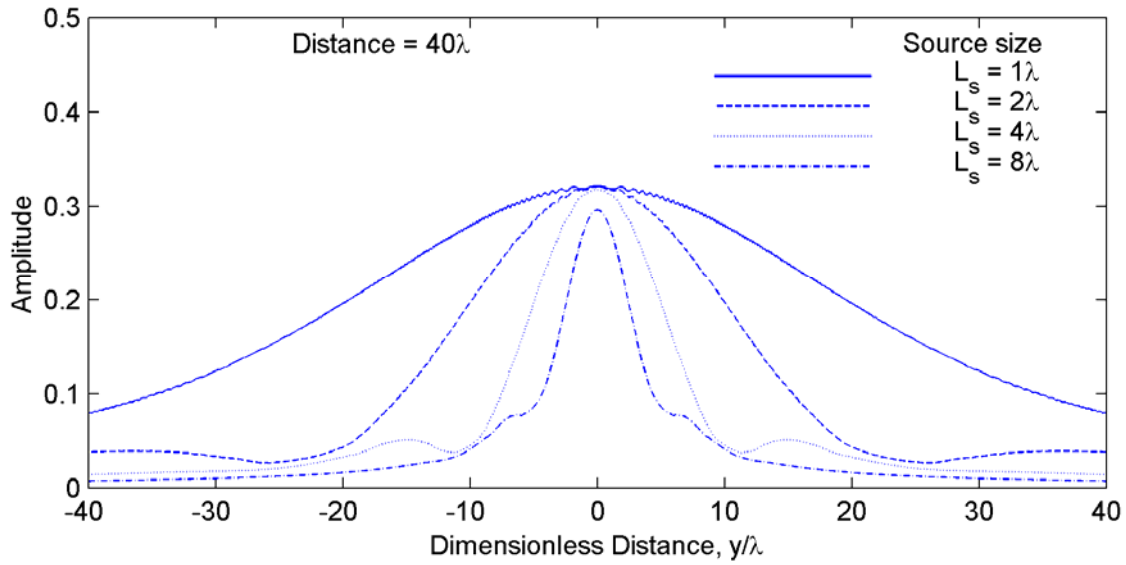


Figure 36. Amplitude lateral distribution at 40-times wavelength distance

2.3.4 Guide Wave Echo Signal Reflected from a Line Defect

Guide wave echo signal was calculated with a defect of one wavelength placed on the axis normal to the MsS probe length in Figure 33. The amplitude distribution pattern is similar to Figure 34 due to the small size of defect. The amplitude distribution along the distance is decided by the probe size that is bigger than the defect.

Figure 37 (a) and (b) show the reflected amplitude variation at distances of 10λ and 40λ from the source as the defect size increases. The reflected amplitudes obtained with the probe size of 4λ and 8λ in Figure 37 (a) are lower than those with the probe size of 1λ and 2λ because the near field length for source of 4λ and 8λ is longer than 10λ . For a defect placed at 40λ , the normalized reflected amplitude with probe size is similar for probe size between 1λ and 8λ . The measured amplitude will be approximately proportional to the probe size.

2.4. Examples of Geometries Evaluated Using MsS

2.4.1 Bonded Thermal Protection for Shuttle

Work was conducted on the space shuttle bonding test sample. MsS nickel strip probes were placed along the length of the sample (approximately 52 inches apart) as shown in Figure 38 and along the width of the sample (approximately 14 inches apart) as shown in Figure 39.

The physical structure of the test panel is unique. The back of the panel is shown in Figure 40 and Figure 41. The profile of the panel is shown in Figure 42. It appears that the panel is a formed piece of aluminum approximately 0.1-inch thick and has a pocket that is filled with honeycomb material. This pocket is attached to the flat aluminum plate either by welding or brazing.

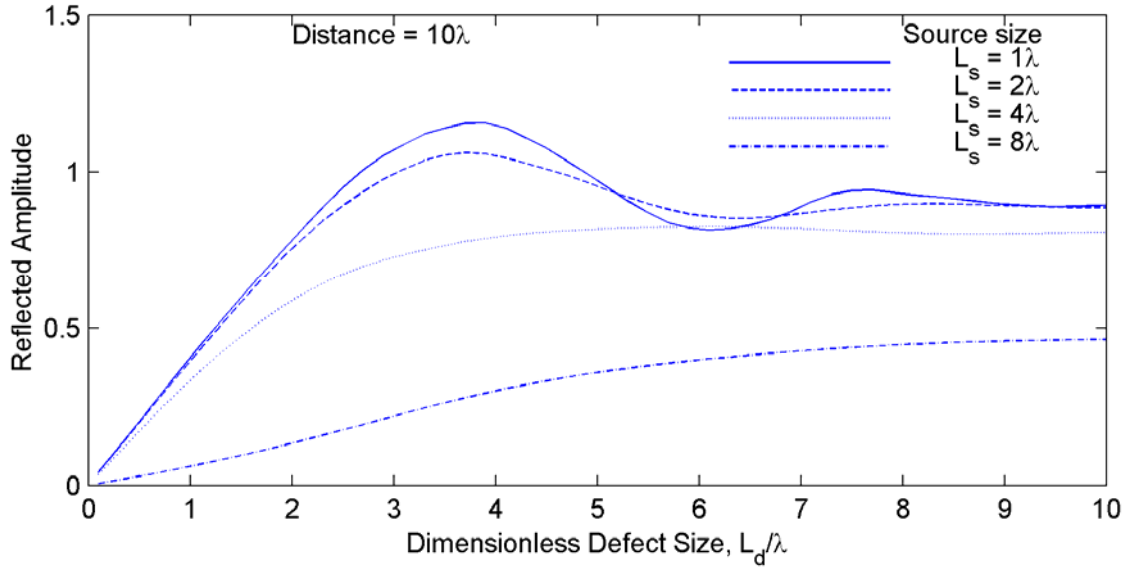


Figure 37(a). Reflected amplitude variation at distance of 10λ

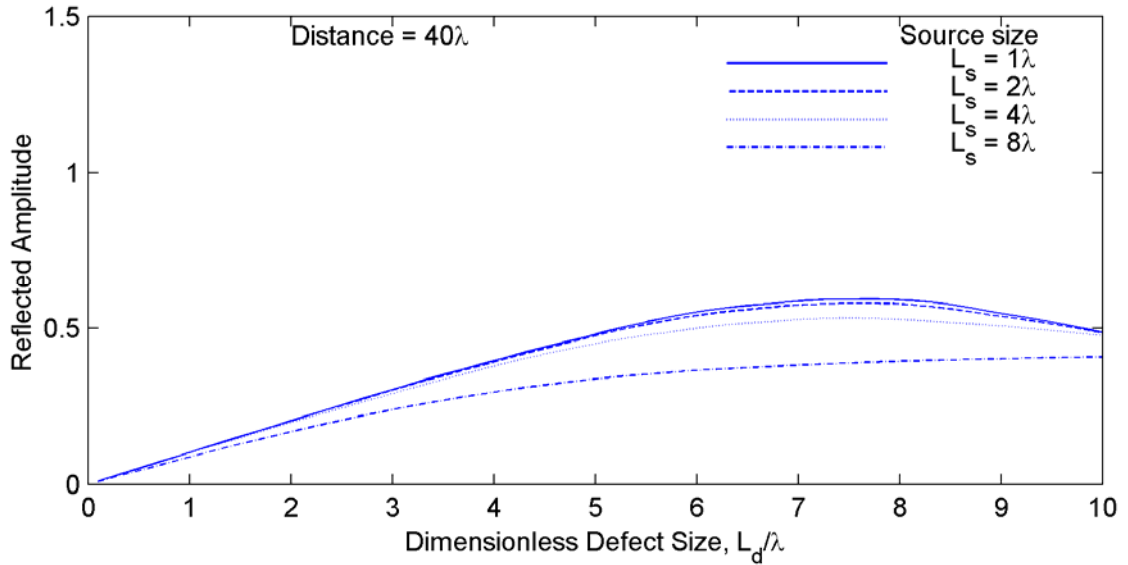


Figure 37(b). Reflected amplitude variation at distance of 40λ

Figure 37. Reflected amplitude variation at distances of 10λ (a) and 40λ (b) from the source as the defect size increases

The data obtained from the MsS nickel strip sensor used in the pulse echo (PE) mode that propagates the guided wave along the length of the panel (as shown in Figure 38) are provided in Figure 43. The time scale in Figure 43 represents approximately 62 inches of metal path. The end-of-the-panel signal should be approximately 0.84 milliseconds from the initial pulse. The waveform in Figure 43 shows signals corresponding to that time frame, but

these signals are not easily detected over the noise level. Presently, these signals are not understood and more work is needed.



Figure 38. Photograph showing the placement of the MsS nickel strip probes for propagating guided waves along the length of the test panel



Figure 39. Photograph showing the placement of the MsS nickel strip probes for propagating guided waves along the width of the test panel



Figure 40. Profile view of part of the test panel showing the pocket filled with honeycomb in relation to the flat aluminum panel



Figure 41. Bottom view of the test panel showing the pocket filled with honeycomb. The bottom face sheet appears to be brazed or welded to the edge of the plate.

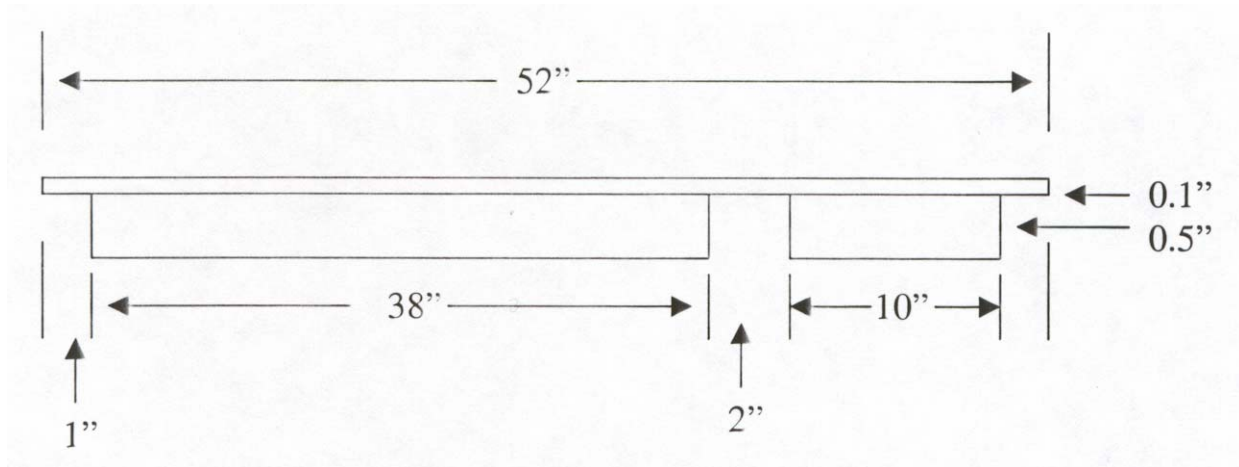


Figure 42. Profile of the test panel

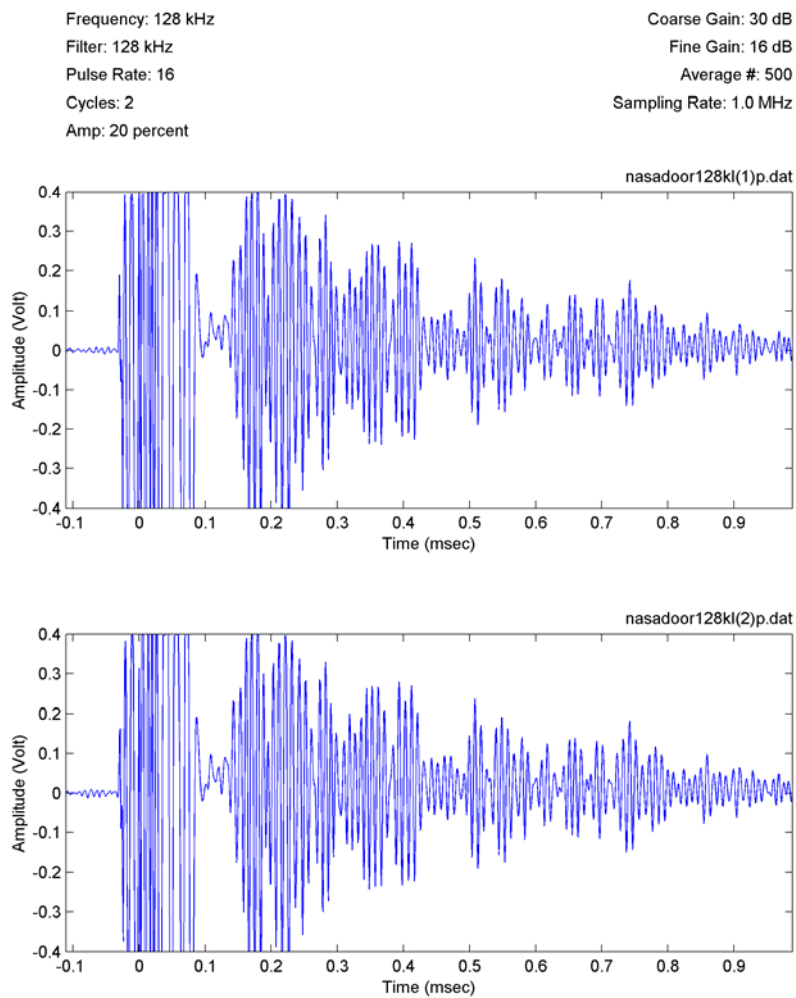


Figure 43. Data obtained from the placement of the MsS nickel strip probes along the length of the test panel in PE mode

A space shuttle panel was investigated using MsS in the pitch-catch (PC) mode. The transmitter and receiver were located on each end of the test panel as shown in Figure 44. The inspection frequency was 64 kHz. Prior to testing, a small region of the TPS was delaminated to determine if PE MsS could detect the debond (see Figure 45). Therefore, the first test data for the PC MsS is for the case with part of the TPS debonded. The patch was debonded in successive steps so that the TPS was approximately 50% debonded, 67% debonded, and 100% debonded. The PC MsS data obtained are shown in Figure 46. As can be seen, there is no apparent difference in the signals. The monitoring data are shown in Figure 47. There are differences that can be observed.



Figure 44. Photograph of the space shuttle simulated door panel with the TPS bonded to the door panel. The shuttle tiles use a similar bonding technique.



Figure 45. Photograph of the debonded region of the space shuttle TPS on the door panel. This is designated as a small delamination in the data.

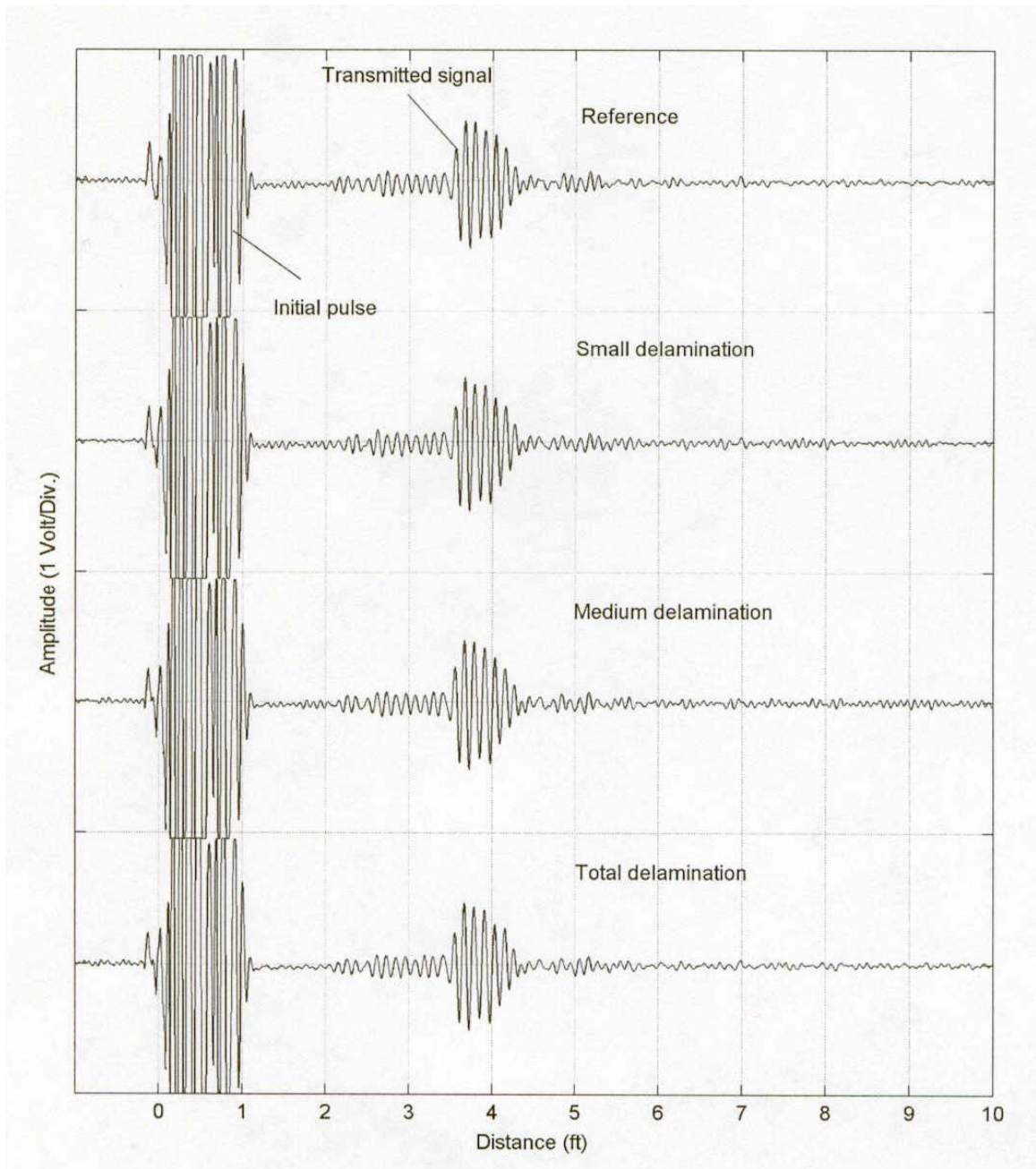


Figure 46. MsS data collected using the PC mode on the space shuttle door panel with the TPS (not the tile) bonded to the surface. The top waveform is the reference taken when the panel had the delamination shown in Figure 45.

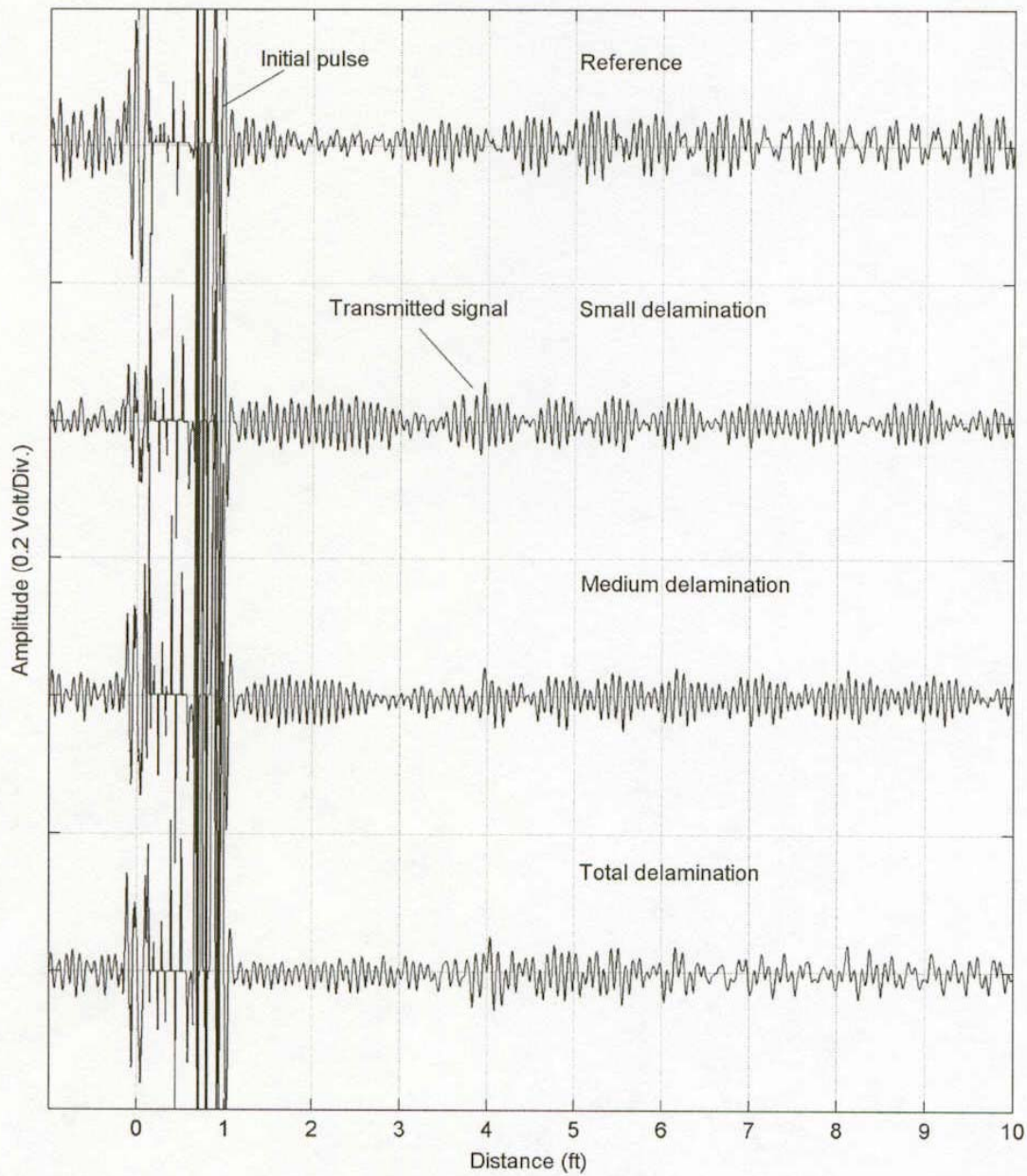


Figure 47. MsS monitoring data obtained by subtracting the reference from another waveform collected with no additional damage (top waveform), subtracting the reference from the waveform where more delamination occurred (second waveform), subtracting the reference from the waveform where more delamination occurred (third waveform), and finally subtracting the reference from the waveform where the small TPS section was totally debonded.

2.4.2 Flat Aluminum Plate with Adhesively Bonded Patch Using PC MsS

The MsS can be used in the PE mode (where one probe serves as both the transmitter and receiver) and the PC mode. In this section of the report, data were collected to evaluate the ability to detect debonding of the adhesively bonded patch. A 12-inch-wide, 34-inch-long, 1/8-inch-thick aluminum plate had a 4-inch by 8-inch-long, 1/16-inch-thick patch bonded to it. Data were collected as illustrated in Figure 48 for six different delamination steps. Steps 1 through 4 were accomplished by inserting a razor blade approximately 1/4 inch into the corner of the patch interface. Steps 5 and 6 were accomplished by inserting the razor blade approximately 1/4 inch into the patch interface and moving it along the entire width of the patch. The final step was the complete removal of the patch.

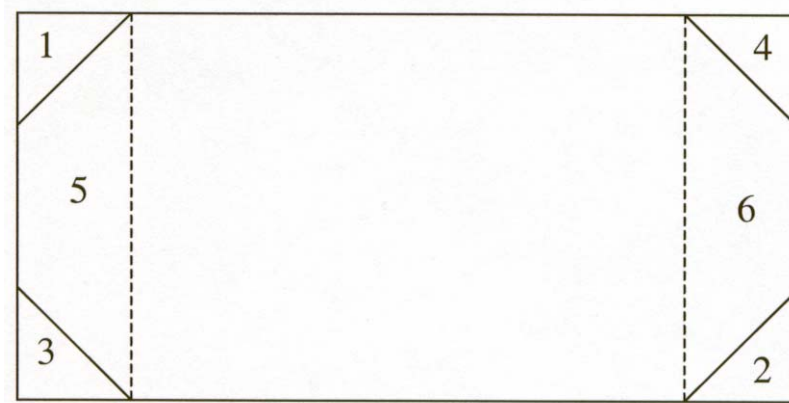


Figure 48. Illustration of six different delamination steps

The inspection and monitoring data for PC MsS mode are shown in Figure 49 and Figure 50. It is difficult to detect even the large delamination in the inspection data. However, in the monitoring data, it is obvious that even the small delamination is detectable. The first two waveforms are denoted as reference minus no delamination as shown in Figure 50. The next waveform shows the reference minus the data obtained when corner 1 was delaminated. The subsequent waveforms show the reference minus the data obtained from delamination processes 2 through 6. Notice that in this case, even the small delamination can be detected in the monitoring mode. Step 7 was when the entire patch was delaminated.

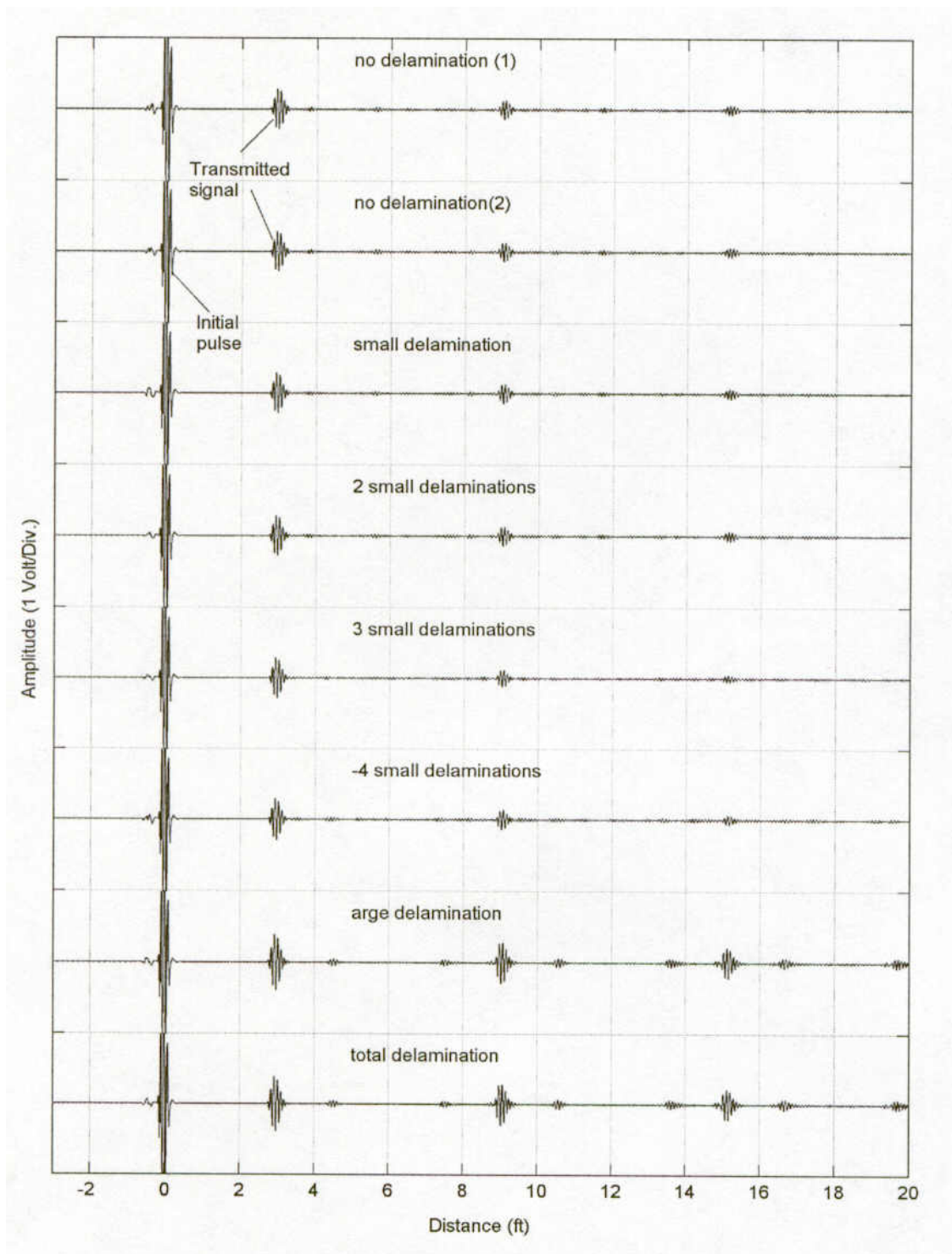


Figure 49. Inspection data obtained from the adhesively bonded patch illustrated in Figure 45 using the PC MsS mode. The first two waveforms are denoted as reference with no delamination. The next waveform shows the reference minus the data obtained when corner 1 was delaminated. The subsequent waveforms show the reference minus the data obtained from delamination processes 2 through 6. Notice that in this case, even the small delamination can be detected in the monitoring mode.

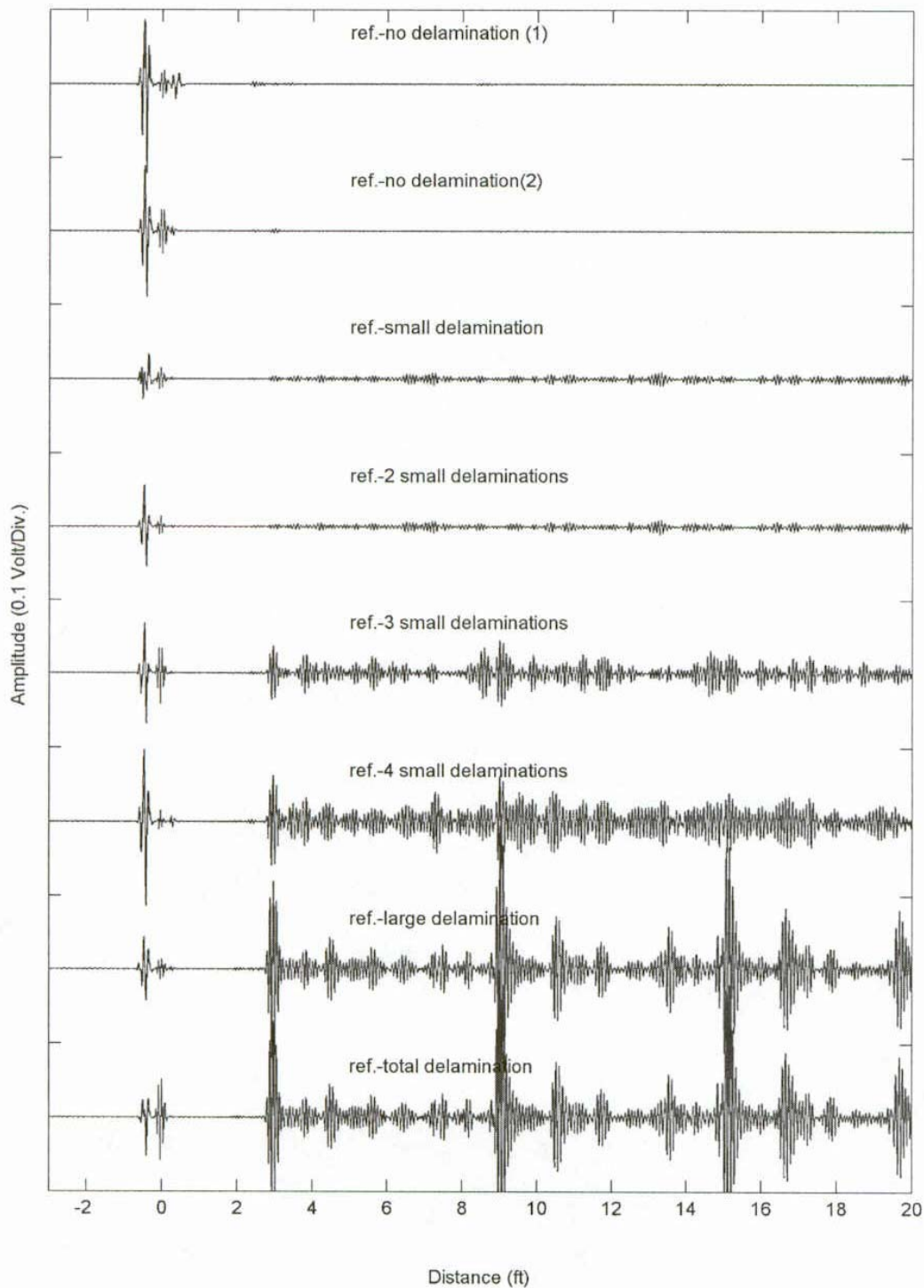


Figure 50. Monitoring data obtained from the adhesively bonded patch illustrated in Figure 45 using the PC MsS mode. The first two waveforms are denoted as reference with no delamination. The next waveform shows the reference minus the data obtained when corner 1 was delaminated. The subsequent waveforms show the reference minus the data obtained from delamination processes 2 through 6. Notice that in this case, even the small delamination can be detected in the monitoring mode.

During the initial investigation of guided waves in bonded structure, it was observed that when the bond between the patch and the aluminum structure was broken, the velocity of the guided wave to the end of the plate seemed to change. A brief explanation of this was that the guided wave entered into the adhesively bonded patch and while the wave was traveling in patched region, the velocity was slightly slower than in the unpatched region. Thus, the velocity change could be used to estimate the bond quality of the patch. This is illustrated in Figure 51. This would mean that the velocity of the guided wave is dependent upon the thickness of the plate. However, theoretically, it is believed that the velocity is thickness independent.

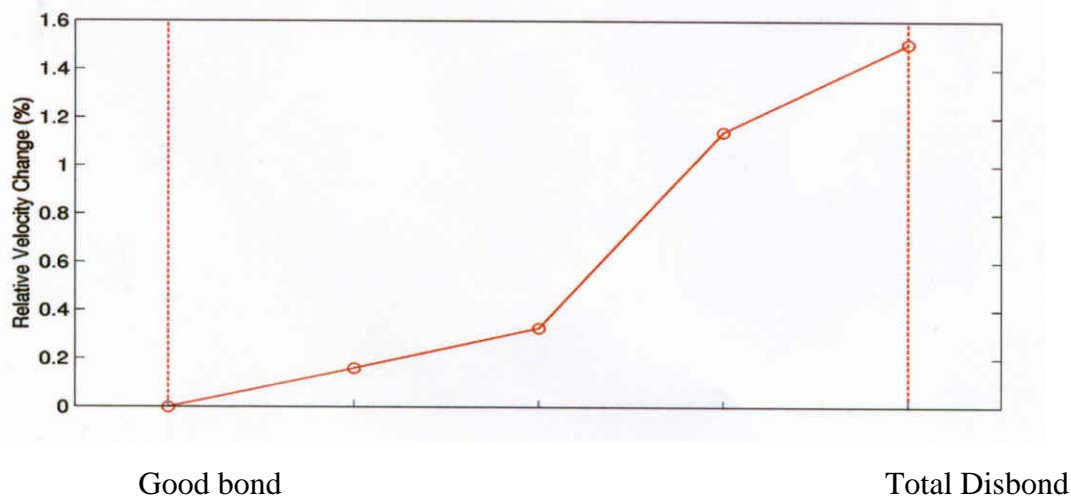


Figure 51. Illustration of change in velocity as a function of bonding quality

A test sample to simulate the bonding was constructed that separated the confusion of the bonding. This consisted of a plate that was 1/4 inch thick, 36 inches long, and 12 inches wide. An MsS nickel strip probe was bonded onto the end of this plate and waveform data were collected. The waveform obtained from the 1/4-inch-thick plate is shown as “condition 1” in Figure 52. Then, much of the thickness of the plate was milled off so that the remaining thickness was 3/16 inch and a region approximately 8 inches wide was not machined down (illustrated in Figure 53). This 8-inch-long region represented the 1/16-inch-thick bonded patch. Then waveform data were collected (shown as condition 2 in Figure 52). Then one more inch of the representative patch region was machined away and waveform data collected (condition 3 in Figure 52). Then a 3-1/2-inch-long region was machined off and another waveform collected (condition 4 in Figure 52). Through careful comparison of the waveforms, it was determined that the velocity did not change as a result of the wave traveling in the thicker portions of the plate.

To attempt to understand if the change in velocity previously observed was still measurable, a 35-inch-long, 12-inch-wide, 3/16-inch-thick plate had 3-12-inch-wide patches bonded to it. The patches were 1 inch long, 3 1/2 inches long and 3 1/2 inches long. Data were collected with all the patches bonded (condition 5 in Figure 52), after the 1 inch patch was removed (condition 6 in Figure 52), after one of the 3 1/2 inch patches was removed (condition 7 in Figure 52), and after all the patches had been removed (condition 8 in Figure 52). The results showed that a velocity change had occurred. This can only be explained by the interaction of the bonded patch-to-substrate sandwich.

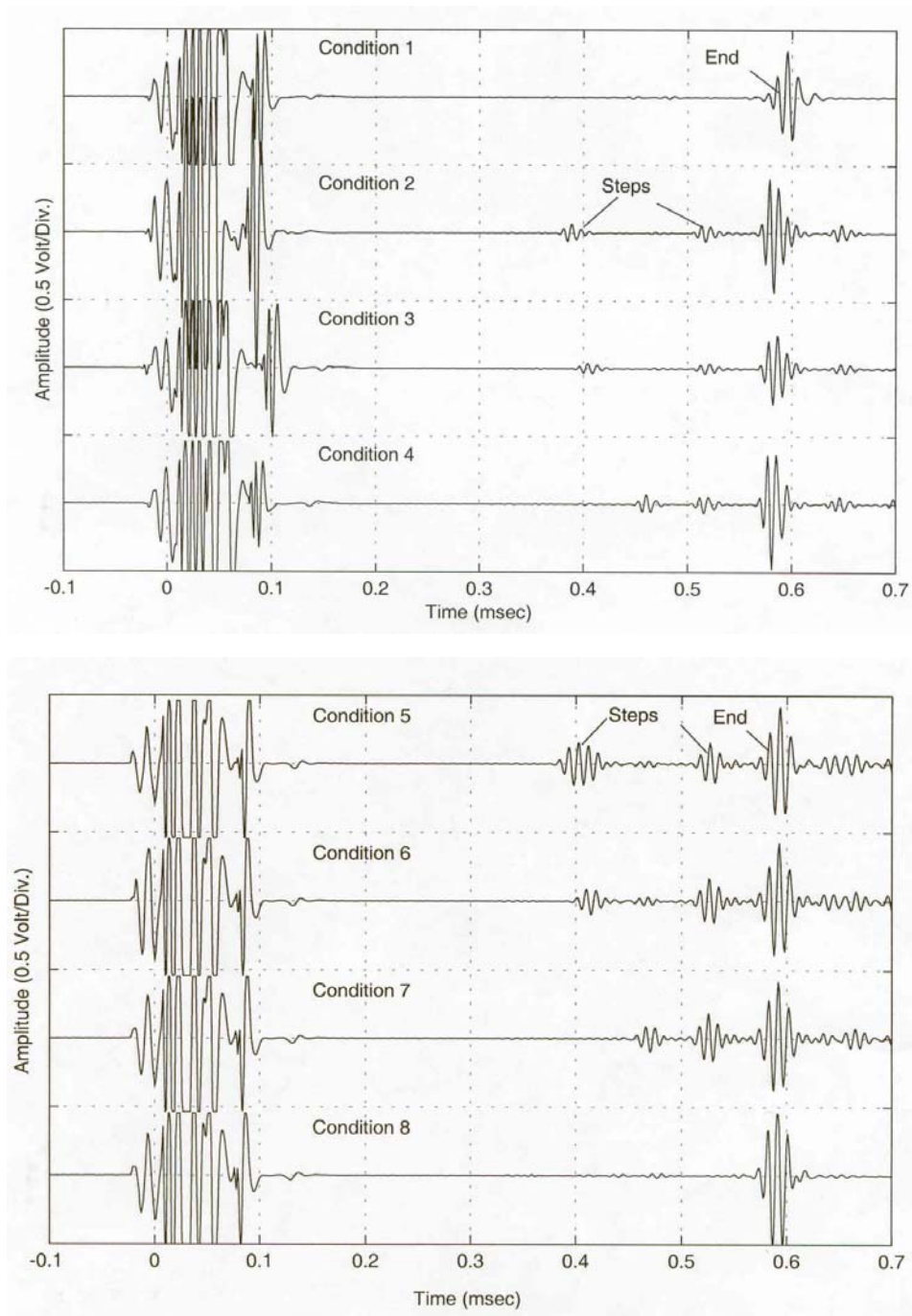


Figure 52. Waveform data obtained from simulated bond structure (conditions 1 through 4) and bonded structure (conditions 5 through 8) with materials being removed to simulate debonding

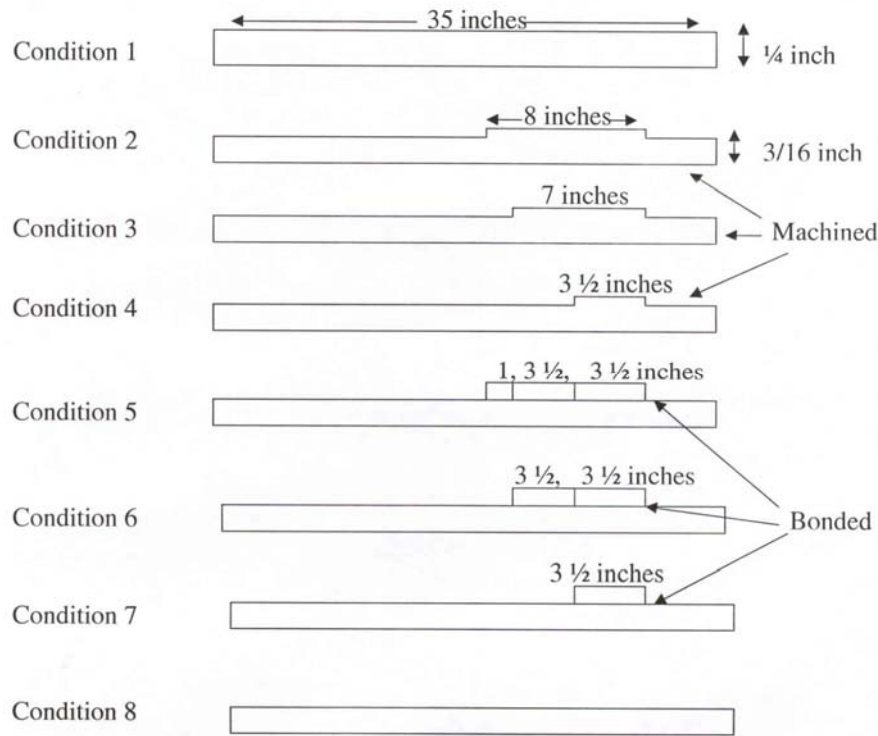


Figure 53. Illustration of process used to evaluate the effect of bonding on guided wave velocity

The PE MsS inspection data and monitoring results obtained for each patch delamination step illustrated in Figure 48 are shown in Figures 54 through 62. Figure 54 shows the reference data compared to another data set collected before disbonding. This clearly shows in the subtracted data no change between the reference and the bonded patch data. Figure 55 shows a slight change in the inspection waveform (called “monitoring data”) at a distance of approximately 23 inches from the end of the plate, but clearly the subtracted data shows distinct evidence of debonding at 23 inches. Figure 56 shows more difference between the initial bonded reference waveform than observed in Figure 55, but it does not show that the change is due to a debond at the end of the patch. Figure 57 is a plot of the same data except the data obtained from the debond at the end of the plate is compared to the data obtained from the debond at the front of the plate. This clearly shows a difference in the two signals and that the difference is due to a change of bonding at approximately 30 inches which is where the end of the patch is located. Similar data obtained from the other debonding experiments (Figures 58 through 61) show that the amount of difference between the initial reference and the various amounts of debonding increases with the amount of debonding. Finally, in Figure 59 where the entire patch has been removed, the subtracted signal looks almost identical to the reference signal. These data clearly indicate that the MsS can be used to see small changes in patch bonding.

Compensation Method: No Reference
Reference Signal Location: --
Velocity Difference: -- %
Amplitude Difference: -- %
Origin: -1.00 ft
Velocity: 127.95 ft

Frequency: 128 kHz
Filter: 128 kHz
Total Gain: 10 dB
Pulse Rate: 16
Cycles: 1
Amp: 20 percent

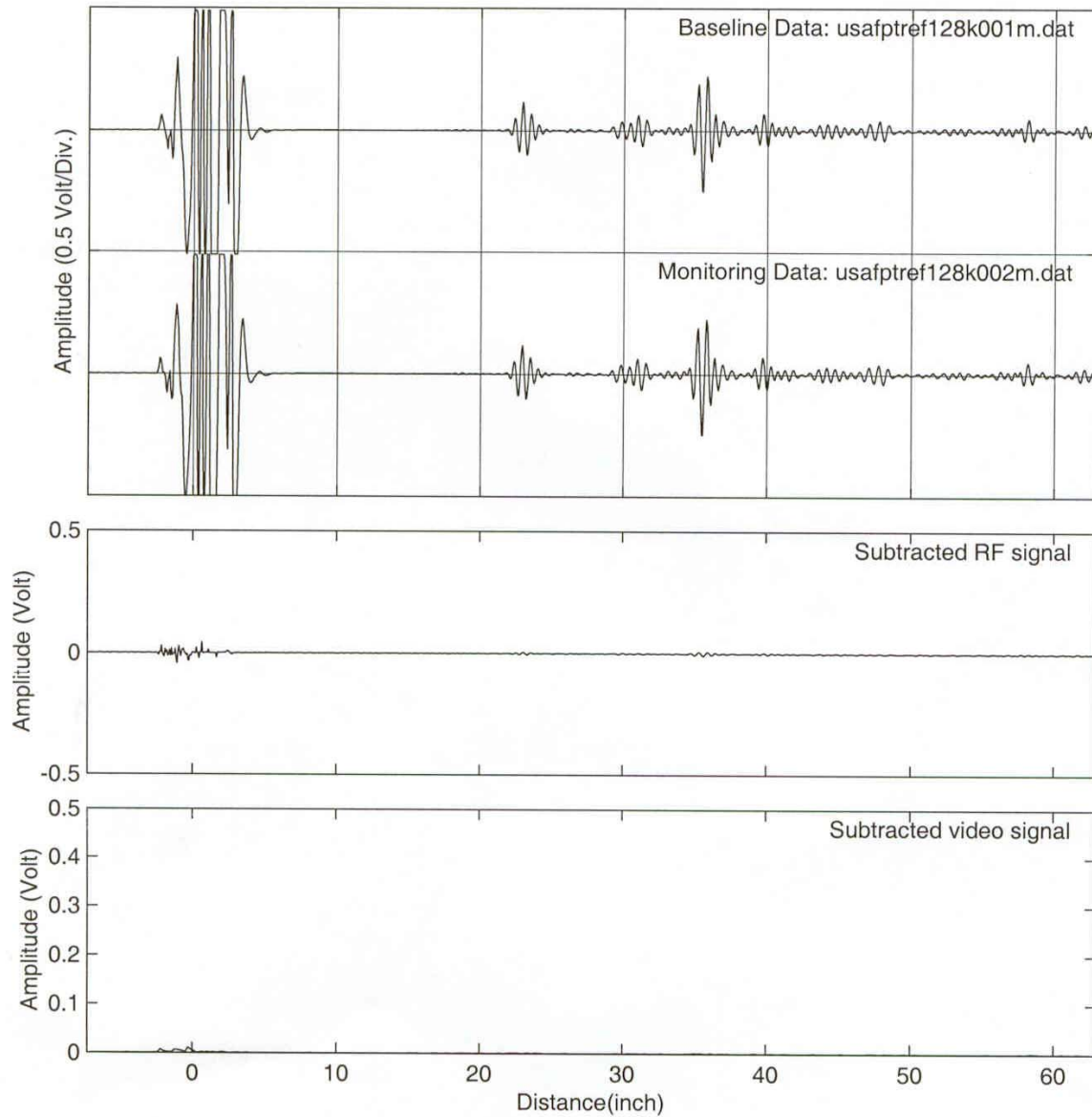


Figure 54. Reference data compared to another data set collected before disbonding

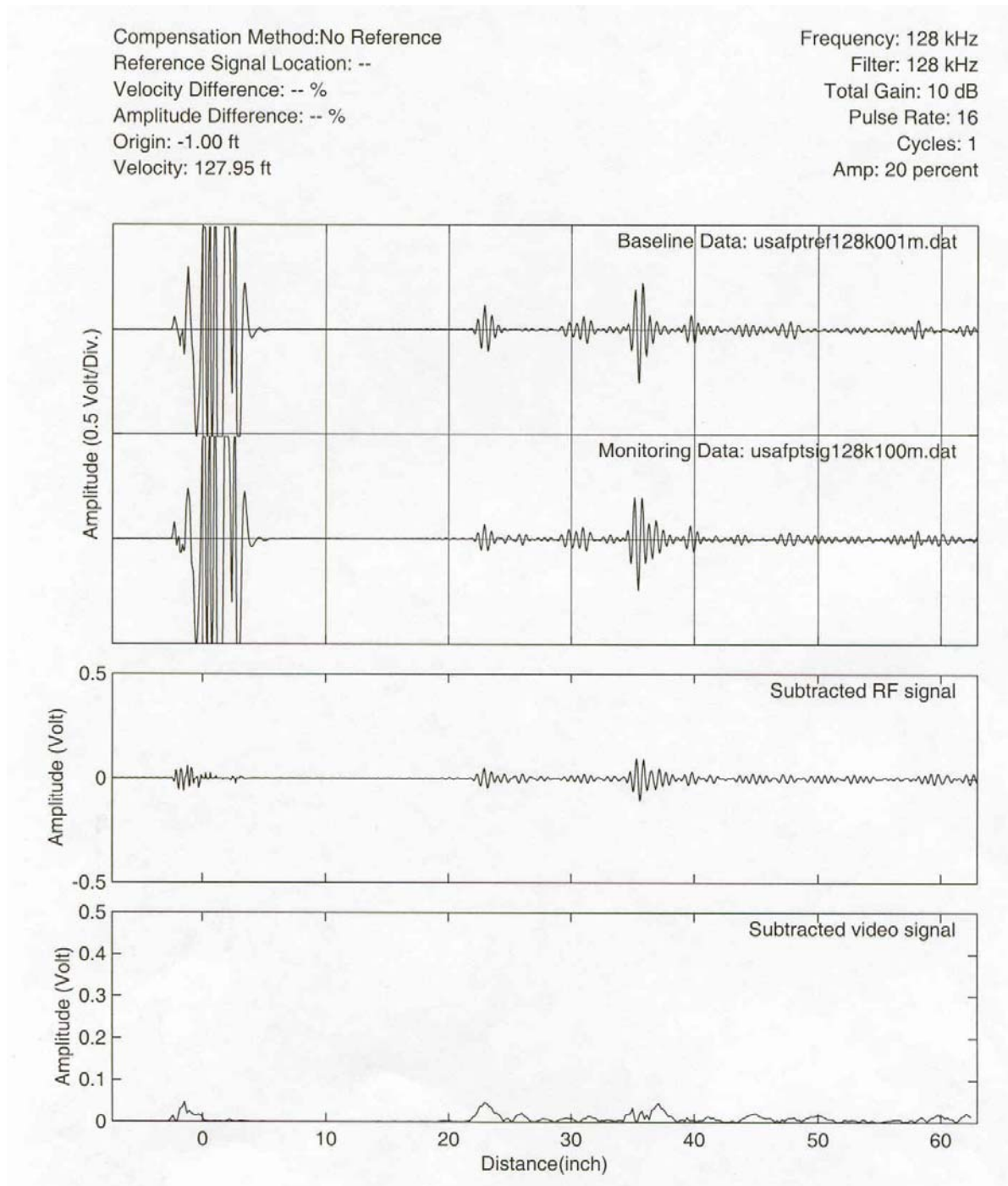


Figure 55. Inspection waveform (called monitoring data) showing a slight change at a distance of approximately 23 inches from the end of the plate

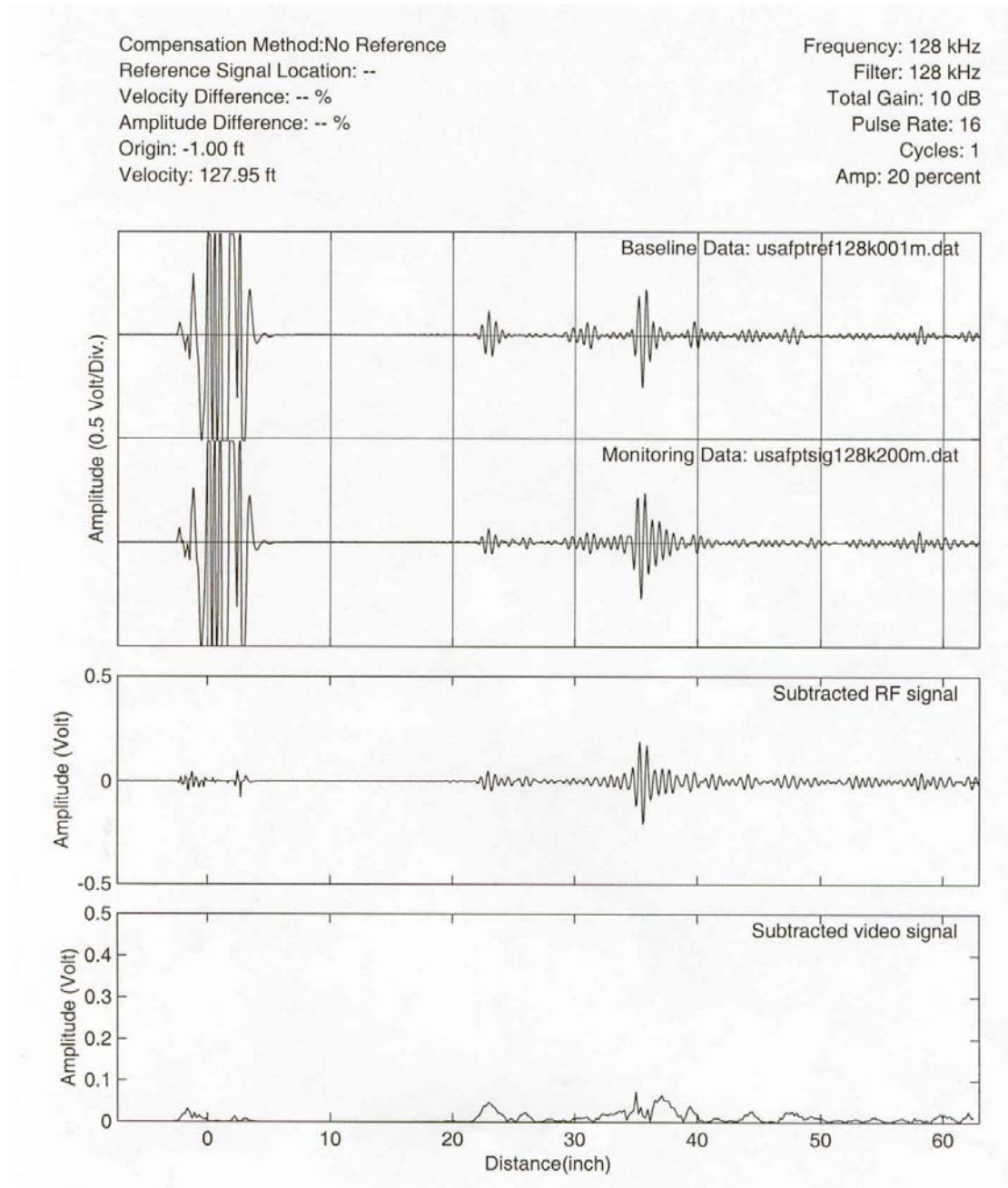


Figure 56. Top trace is the reference signal with no delaminations and monitoring data is from step 2 of the delamination process. The subtracted RF signal is the difference between the reference signal and the step 2 delamination process, showing a difference but not what is the difference relative to step 1 of the delamination process.

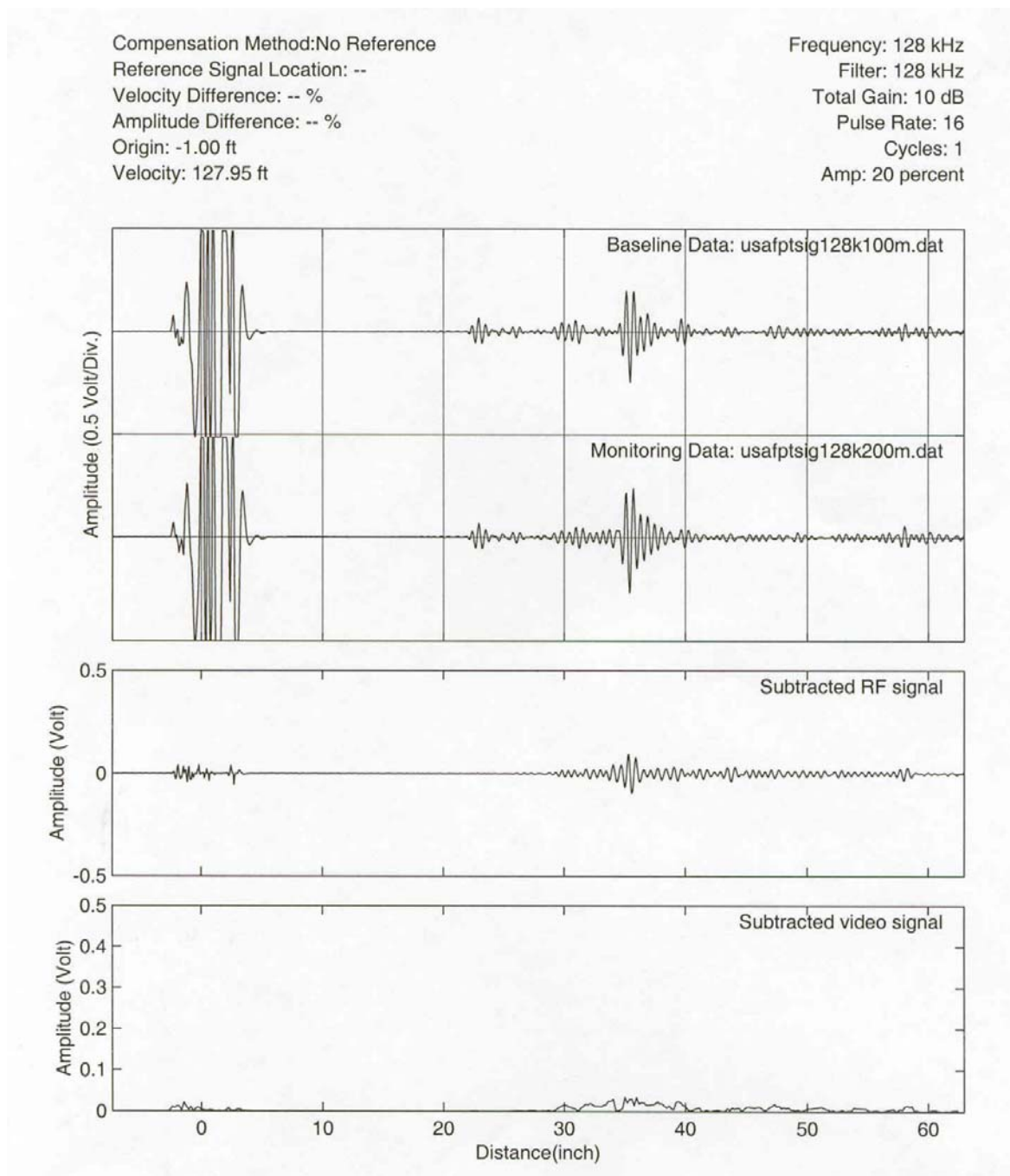


Figure 57. Top trace is data collected from step 1 of the delamination process and monitoring data is from step 2 of the delamination process. The subtracted RF signal is the comparison of the delamination data from delamination steps 1 and 2, clearly showing the difference and that the difference occurs at the back of the patch.

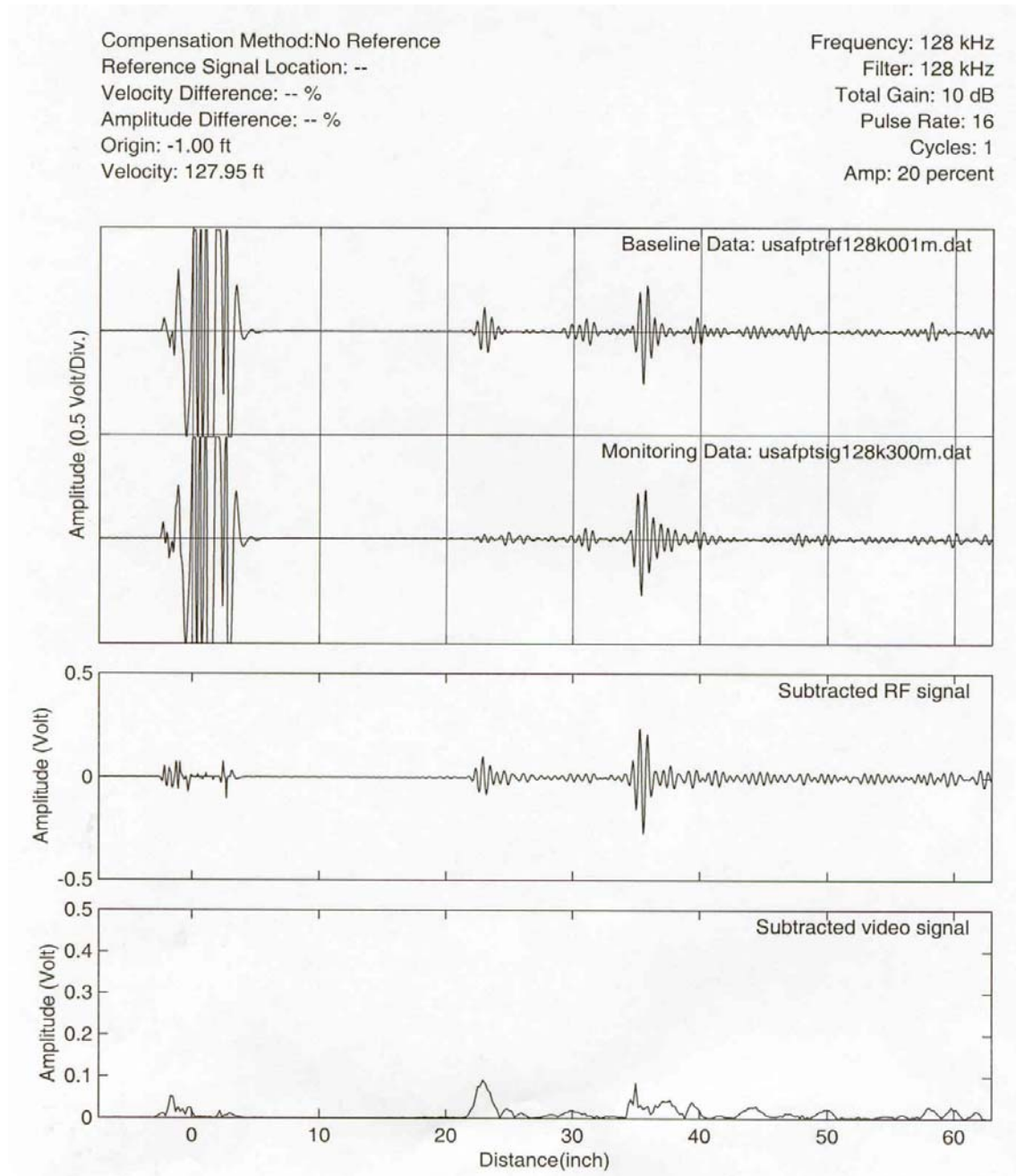


Figure 58. Top trace is the reference signal with no delaminations and monitoring data is from step 3 of the delamination process. The subtracted RF signal is the difference between the reference signal and the step 3 delamination process, showing a difference but not what is the difference relative to steps 1 or 2 of the delamination process. The data from steps 1 or 2 could be used to determine what is the difference relative to each of those steps.

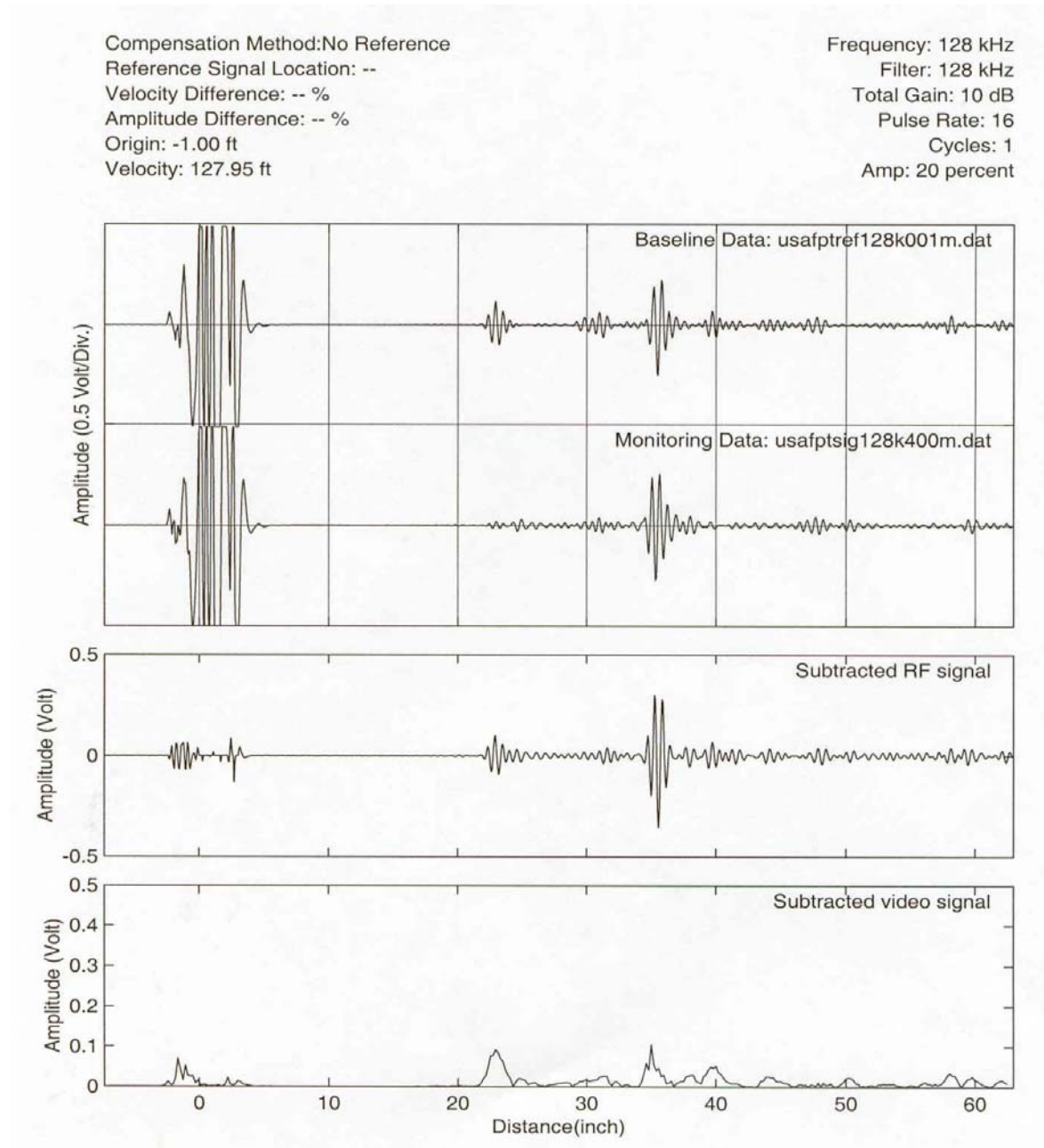


Figure 59. Top trace is the reference signal with no delaminations and monitoring data is from step 4 of the delamination process. The subtracted RF signal is the difference between the reference signal and the step 4 delamination process, showing a difference but not what is the difference relative to steps 1, 2 or 3 of the delamination process. The data from steps 1, 2 or 3 could be used to determine what is the difference relative to each of those steps.

Compensation Method: No Reference
Reference Signal Location: --
Velocity Difference: -- %
Amplitude Difference: -- %
Origin: -1.00 ft
Velocity: 127.95 ft

Frequency: 128 kHz
Filter: 128 kHz
Total Gain: 10 dB
Pulse Rate: 16
Cycles: 1
Amp: 20 percent

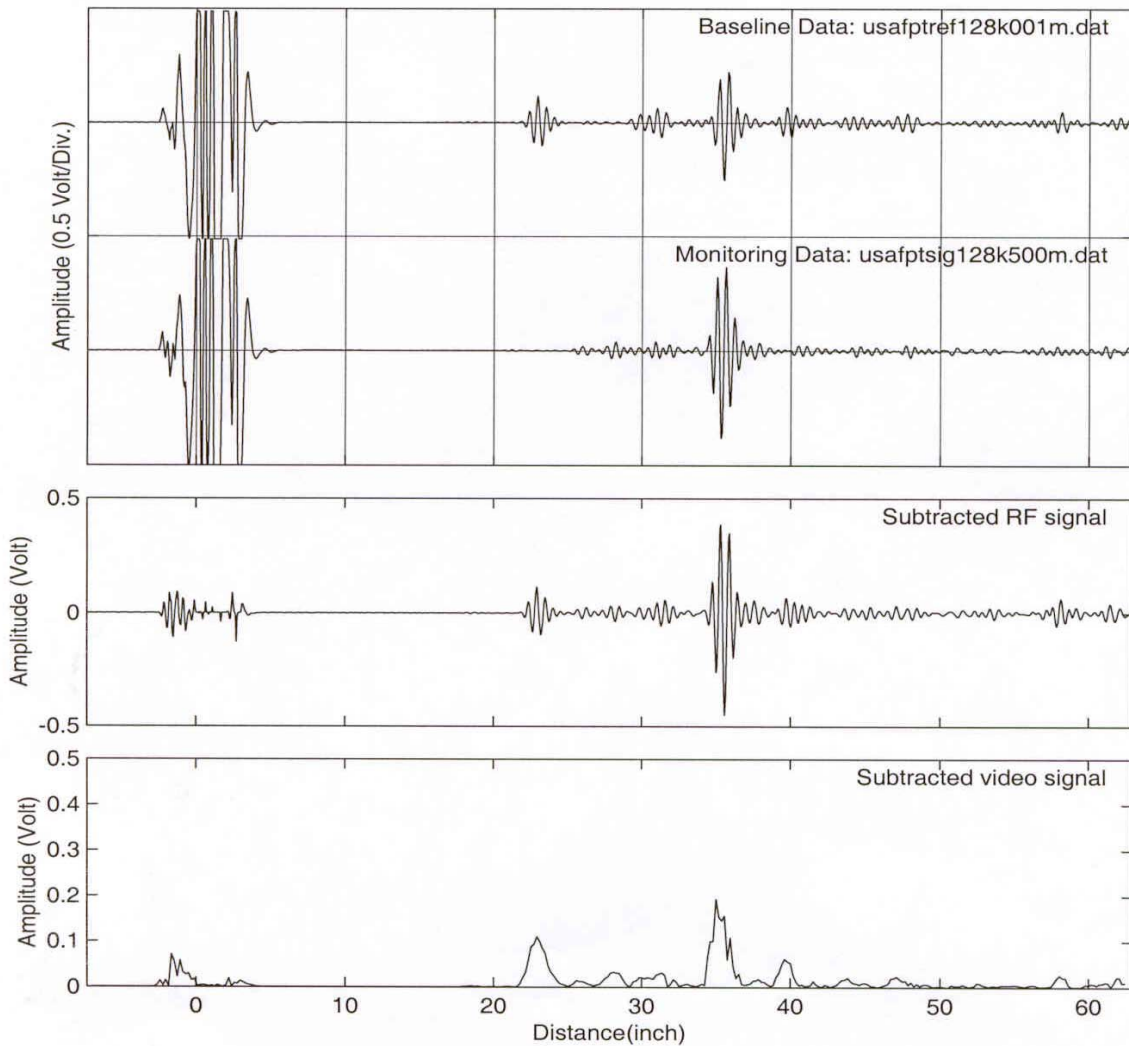


Figure 60. Top trace is the reference signal with no delaminations and monitoring data is from step 5 of the delamination process. The subtracted RF signal is the difference between the reference signal and the step 5 delamination process, showing a difference but not what is the difference relative to steps 1, 3, or 4 of the delamination process. The data from steps 1, 2, 3 or 4 could be used to determine what is the difference relative to each of those steps.

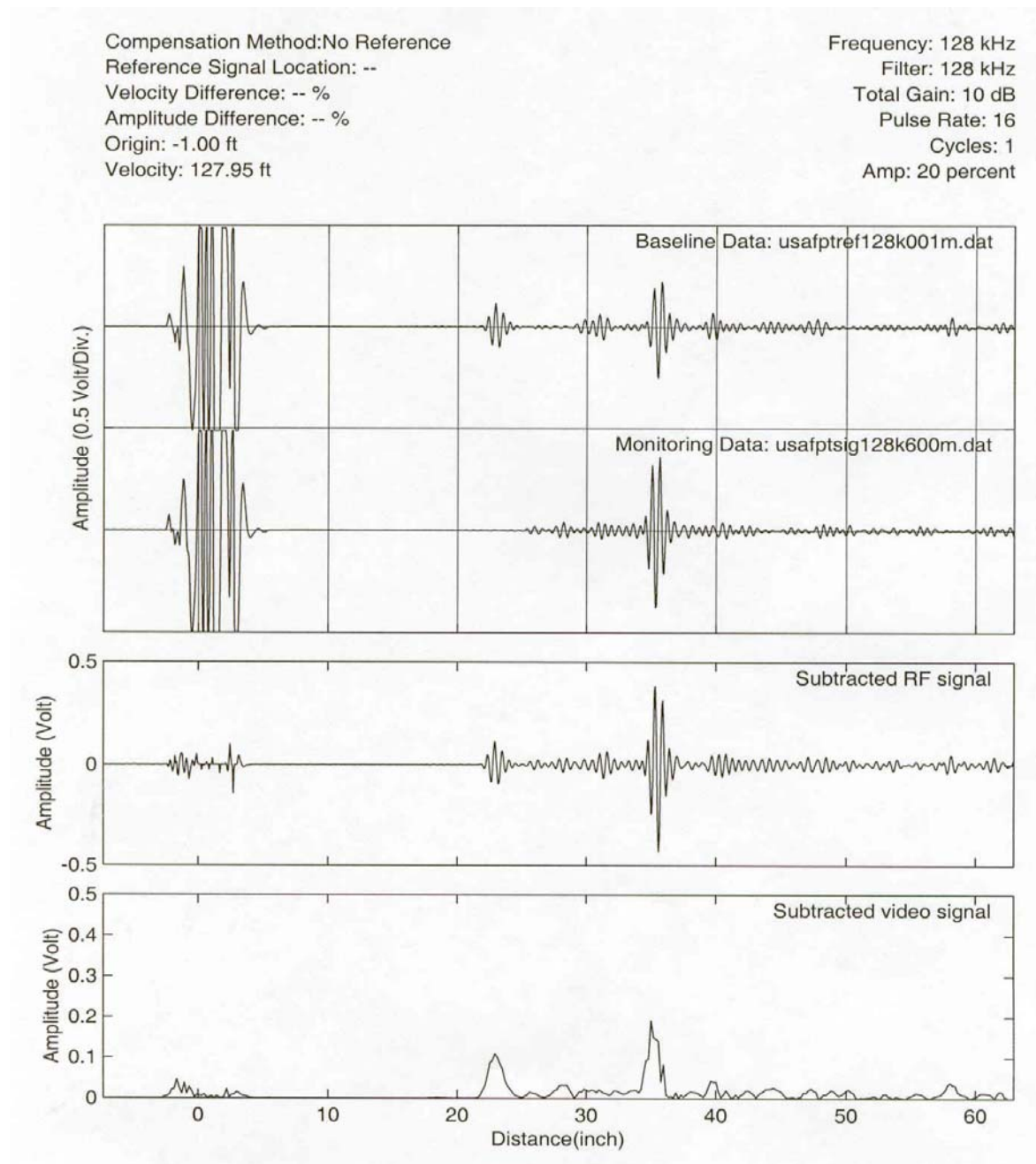


Figure 61. Top trace is the reference signal with no delaminations and monitoring data is from step 6 of the delamination process. The subtracted RF signal is the difference between the reference signal and the step 6 delamination process. There is a large difference.

Compensation Method: No Reference
Reference Signal Location: --
Velocity Difference: -- %
Amplitude Difference: -- %
Origin: -1.00 ft
Velocity: 127.95 ft

Frequency: 128 kHz
Filter: 128 kHz
Total Gain: 10 dB
Pulse Rate: 16
Cycles: 1
Amp: 20 percent

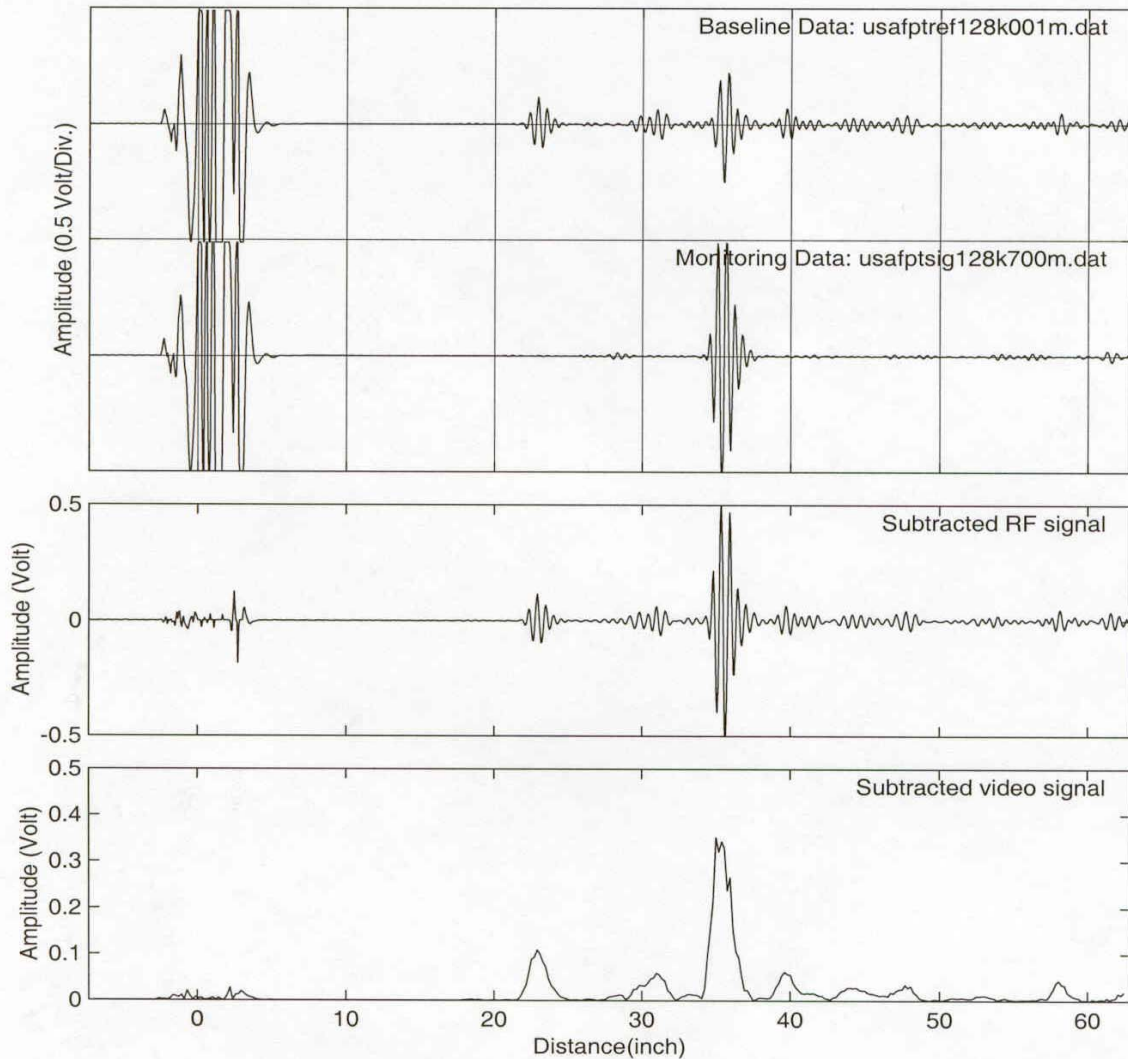


Figure 62. Top trace is the reference signal with no delaminations and monitoring data is from step 7 of the delamination process. The subtracted RF signal is the difference between the reference signal and the step 7 delamination process. There is a large difference.

2.4.3 Work on Detection of Defect Growth Under the Patch Using MsS

Tests were conducted on an aluminum plate with an adhesively bonded aluminum patch to determine whether the MsS monitoring approach could detect changes in defect length under the patch of approximately 0.1 inch. The test plate was 34 inches long, ¼ inch thick, and 12 inches wide. The patch was 8 inches long, 1/16 inch thick, and 4 inches wide. The edges of the patch were tapered as illustrated in Figure 63. An MsS nickel strip was placed

at the end of the plate. Reference data were collected from the test sample using the MsS before a notch was placed on the backside of the $\frac{1}{4}$ -inch-thick plate at a location approximately in the geometrical middle of the patch. The initial notch size was approximately $\frac{1}{2}$ inch long by $\frac{1}{8}$ inch deep, and the length of the notch was sequentially increased in steps of approximately 0.1 inch. MsS waveform data were collected from the notch as it increased from $\frac{1}{2}$ inch to 1.0 inch long in successive steps of 0.1 inch. The waveforms collected and the differences observed using the monitoring waveform subtraction algorithm for various notch lengths are shown in Figures 64 through 72.



Figure 63. Photograph of the adhesively bonded patch on an aluminum substrate showing the beveled edges. The patch is approximately 8 inches long, 4 inches wide, and $\frac{1}{16}$ inch thick.

The waveform data shown in Figure 64 are two reference waveforms prior to the notch being placed underneath the patch. The monitoring waveform difference shows only a small change difference in the waveforms. The waveform data shown in Figure 65 is a comparison of the reference waveform data and the waveform data obtained after the $\frac{1}{2}$ -inch-long defect was placed under the patch. The monitoring data clearly show a large signal difference that occurs at approximately 28 inches from the MsS (which corresponds to the location of the $\frac{1}{2}$ -inch-long defect). Clearly, the defect is not seen in the monitoring data (second waveform in the plot identified as `usafntsig128K001m.dat`).

The waveform data in Figure 66 is from the notch that has been increased by 0.1 inch to a total length of 0.6 inch. When compared to the reference for no defect, again the defect appears clearly in the monitoring data at approximately 28 inches. However, it is difficult to see any difference between monitoring signals obtained between the 0.5- and 0.6-inch-long signals when the monitoring signal is individually compared to the reference signal where there is no defect under the patch. Similar observations can be made for the waveforms in Figures 67 through 70 where the notch is increasing in length from 0.6 inch to 1 inch. However, when the reference

data is chosen as the data from when the defect was 0.5 inch long and the question to be answered is whether a change in the defect length of 0.1 inch can be observed, then the true comparison should be between the waveforms obtained from 0.5- and 0.6-inch-long defect conditions. Figure 71 shows the waveform data and the monitoring data comparing the waveforms from the 0.5-inch and 0.6-inch-long defects. This clearly shows that defect change in length of 0.1 inch can be detected in the monitoring mode. Figure 72 shows similar monitoring data between the case where the defect is 0.5 inch long and 0.7 inch long. As can be observed, the fact that a difference is present can easily be detected. However, the actual amount of change in the defect is not obvious.

2.4.4 Defects Under Fasteners

Using the ¼-inch-thick flat plate with a large number of tapered fastener holes previously used for MsS experiments, another line of additional holes was drilled into the plate approximately 2 inches from the first set of holes. Tapered head, threaded fasteners were placed in the holes and tightened. This test plate is shown in Figure 73. Two reference data waveforms were collected. These waveforms are shown in Figure 74 along with the difference of the two waveforms. As can be seen, basically a flat line difference was obtained. The goal of this test was to determine the detection sensitivity to simulated corrosion. To accomplish this goal, a small corrosion-type defect (estimated to be approximately 0.01 inch deep by 0.02 inch diameter) in area was placed in a hole approximately 20 inches from the sensors using a pointed punch and a slight hammer blow.

The fastener was put back in the hole and MsS data collected. The waveform obtained is shown as the second waveform in Figure 75. It is impossible to visually detect any difference between the baseline data and the monitoring data. However, when the difference of the waveforms is obtained, the small defect is clearly observed at approximately 20 inches from the MsS. The fastener was then removed and the corrosion region made larger (estimated to be approximately 0.01 inch deep by 0.03 inch diameter). The fastener was put back in and MsS data collected. The waveform data obtained is shown as the monitoring waveform in Figure 76. Again, it is impossible to visually detect any difference between the baseline and monitoring waveforms. However, when the difference is taken, the defect is clearly observed at 20 inches from the MsS.

Similar data were obtained after the defect was increased to an estimated size of 0.02 inch by 0.050 inch by 0.1 inch and 0.025 by 0.08 inch diameter. The defects are shown in Figures 77 and 78. The corresponding waveform data are shown in Figures 79 and 80 as the monitoring waveforms. Again, it impossible to visually detect any differences between these waveforms and the baseline data; however the monitoring data clearly show the defect.

This clearly showed that in the inspection mode the largest simulated defect (the 0.02 by 0.05 by 0.1) could not be detected while in the monitoring mode, even the smallest change in the defect, i.e., 0.003 by 0.01 inch diameter, could be detected.

Since this high defect detection sensitivity was not really expected, another set of data was obtained in an attempt to confirm these results. For this case, the waveform data with the large defect in the hole at 20 inches from the MsS was used as the reference data. A small defect (0.01 inch by 0.03 inch diameter) was placed in the hole approximately 32 inches from the MsS. The fastener was reinstalled and tightened. The waveform obtained is shown in Figure 81. Again, it is impossible to visually detect any

difference between the monitoring data and the baseline data. However, when the difference is obtained, the defect clearly is detected at approximately 32 inches from the MsS. Similar results are obtained when the defect is increased in two steps to approximately 0.03-inch by 0.05-inch diameter. These data are shown in Figure 82 and Figure 83.

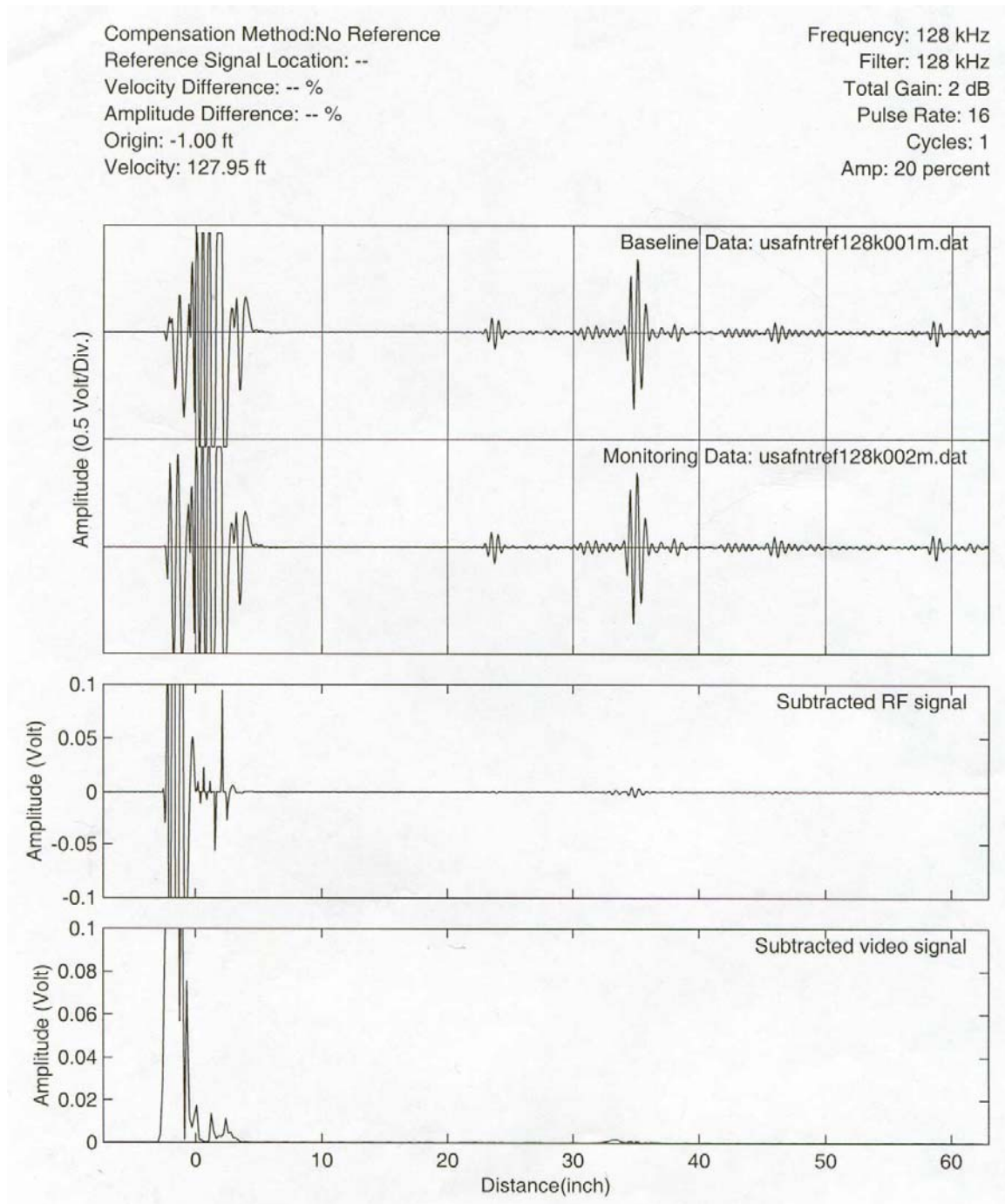


Figure 64. MsS waveform and monitoring data comparing two data sets for the case of no defect under the adhesively bonded aluminum patch

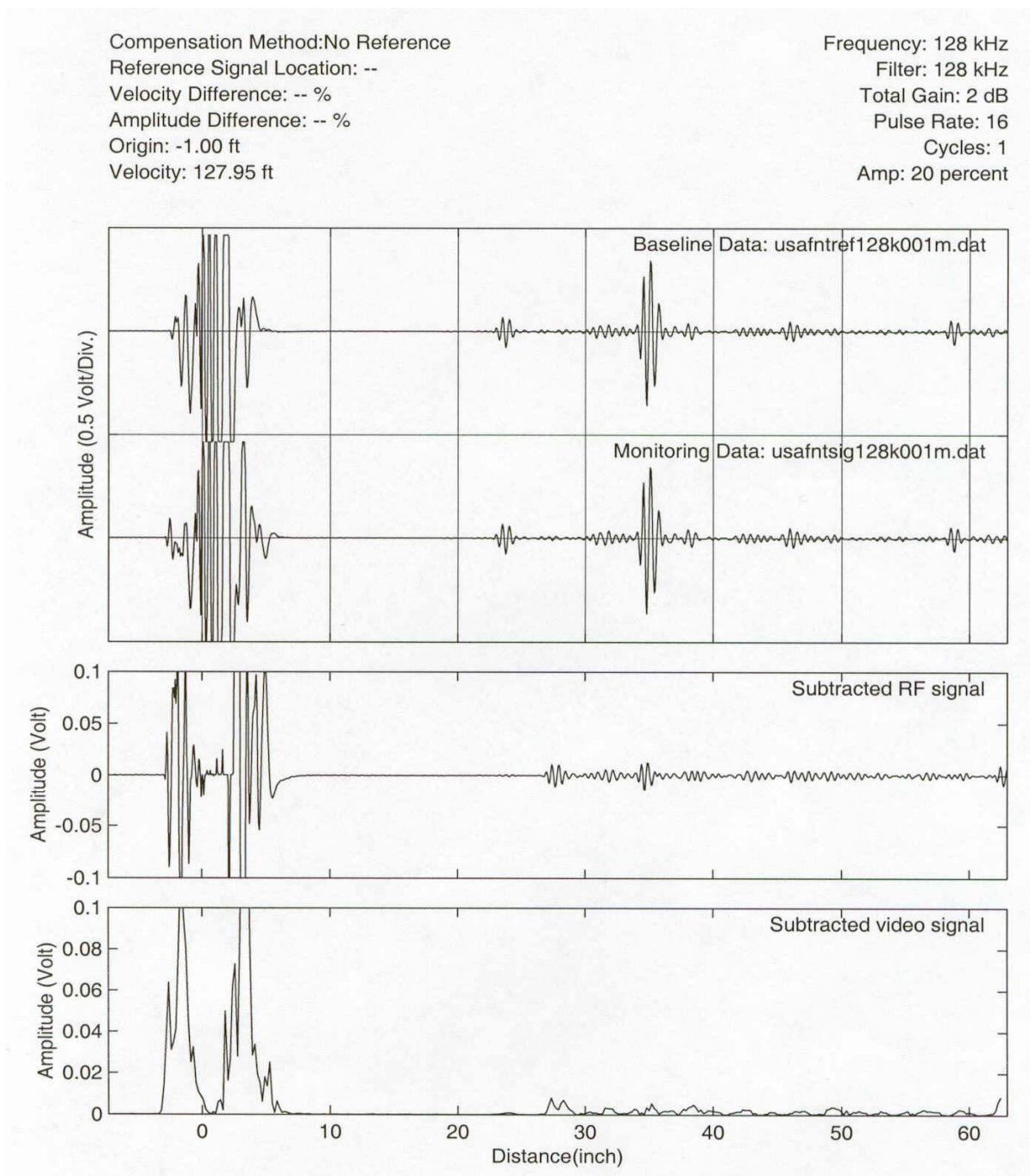


Figure 65. MsS waveform and monitoring data comparing the case of no defect under the adhesively bonded aluminum patch to the case where a 0.5-inch-long, 1/8-inch-deep defect was placed below the adhesively bonded aluminum patch

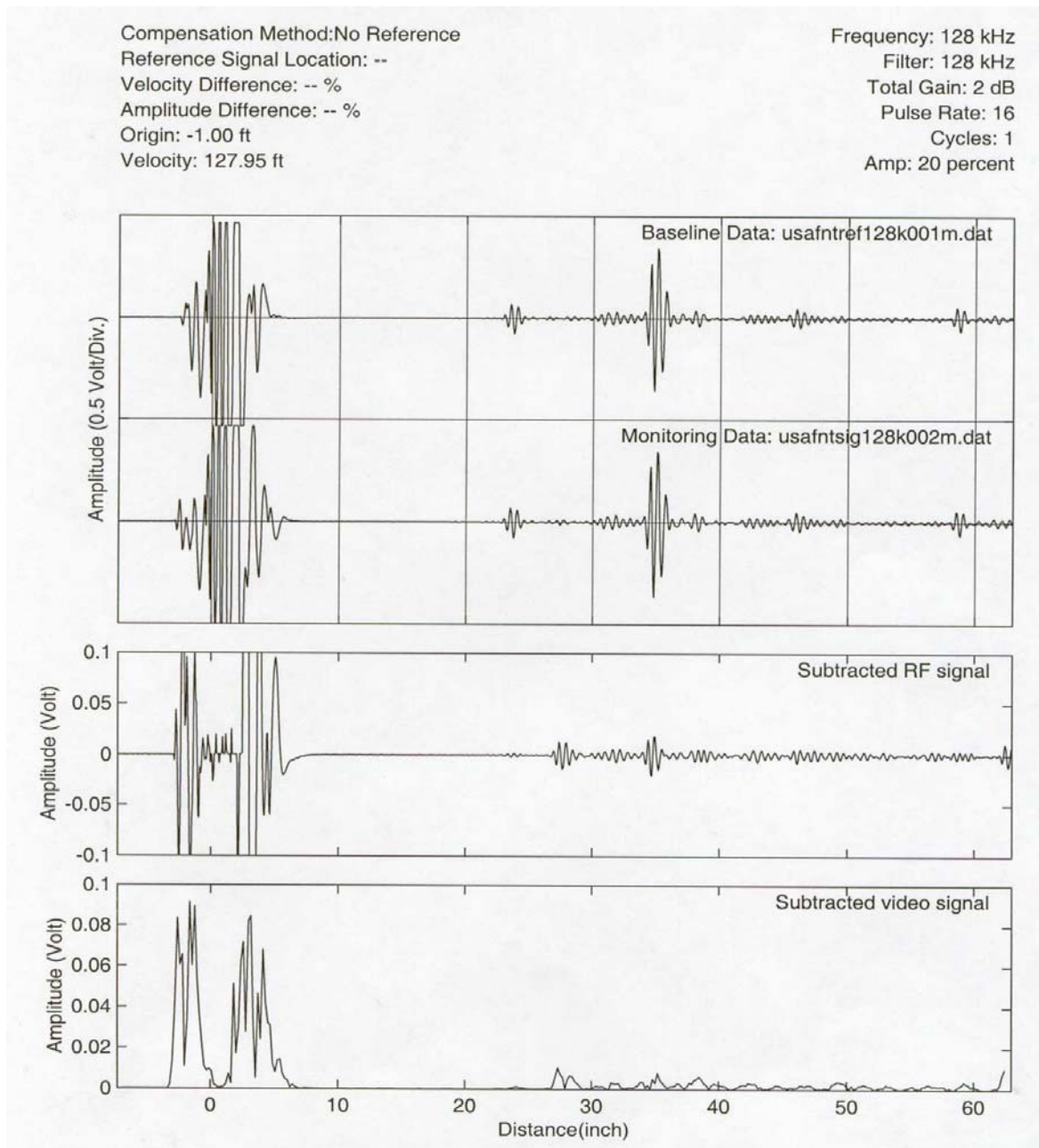


Figure 66. MsS waveform and monitoring data comparing the case of no defect under the adhesively bonded aluminum patch to the case where a 0.6-inch-long, 1/8-inch-deep defect was placed below the adhesively bonded aluminum patch

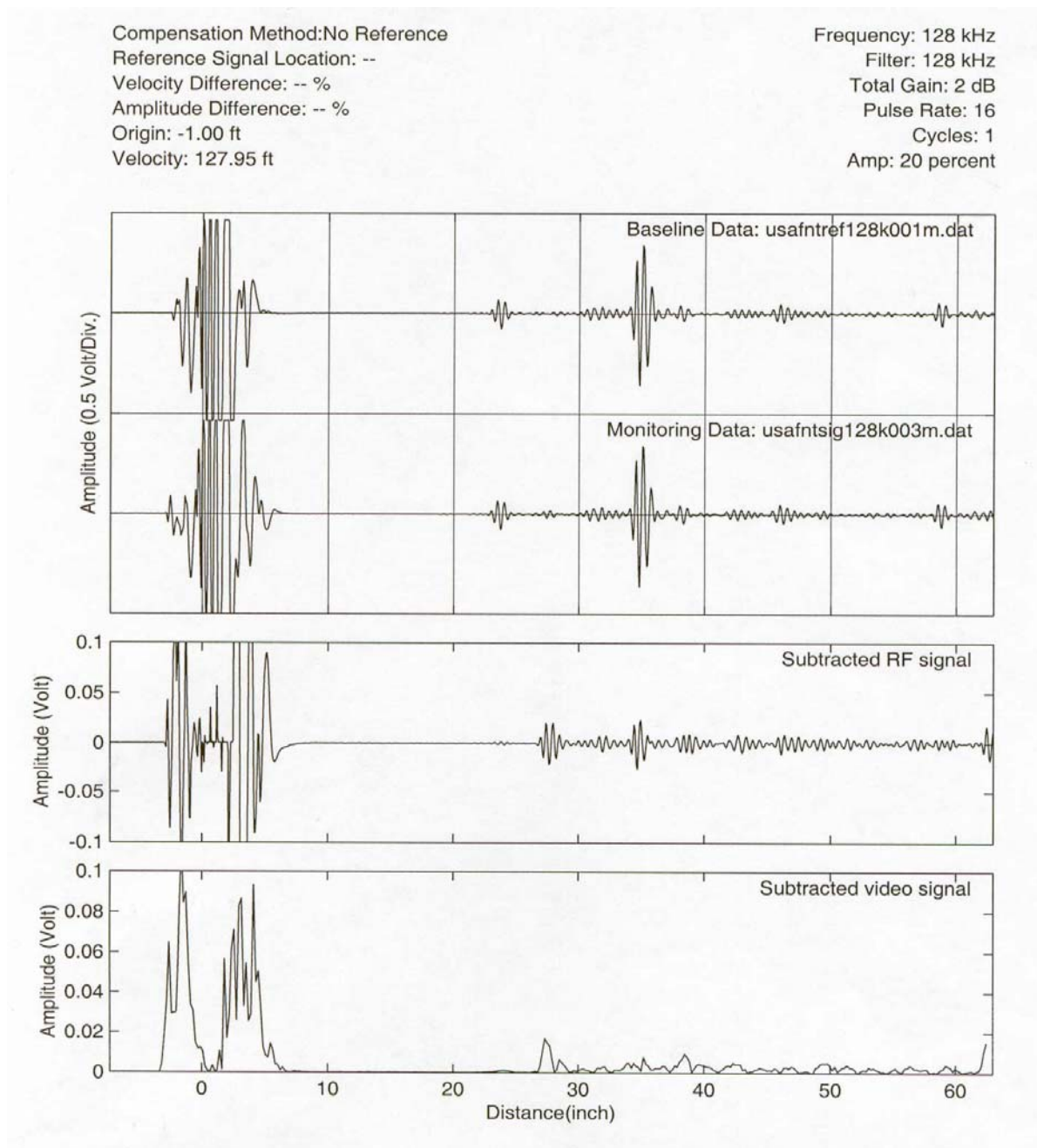


Figure 67. MsS waveform and monitoring data comparing the case of no defect under the adhesively bonded aluminum patch to the case where a 0.7-inch-long, 1/8-inch-deep defect was placed below the adhesively bonded aluminum patch

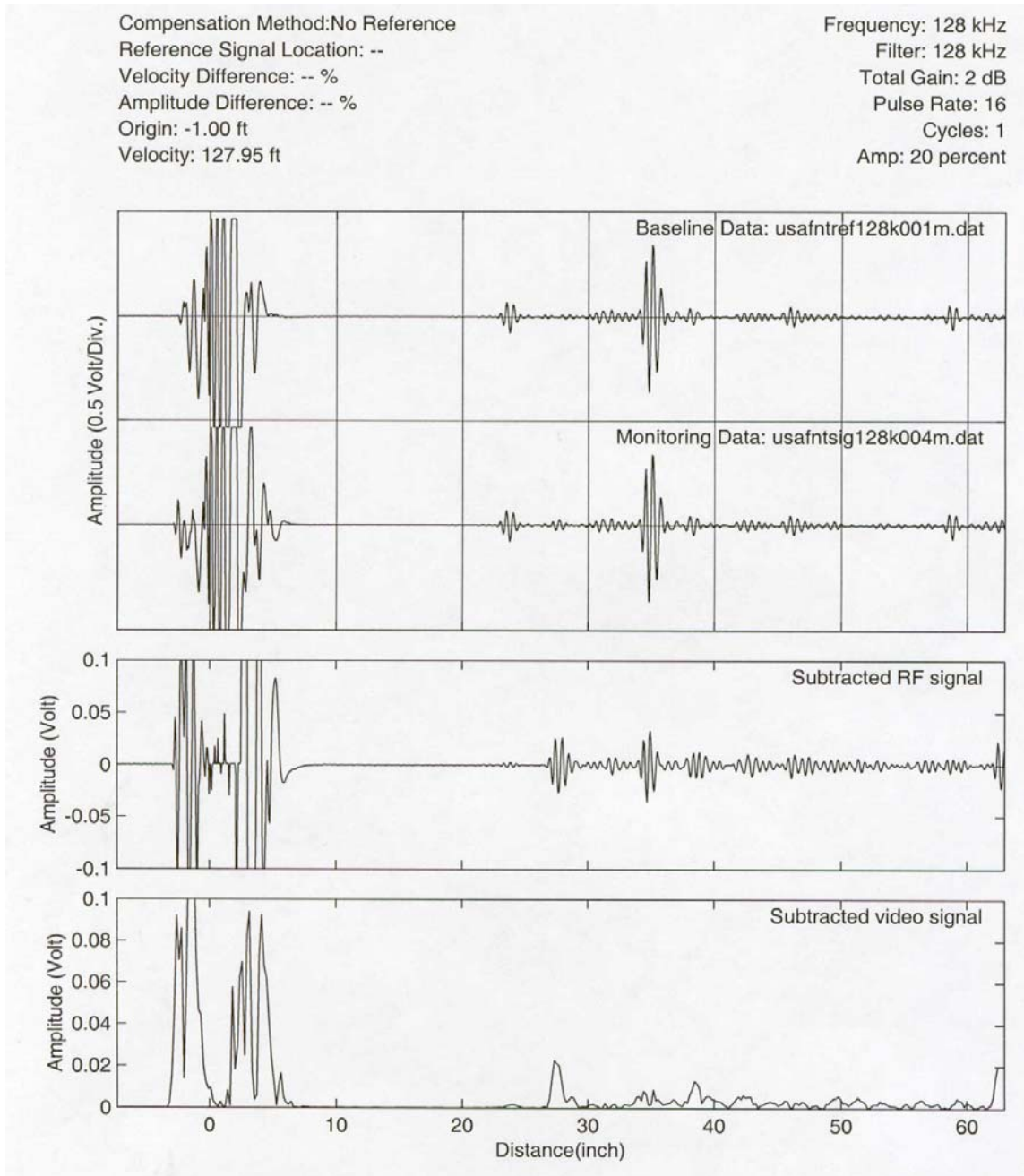


Figure 68. MsS waveform and monitoring data comparing the case of no defect under the adhesively bonded aluminum patch to the case where a 0.8-inch-long, 1/8-inch-deep defect was placed below the adhesively bonded aluminum patch

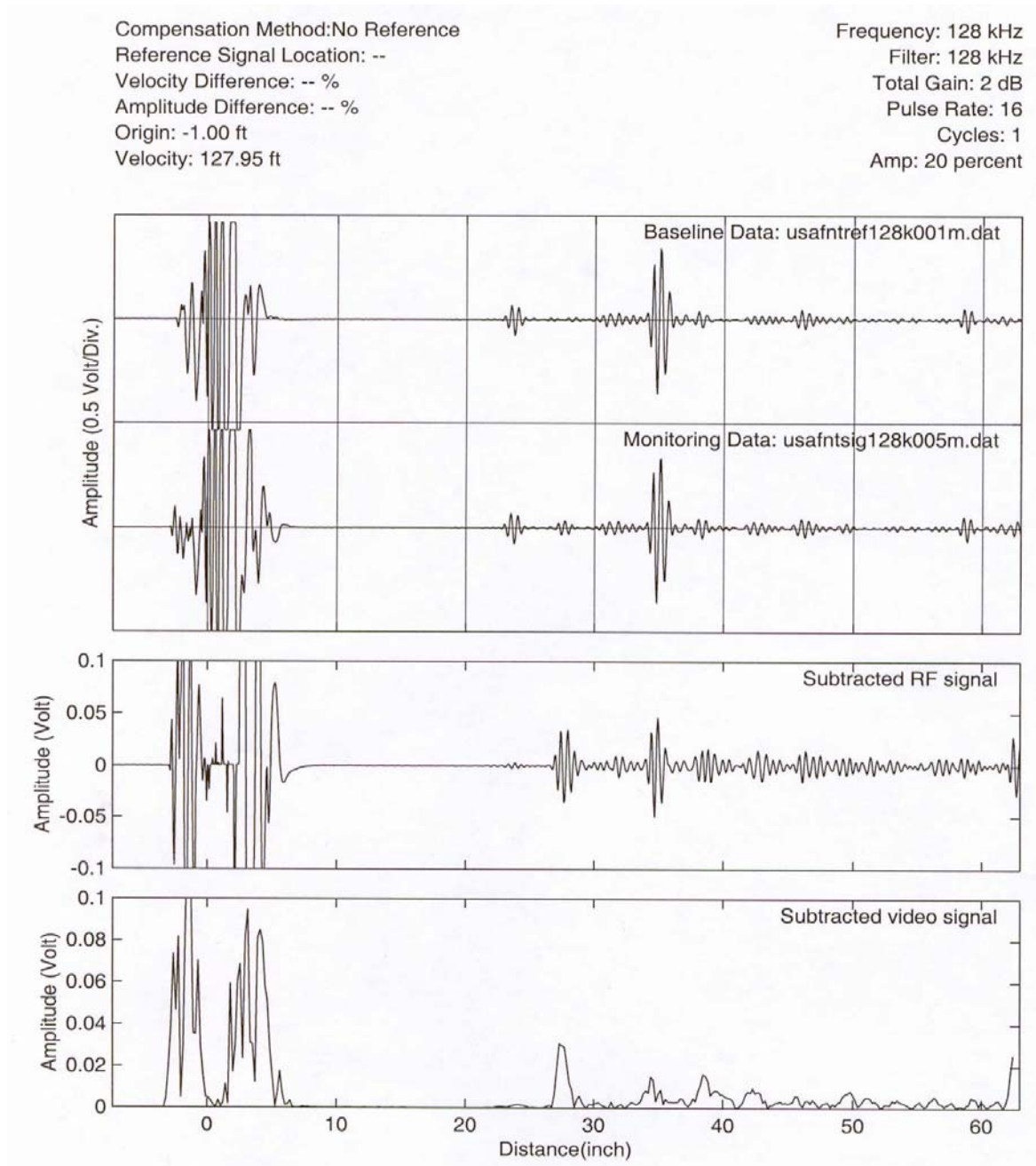


Figure 69. MsS waveform and monitoring data comparing the case of no defect under the adhesively bonded aluminum patch to the case where a 0.9-inch-long, 1/8-inch-deep defect was placed below the adhesively bonded aluminum patch

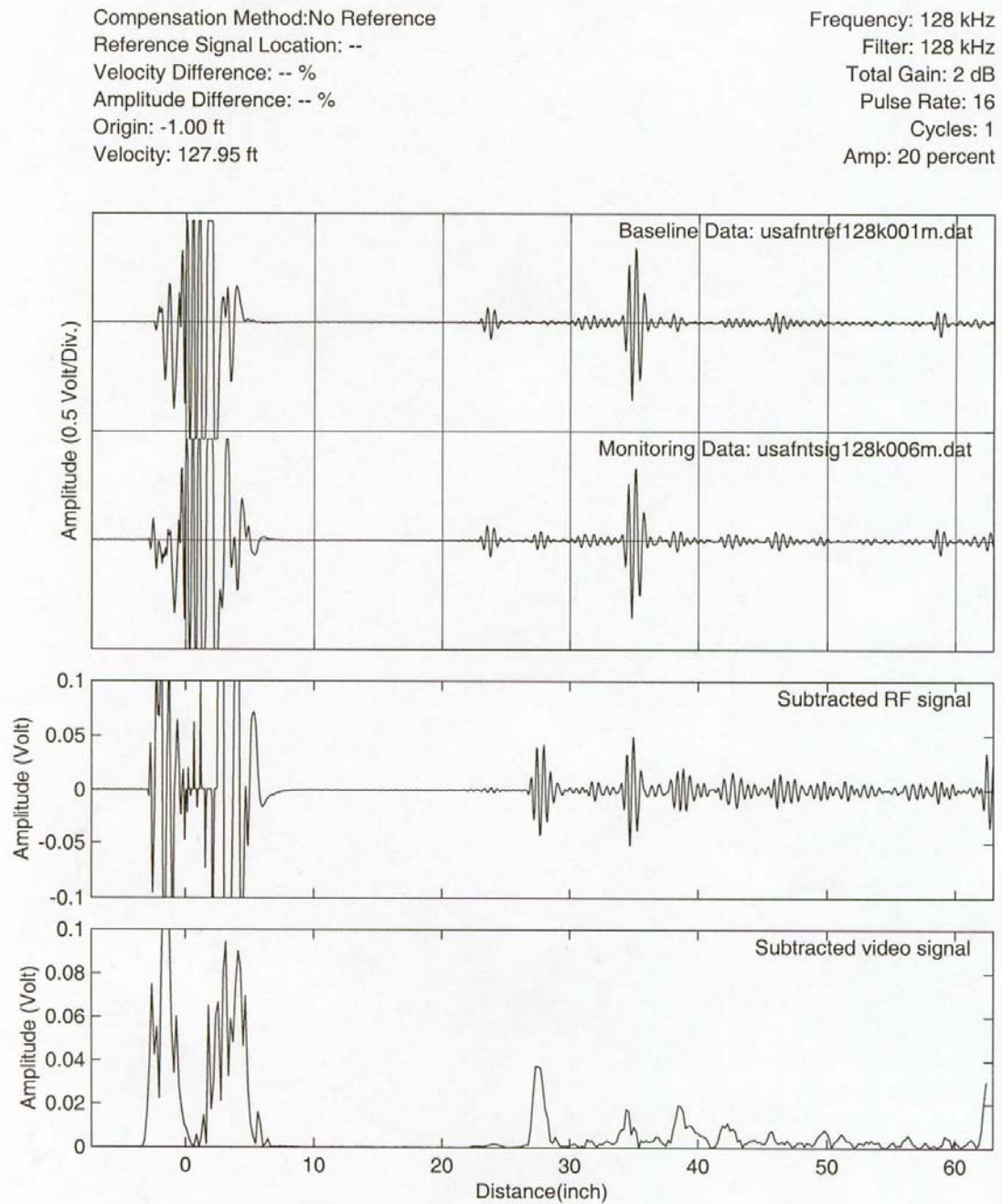


Figure 70. MsS waveform and monitoring data comparing the case of no defect under the adhesively bonded aluminum patch to the case where a 1.0-inch-long, 1/8-inch-deep defect was placed below the adhesively bonded aluminum patch

Compensation Method: No Reference
 Reference Signal Location: --
 Velocity Difference: -- %
 Amplitude Difference: -- %
 Origin: -1.00 ft
 Velocity: 127.95 ft

Frequency: 128 kHz
 Filter: 128 kHz
 Total Gain: 2 dB
 Pulse Rate: 16
 Cycles: 1
 Amp: 20 percent

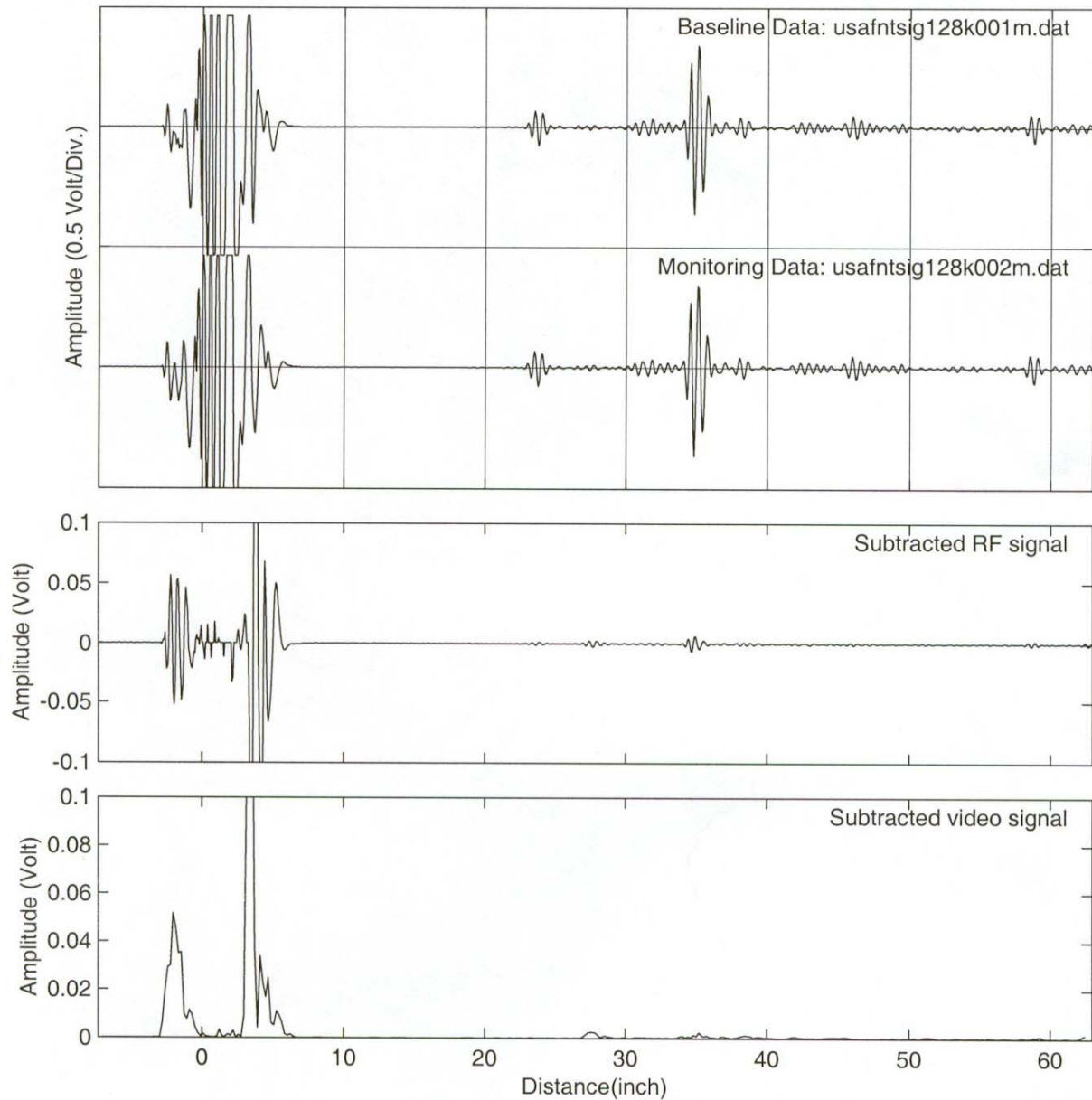


Figure 71. MsS waveform and monitoring data comparing the case where a 0.5-inch-long, 1/8-inch-deep defect was placed below the adhesively bonded aluminum patch to the case where the defect length was increased by 0.1 inch to 0.6 inch

Compensation Method: No Reference
Reference Signal Location: --
Velocity Difference: -- %
Amplitude Difference: -- %
Origin: -1.00 ft
Velocity: 127.95 ft

Frequency: 128 kHz
Filter: 128 kHz
Total Gain: 2 dB
Pulse Rate: 16
Cycles: 1
Amp: 20 percent

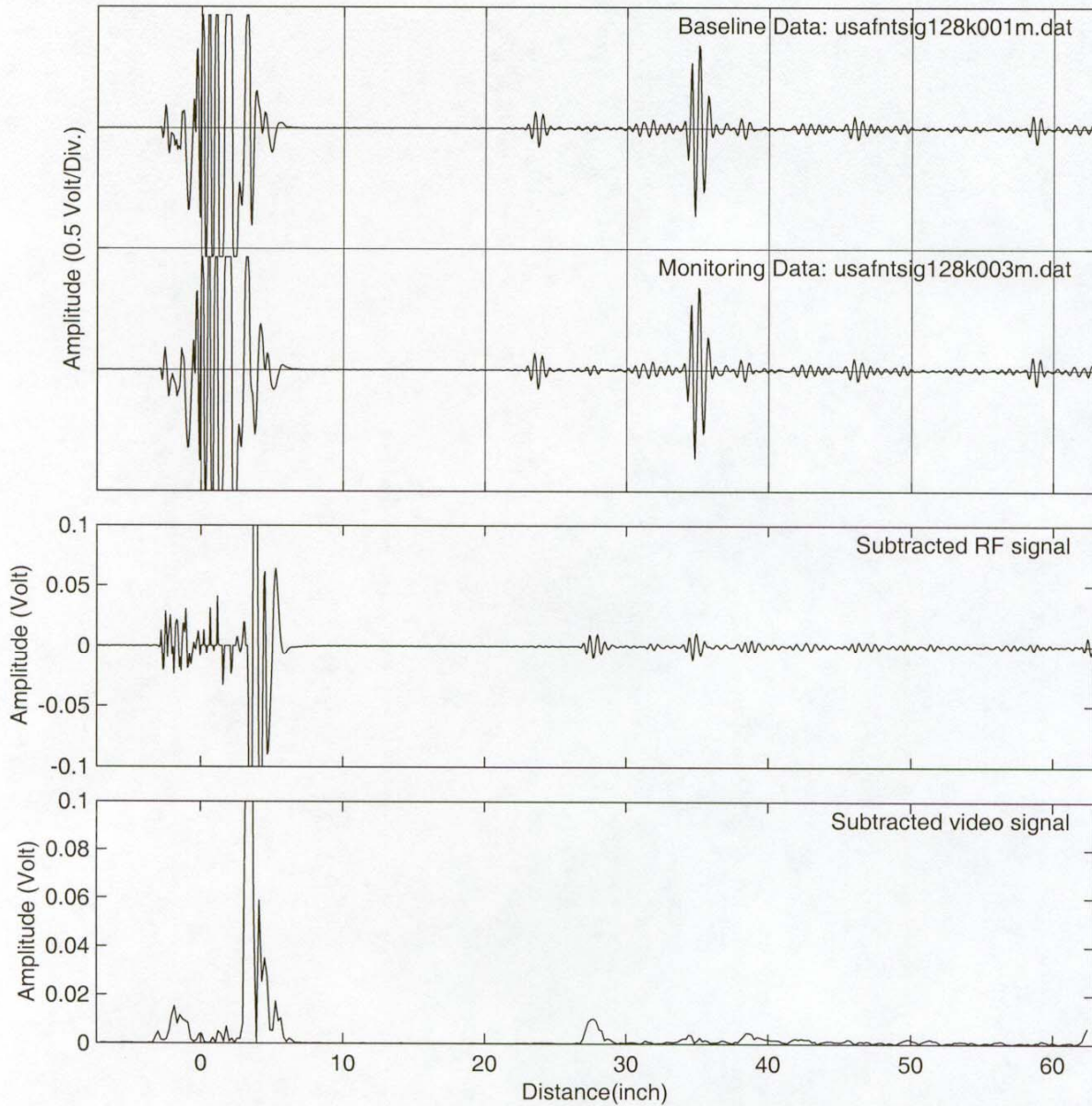


Figure 72. MsS waveform and monitoring data comparing the for the case where a 0.5-inch-long, 1/8-inch-deep defect was placed below the adhesively bonded aluminum patch to the case where the defect length was increased by 0.2 inch to 0.7 inch



Figure 73. Photograph of the test plate showing holes and fasteners

Compensation Method: No Reference
Reference Signal Location: --
Velocity Difference: -- %
Amplitude Difference: -- %
Origin: -1.00 ft
Velocity: 127.95 ft

Frequency: 128 kHz
Filter: 128 kHz
Total Gain: 20 dB
Pulse Rate: 16
Cycles: 1
Amp: 20 percent

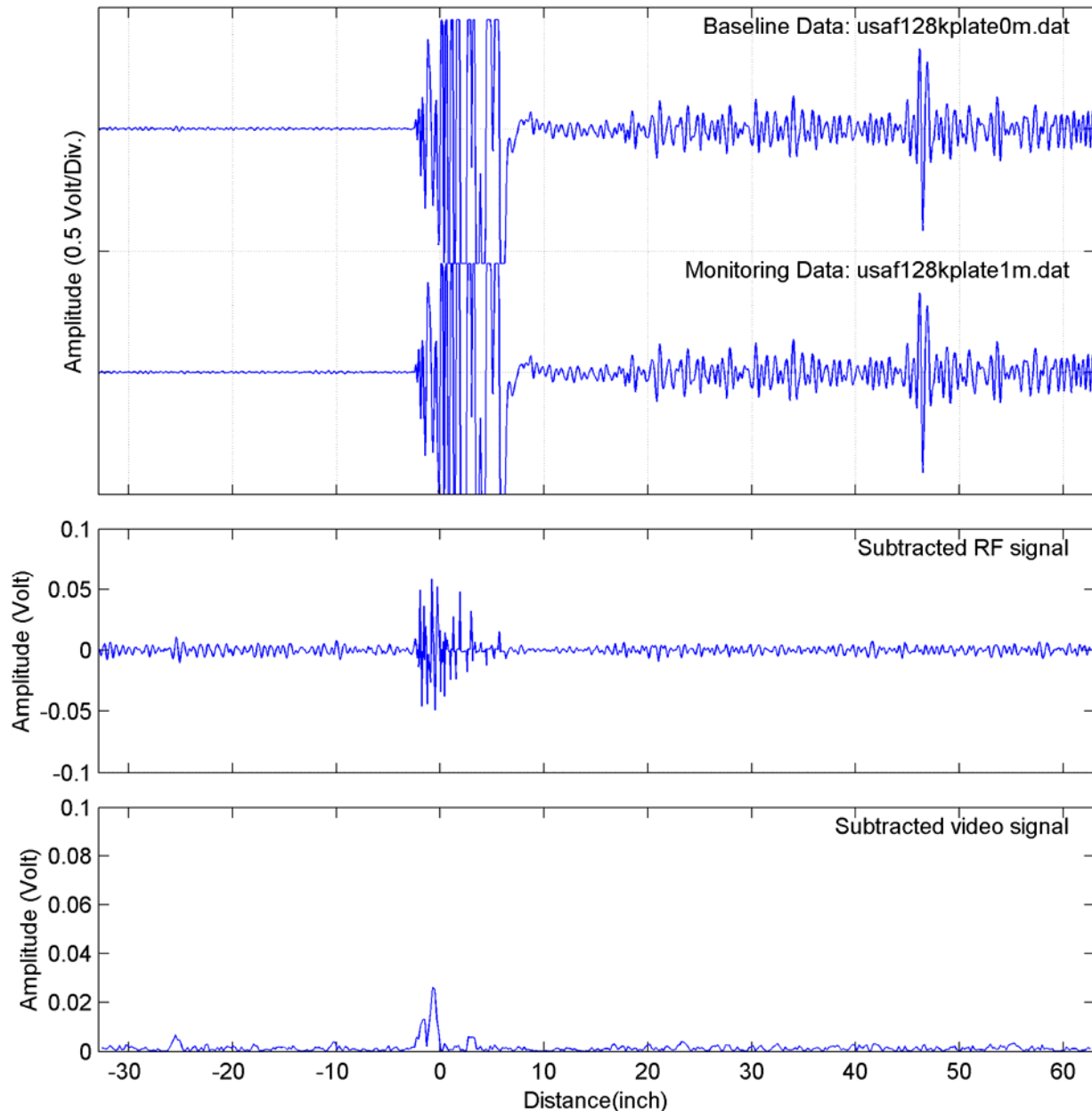


Figure 74. Waveforms obtained for no defects in the holes (top) and another case of no defects in the holes (middle). The lower waveforms show the difference data and it is clear that the difference is basically a flat line except where the sensor output signal was saturated.

Compensation Method: No Reference
Reference Signal Location: --
Velocity Difference: -- %
Amplitude Difference: -- %
Origin: -1.00 ft
Velocity: 127.95 ft

Frequency: 128 kHz
Filter: 128 kHz
Total Gain: 20 dB
Pulse Rate: 16
Cycles: 1
Amp: 20 percent

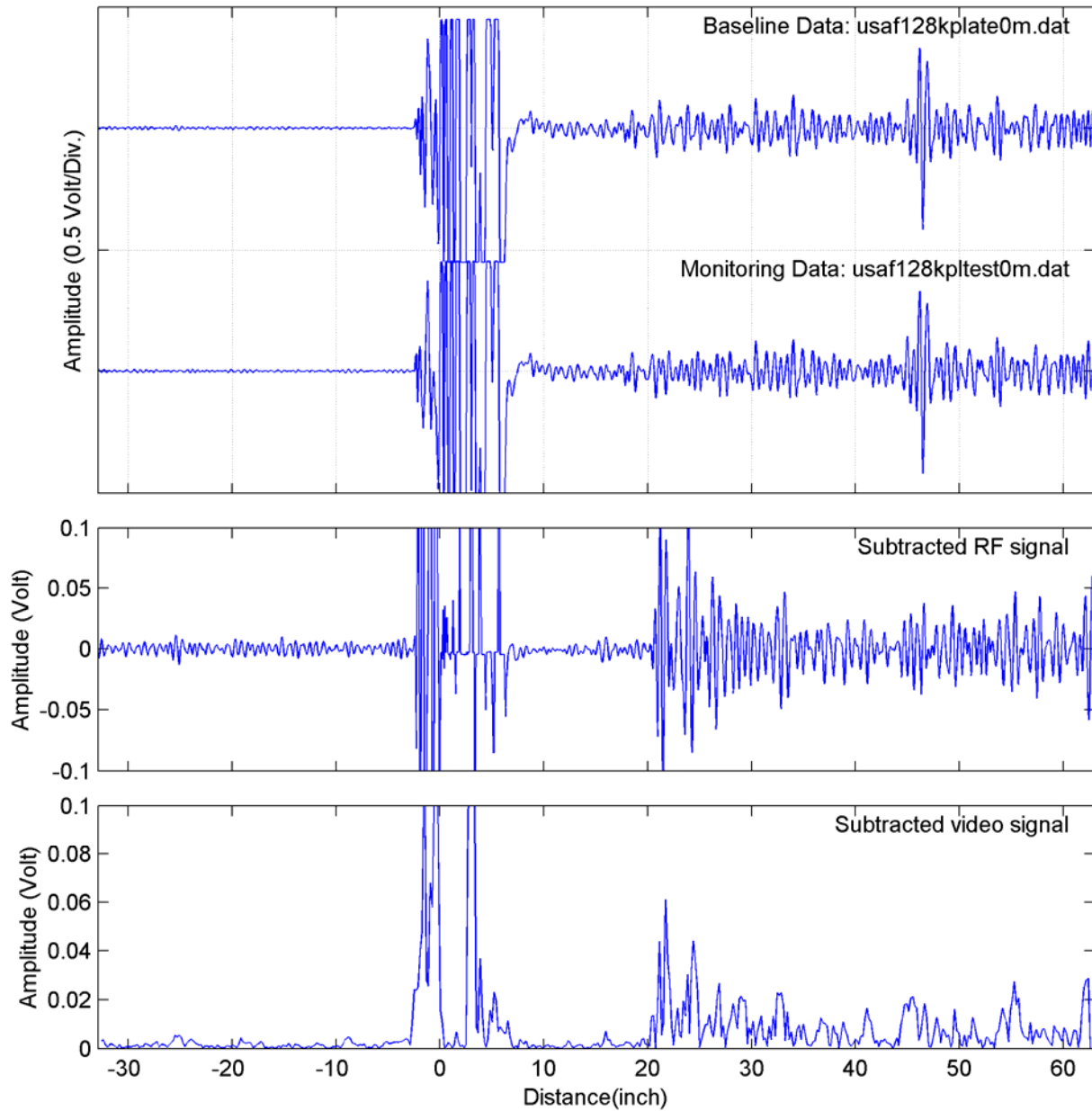


Figure 75. Waveforms obtained for no defects in the holes (top) and with a defect that is approximately 0.003 inch by 0.02 inch diameter inch and in the hole 20 inches from the sensor. The lower waveforms show the difference data and it is clear that the small defect can be seen at 20 inches.

Compensation Method: No Reference
Reference Signal Location: --
Velocity Difference: -- %
Amplitude Difference: -- %
Origin: -1.00 ft
Velocity: 127.95 ft

Frequency: 128 kHz
Filter: 128 kHz
Total Gain: 20 dB
Pulse Rate: 16
Cycles: 1
Amp: 20 percent

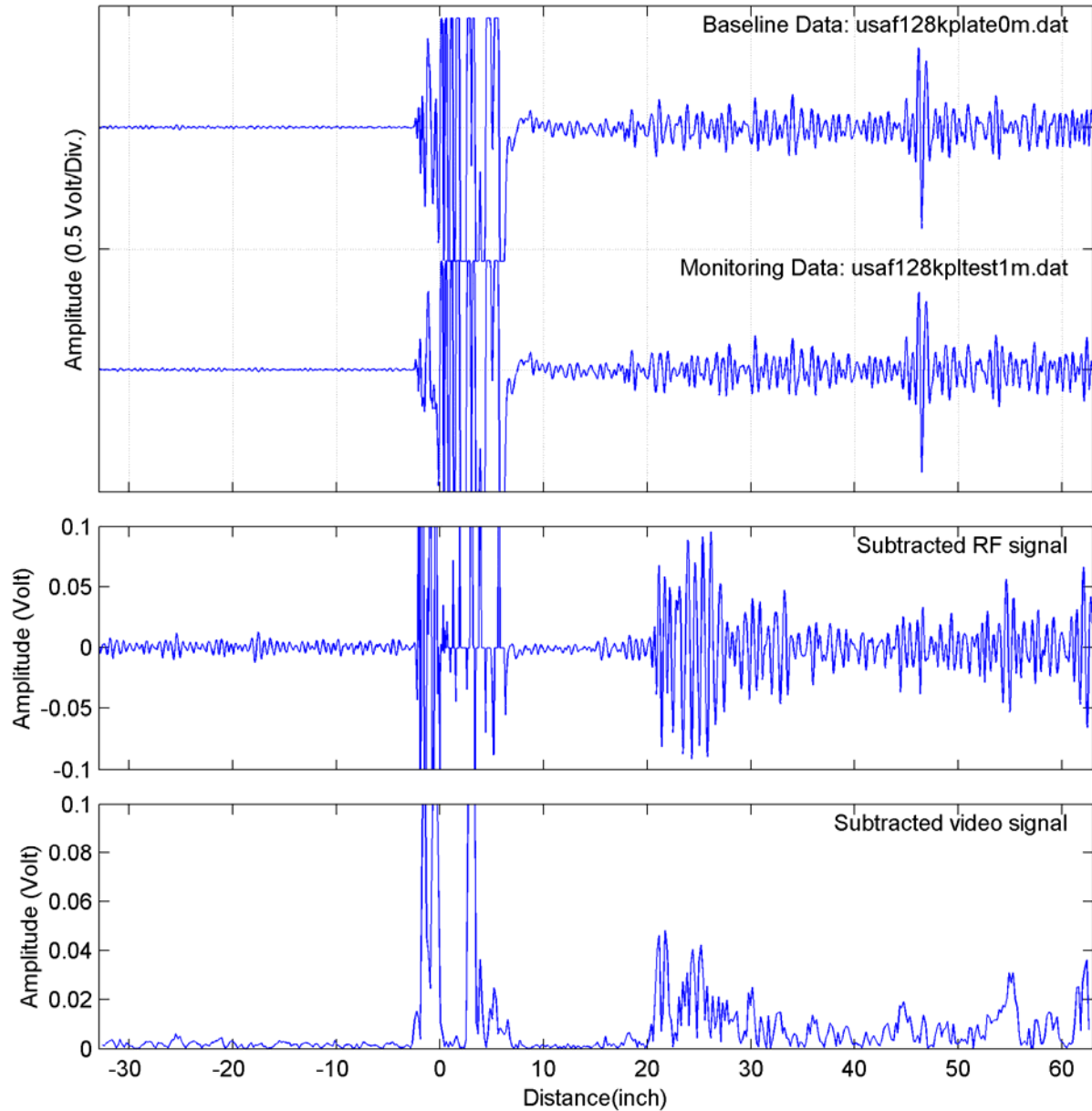


Figure 76 Waveforms obtained for no defects in the holes (top) and with a defect that is approximately 0.01 inch by 0.03 inch diameter and in the hole 20 inches from the sensor. The lower waveforms show the difference data and it is clear that the small defect can be seen at 20 inches.

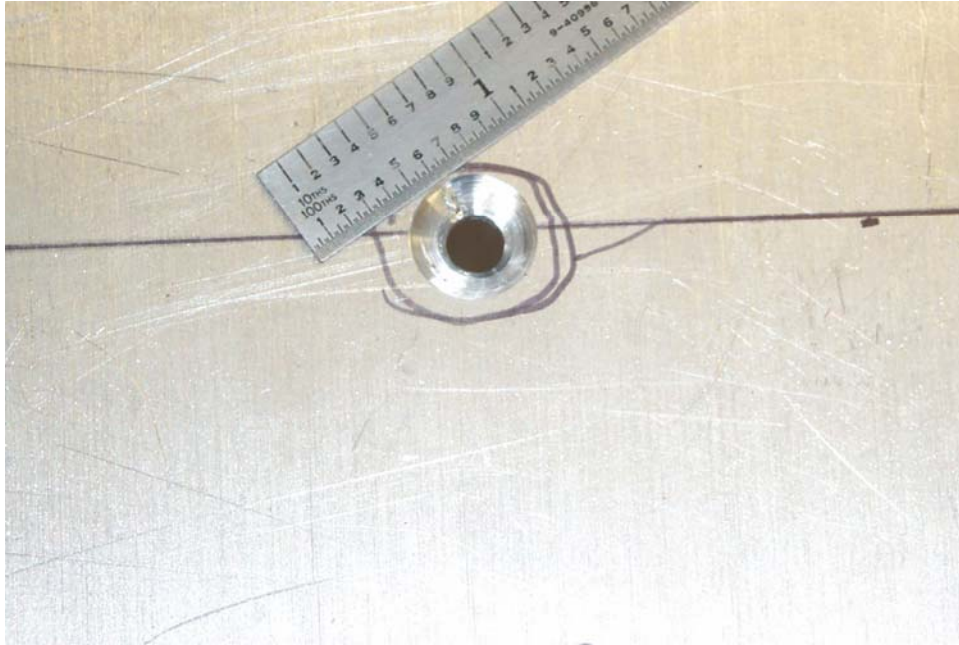


Figure 77. Photograph of the 0.02 inch by 0.05 inch by 0.10 inch defect in the tapered hole



Figure 78. Photograph of the 0.006 inch by 0.05 inch by 0.1 inch defect in the tapered hole

Compensation Method: No Reference
Reference Signal Location: --
Velocity Difference: -- %
Amplitude Difference: -- %
Origin: -1.00 ft
Velocity: 127.95 ft

Frequency: 128 kHz
Filter: 128 kHz
Total Gain: 20 dB
Pulse Rate: 16
Cycles: 1
Amp: 20 percent

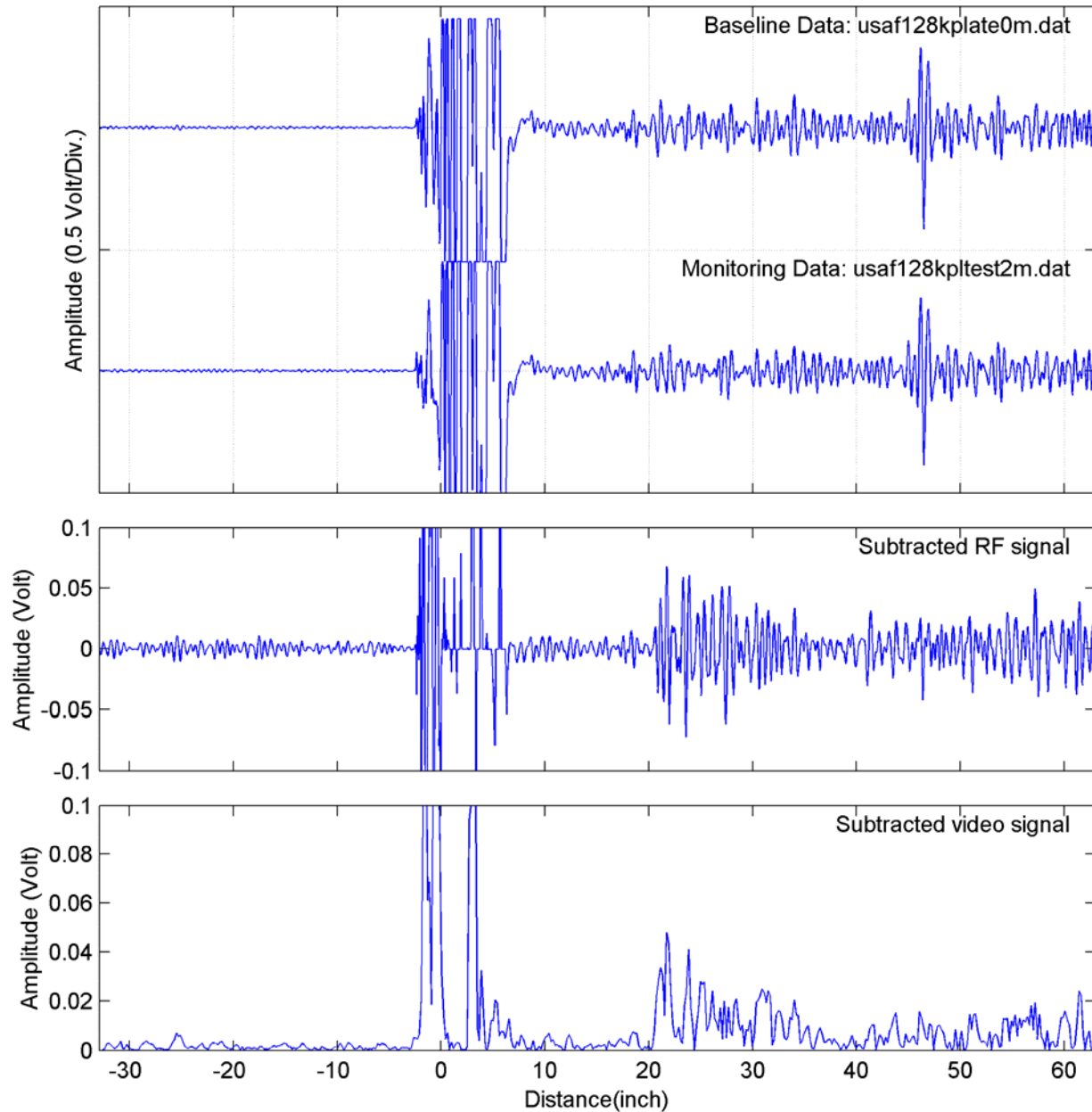


Figure 79. Waveforms obtained for no defects in the holes (top) and with a defect that is approximately 0.02 inch by 0.05 inch by 0.1 inch and in the hole 20 inches from the sensor. The lower waveforms show the difference data and it is clear that the small defect can be seen at 20 inches.

Compensation Method: No Reference
Reference Signal Location: --
Velocity Difference: -- %
Amplitude Difference: -- %
Origin: -1.00 ft
Velocity: 127.95 ft

Frequency: 128 kHz
Filter: 128 kHz
Total Gain: 20 dB
Pulse Rate: 16
Cycles: 1
Amp: 20 percent

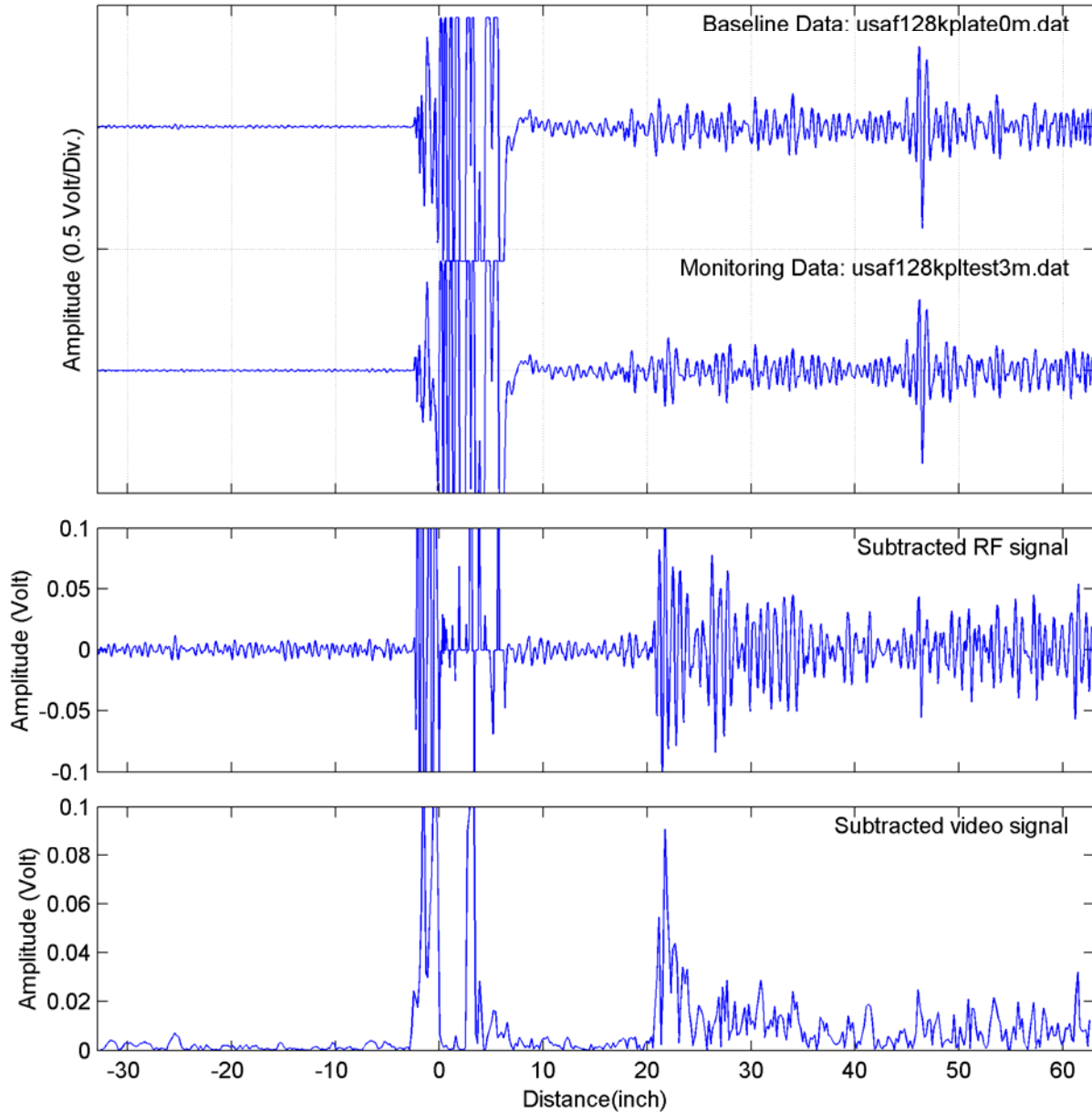


Figure 80. Waveforms obtained for no defects in the holes (top) and with a defect that is approximately 0.025 inch by 0.08 inch in diameter and in the hole 20 inches from the sensor. The lower waveforms show the difference data and it is clear that the small defect can be seen at 20 inches.

Compensation Method: No Reference
Reference Signal Location: --
Velocity Difference: -- %
Amplitude Difference: -- %
Origin: -1.00 ft
Velocity: 127.95 ft

Frequency: 128 kHz
Filter: 128 kHz
Total Gain: 20 dB
Pulse Rate: 16
Cycles: 1
Amp: 20 percent

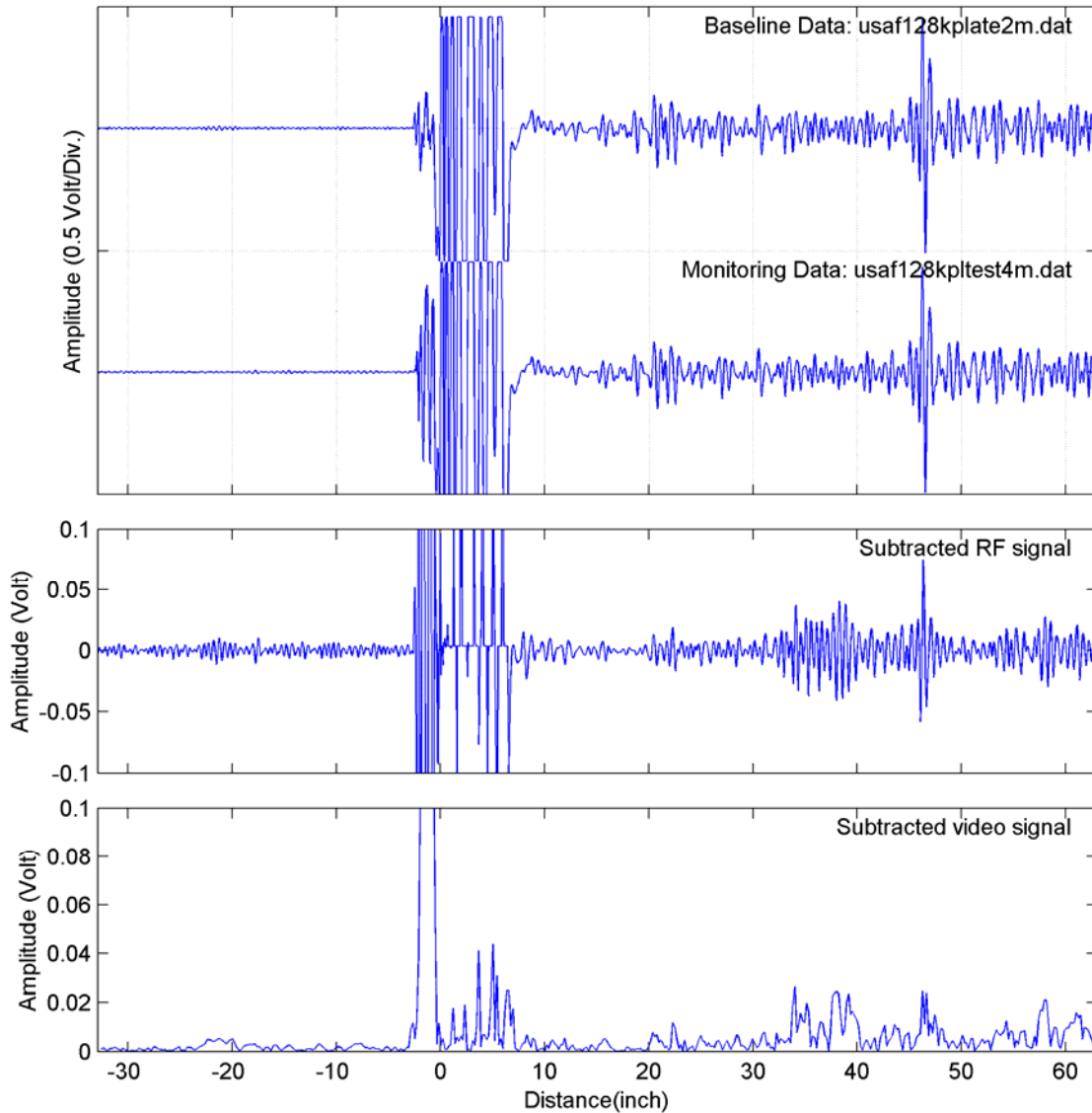


Figure 81. The top waveform (reference) was from the case where the large defect was in the hole 20 inches from the MsS. The middle (monitoring) waveform is from the case where the 0.003 inch by 0.01 inch by 0.01 inch defect was introduced into the fastener hole approximately 32 inches from the MsS. Again, it is impossible to visually detect any difference between the monitoring data and baseline data. However, when the difference is obtained, the defect clearly is detected at approximately 32 inches from the MsS.

Compensation Method: No Reference
Reference Signal Location: --
Velocity Difference: -- %
Amplitude Difference: -- %
Origin: -1.00 ft
Velocity: 127.95 ft

Frequency: 128 kHz
Filter: 128 kHz
Total Gain: 20 dB
Pulse Rate: 16
Cycles: 1
Amp: 20 percent

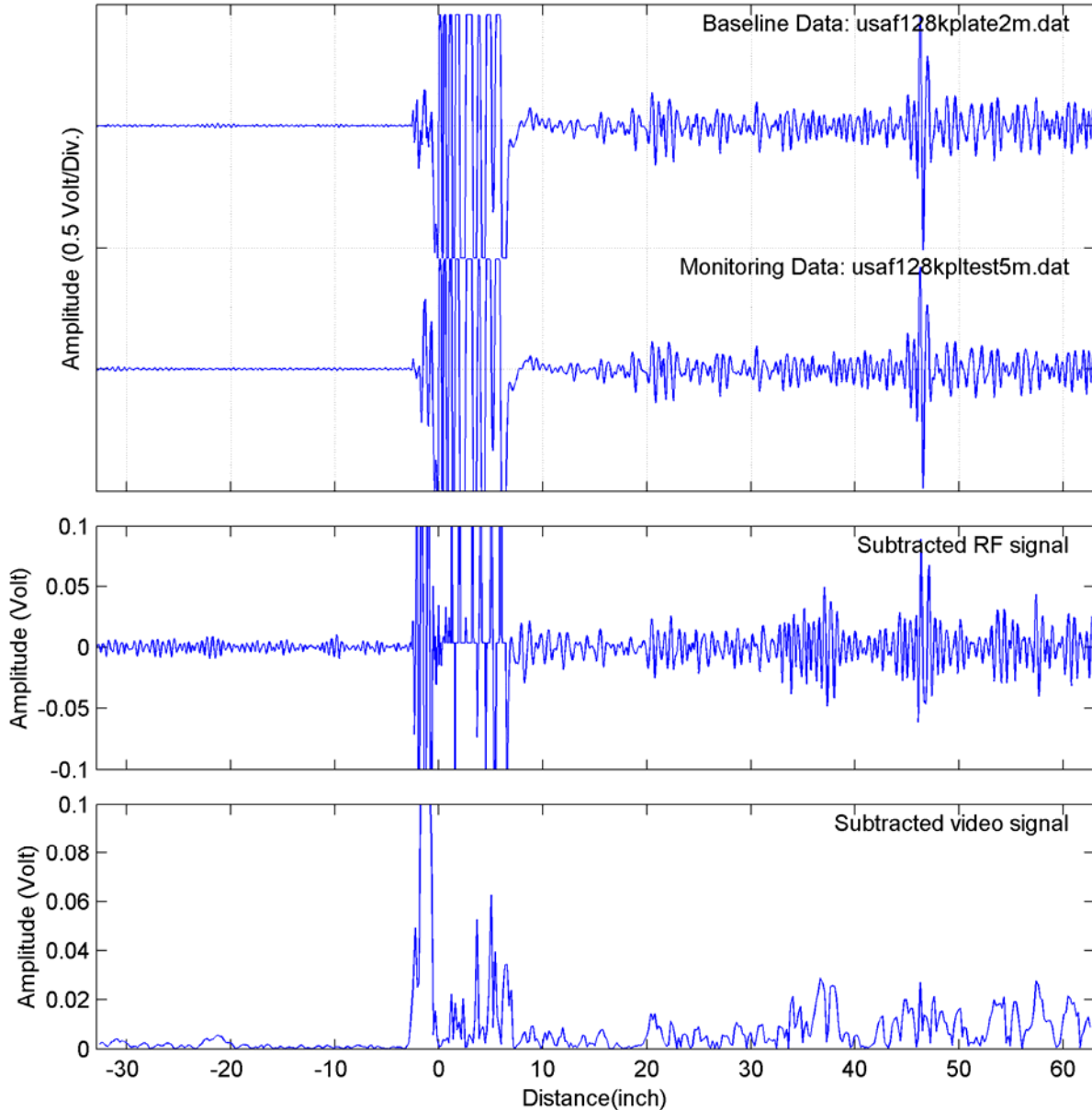


Figure 82. The top waveform (reference) was from the case where the large defect was in the hole 20 inches from the MsS. The middle (monitoring) waveform is from the case where the 0.006 inch by 0.03 inch by 0.03 inch defect was introduced into the fastener hole approximately 32 inches from the MsS. Again, it is impossible to visually detect any difference between the monitoring data and baseline data. However, when the difference is obtained, the defect clearly is detected at approximately 32 inches from the MsS.

Compensation Method: No Reference
Reference Signal Location: --
Velocity Difference: -- %
Amplitude Difference: -- %
Origin: -1.00 ft
Velocity: 127.95 ft

Frequency: 128 kHz
Filter: 128 kHz
Total Gain: 20 dB
Pulse Rate: 16
Cycles: 1
Amp: 20 percent

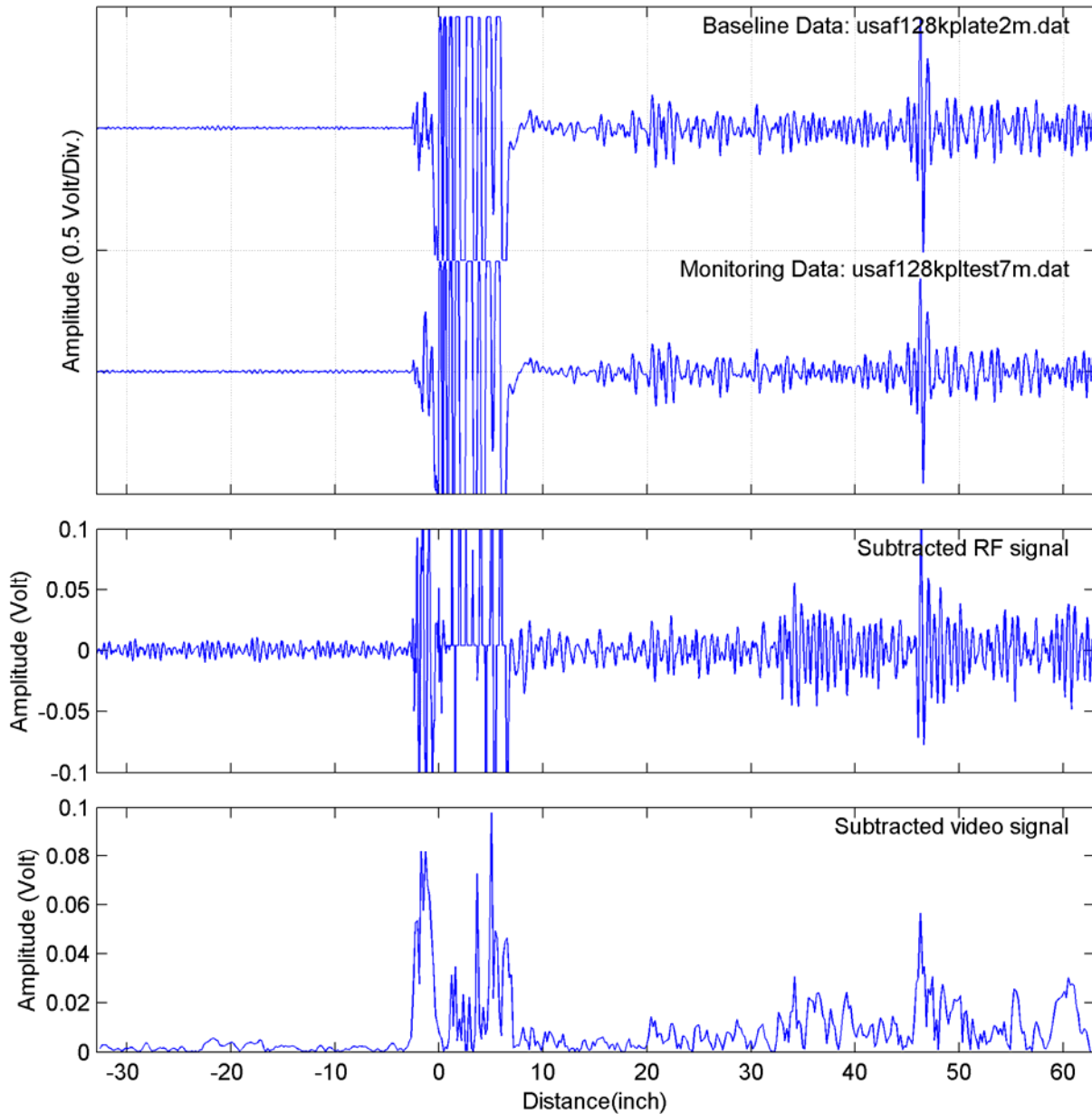


Figure 83. The top waveform (reference) was from the case where the large defect was in the hole 20 inches from the MsS. The middle (monitoring) waveform is from the case where the 0.006 inch by 0.05 inch by 0.05 inch defect was introduced into the fastener hole approximately 32 inches from the MsS. Again, it is impossible to visually detect any difference between the monitoring data and baseline data. However, when the difference is obtained, the defect clearly is detected at approximately 32 inches from the MsS.

A third test was done with more care taken in measuring the defects in the hole located approximately 23 inches from the MsS. The holes were measured to be approximately 0.01 inch deep by 0.03 inch diameter, 0.02 inch deep by 0.05 inch diameter, and 0.025 inch by 0.065 inch in diameter. The MsS inspection and monitoring data obtained for each of these cases is shown in Figures 84 through 86. Again, it is impossible to see any difference in the inspection waveforms, but the difference waveform clearly shows the presence of the defects.

2.4.5 *Cryogenic Fuel Lines for NASA*

Remote monitoring using an ultrasonic guided wave examination was suggested as an approach for assessing the physical condition of vent line piping at a NASA launch facility. Magnetostrictive sensor (MsS) technology was determined to be a potential method of inducing and receiving guided waves. This approach involves permanently bonding a high-purity nickel strip circumferentially around the pipe at a single location (as shown in Figures 87 and 88), applying a bias magnetic field to the strip, applying an alternating magnetic field using electromagnetic coils, to send and receive, respectively, mechanical energy in the pipe in the form of guided waves. However, there are two potential difficulties associated with using this technology on the NASA vent line pipe. First, the pipe is made from aluminum and SwRI has experienced difficulties with using the nickel strip probe on an aluminum substrate and subjecting the combination to large temperature extremes. Second, the temperature of the aluminum pipe is not circumferentially symmetric during use; that is, the bottom of the pipe reaches a temperature of approximately -200°F while the top of the pipe is close to ambient temperature. It has been observed in past work that subjecting a nickel-based MsS transducer bonded on aluminum to extreme temperatures ranges had caused the nickel to lose its ability to be magnetized.

Two experiments were conducted on the aluminum pipe to validate that the MsS can be subjected to asymmetric thermal changes in the cryogenic range to show (1) no change in the waveform if no change in the status of the pipe has occurred and (2) a change in the waveform if a defect has been initiated in the pipe. The first experiment involved investigation of the guided wave data taken from each sensor location before and after exposure to extreme cold on the underside of the pipe. Baseline data were taken with each MsS prior to exposure to the nitrogen bath. After the baseline MsS data were collected, the underside of the pipe end in the area where the MsS was located was placed in a customized Styrofoam ice chest and sealed to the bottom of the pipe. Liquid nitrogen was then placed in the ice chest so that the liquid level approximately covered the lower quarter of the pipe circumference. The liquid nitrogen temperature was approximately -321°F (-196°C). This process simulated the operational conditions experienced by the Shuttle fuel lines during filling of the tanks. MsS data waveforms were collected continuously during this time to monitor the effects of the temperature excursion. The liquid nitrogen in the basin was replenished to maintain constant depth for approximately 15 minutes. The pipe was then allowed to return to room temperature when MsS data monitoring waveforms were again recorded.

Compensation Method: No Reference
Reference Signal Location: --
Velocity Difference: -- %
Amplitude Difference: -- %
Origin: -1.00 ft
Velocity: 127.95 ft

Frequency: 128 kHz
Filter: 128 kHz
Total Gain: 20 dB
Pulse Rate: 16
Cycles: 1
Amp: 20 percent

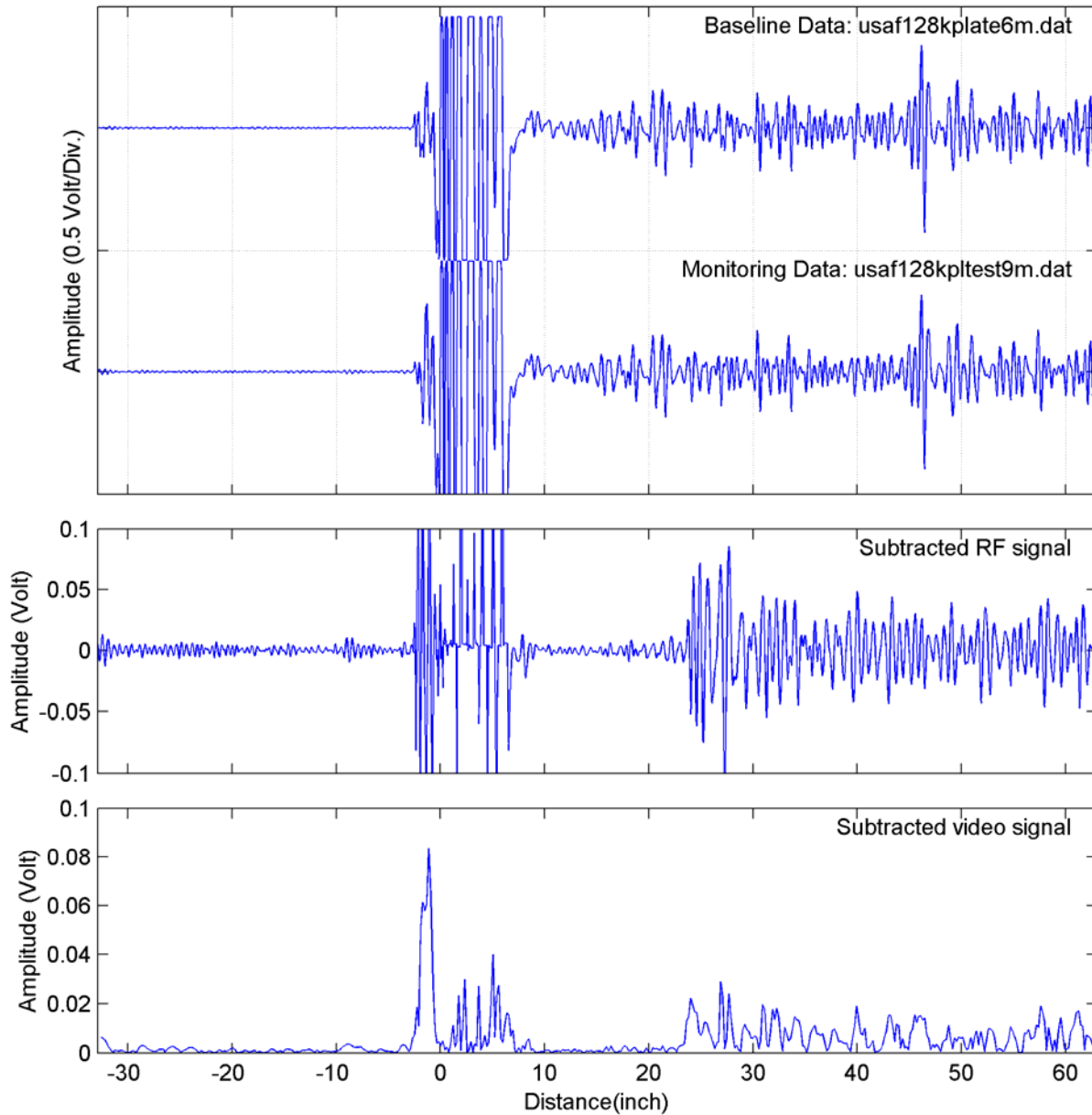


Figure 84. The top waveform (reference) was from the case where the defect was in the hole 23 inches from the MsS. The middle (monitoring) waveform is from the case where a defect approximately 0.01 inch deep by 0.03 inch diameter was introduced into the fastener hole approximately 23 inches from the MsS. Again, it is impossible to visually detect any difference between the monitoring data and baseline data. However, when the difference is obtained, the defect clearly is detected at approximately 23 inches from the MsS.

Compensation Method: No Reference
Reference Signal Location: --
Velocity Difference: -- %
Amplitude Difference: -- %
Origin: -1.00 ft
Velocity: 127.95 ft

Frequency: 128 kHz
Filter: 128 kHz
Total Gain: 20 dB
Pulse Rate: 16
Cycles: 1
Amp: 20 percent

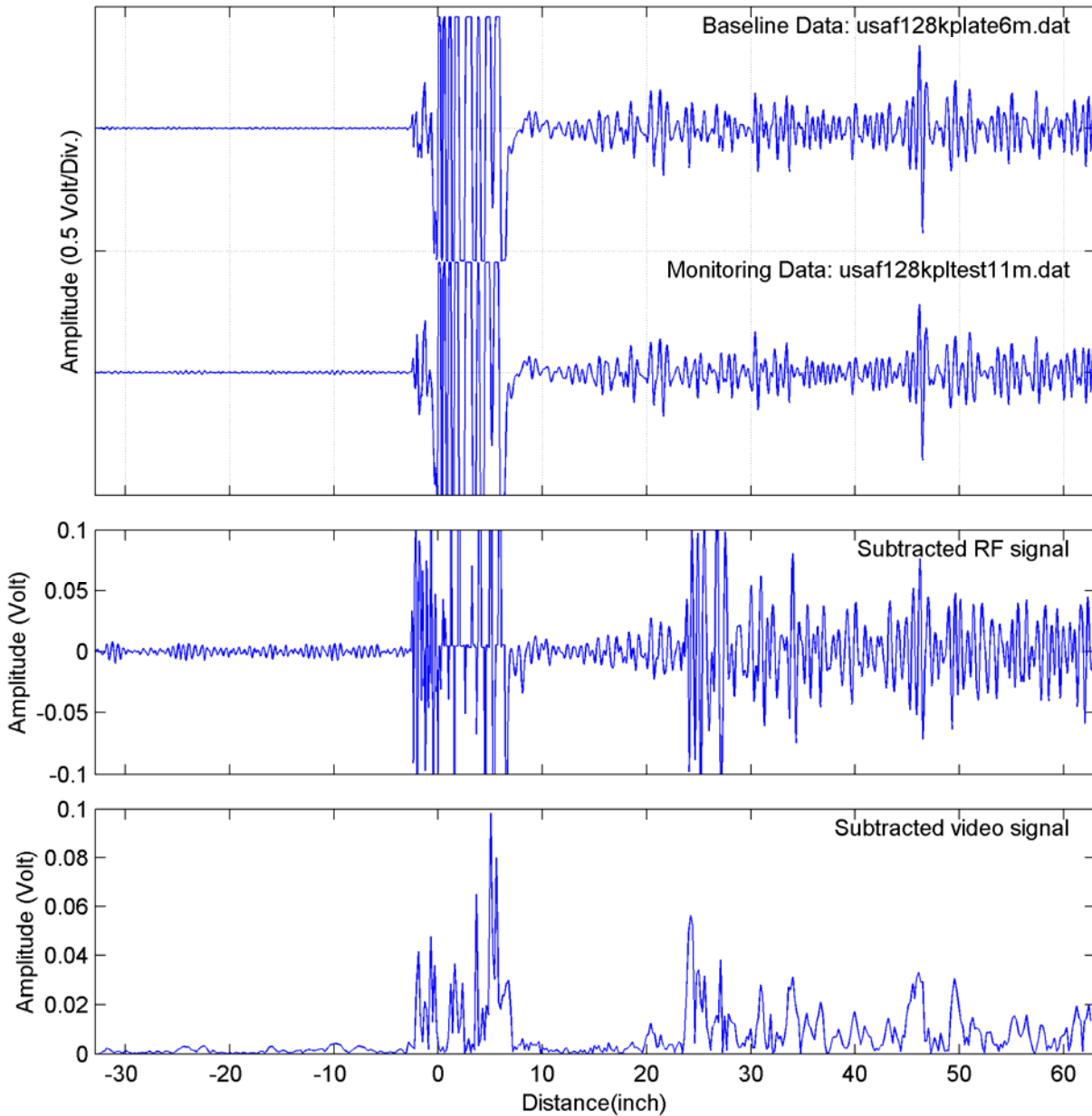


Figure 85. The top waveform (reference) was from the case where the defect was in the hole 23 inches from the MsS. The middle (monitoring) waveform is from the case where a defect size was increased to approximately 0.02 inch deep by 0.05 inch diameter. Again, it is impossible to visually detect any difference between the monitoring data and baseline data. However, when the difference is obtained, the defect clearly is detected at approximately 23 inches from the MsS.

Compensation Method: No Reference
Reference Signal Location: --
Velocity Difference: -- %
Amplitude Difference: -- %
Origin: -1.00 ft
Velocity: 127.95 ft

Frequency: 128 kHz
Filter: 128 kHz
Total Gain: 20 dB
Pulse Rate: 16
Cycles: 1
Amp: 20 percent

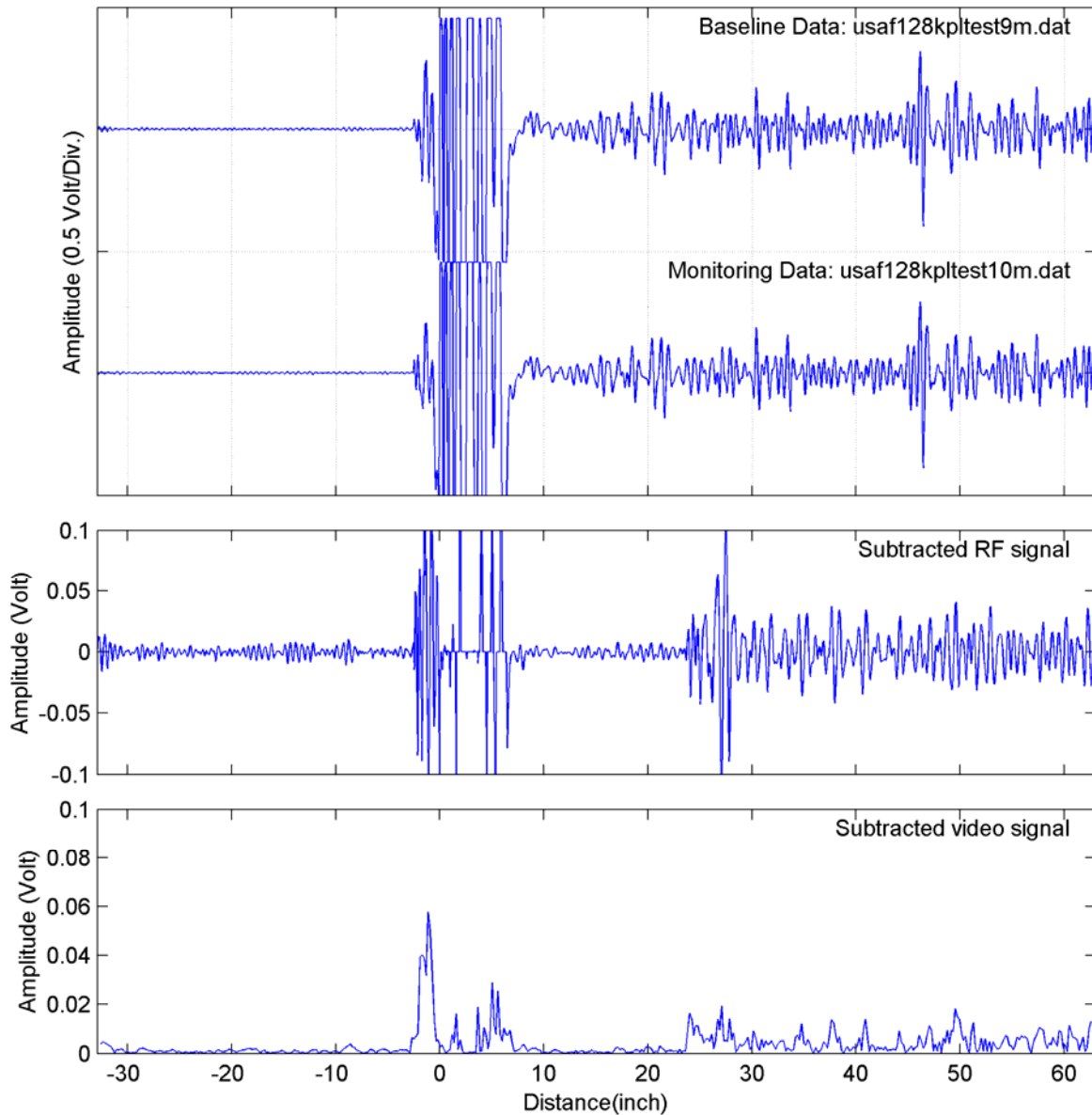


Figure 86. The top waveform (reference) was from the case where the defect was in the hole 23 inches from the MsS. The middle (monitoring) waveform is from the case where a defect size was increased to approximately 0.025 inch by 0.065 inch in diameter. Again, it is impossible to visually detect any difference between the monitoring data and baseline data. However, when the difference is obtained, the defect clearly is detected at approximately 23 inches from the MsS.



Figure 87. Photograph of the ample pipe used in study. Monitoring MsSs were bonded on each end of the pipe

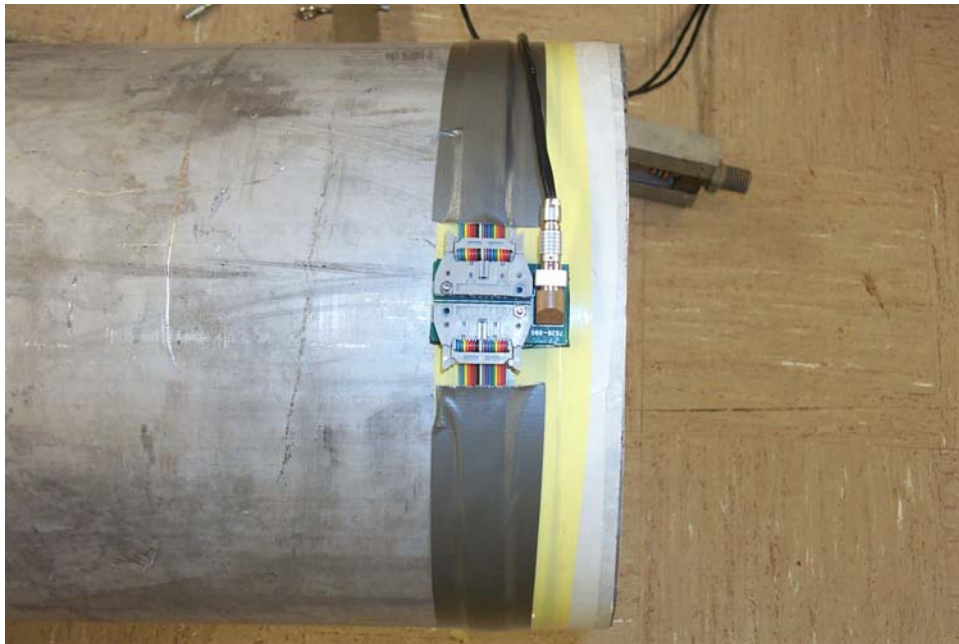


Figure 88. Photograph illustrating the placement of the transducers on the sample pipe

To study the effects of the cold on the underside of the sensor, MsS data waveforms collected after the pipe had returned to ambient temperature were compared to the baseline MsS data waveform collected prior to subjecting the pipe to the liquid nitrogen bath using the SwRI waveform subtraction algorithm. Waveform subtraction involves the normalization (in both amplitude and time) of the monitoring data waveform to a known, non-changing signal in the waveform, such as a pipe end reflection, in the baseline waveform data. Once the monitoring waveform data has been normalized, the baseline waveform is subtracted to reveal any new or higher magnitude features in the monitoring waveform data. Comparisons of the aluminum pipe baseline data with the monitoring waveform data taken after the pipe returned to room temperature are shown in Figure 89 for the continuous band and Figure 90 for the segmented band.

The waveforms shown in the top of each figure are actual waveforms. The normalization occurs prior to waveform subtraction. The waveforms in Figure 89 are very similar in both amplitude and time. The waveforms in Figure 90 are not, and this shows the importance of waveform normalization. Each figure shows waveforms containing the initial pulse and the reflection of that pulse from the far end of the pipe. In both figures, examination of the subtraction results show that the temperature excursion does not introduce extraneous features in the data, thus there is a near perfect cancellation of the end reflection for each case. However, there is a marked decrease in the amplitude of the end reflection in the case of the segmented band after chilling. It is not clear why this occurs in the segmented band and not the continuous band, but the gain and time shift associated with the waveform subtraction method is able to compensate for this drop in amplitude.

The results of this experiment show that the standard method of applying a continuous nickel band with fast curing epoxy is sufficient to endure temperature excursions similar to those expected in the field, even without remagnetizing the nickel strip.

To investigate the effectiveness of this monitoring technique for detecting flaws over time, a narrow saw cut notch approximately 0.19 inches (4.8 mm) deep was placed in the pipe approximately 46 inches (1.17 m) from the continuous nickel MsS. Data were taken again from each MsS and the subtraction method algorithm was used to determine if the notch was detectable in a monitoring application. Figures 91 and 92 show the monitoring data for the continuous band and segmented band transducers, respectively.

These data showed that the notch (which is approximately 3.2 inches long, 0.19 inch deep at its maximum and approximately 2% of the total wall cross section), is detectable using waveform subtraction with either the continuous band or the segmented band transducers. However, the continuous nickel MsS performed much better.

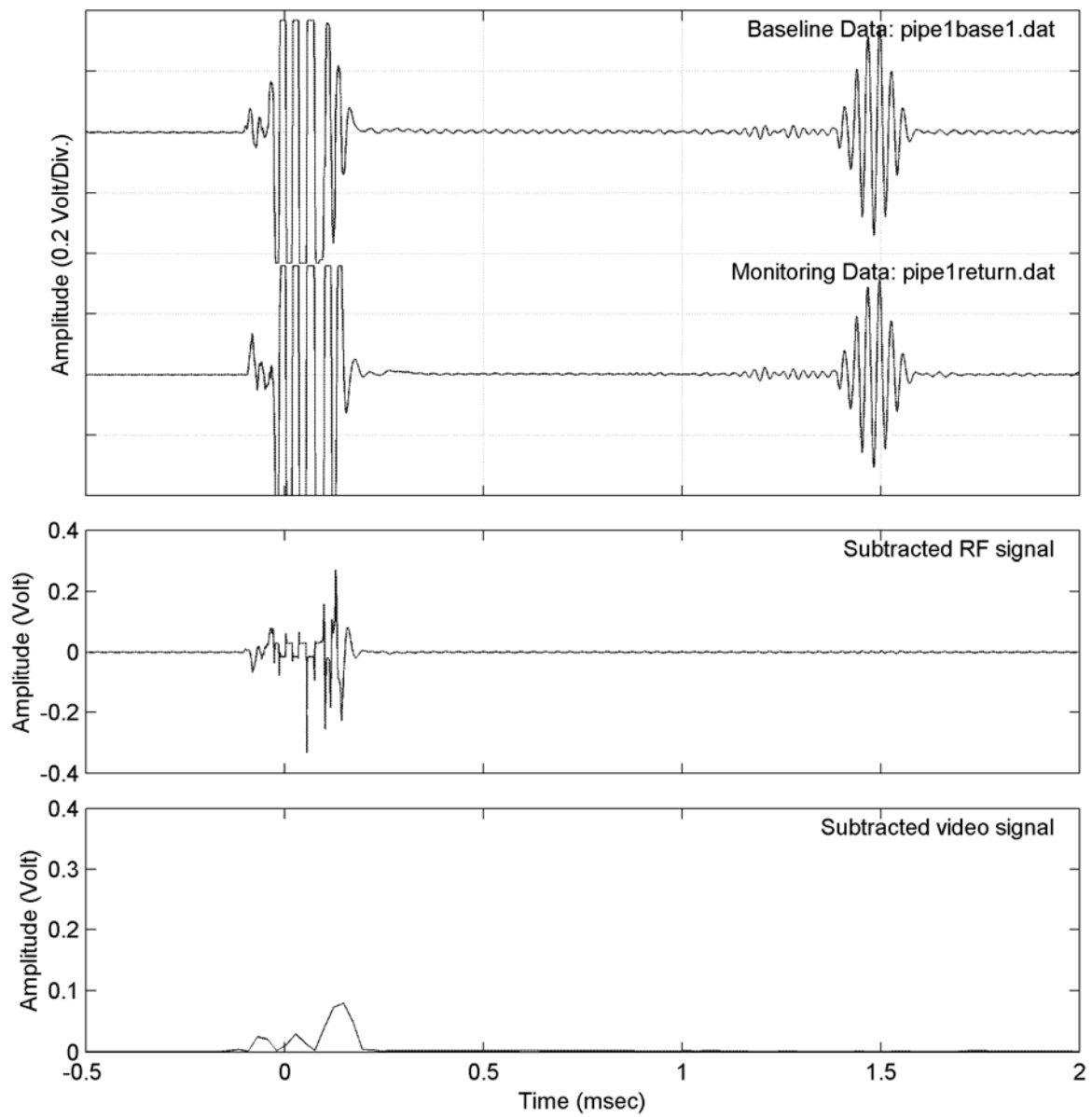


Figure 89. Comparison of normalized baseline waveform data with normalized monitoring waveform data taken after temperature excursion for the continuous MsS

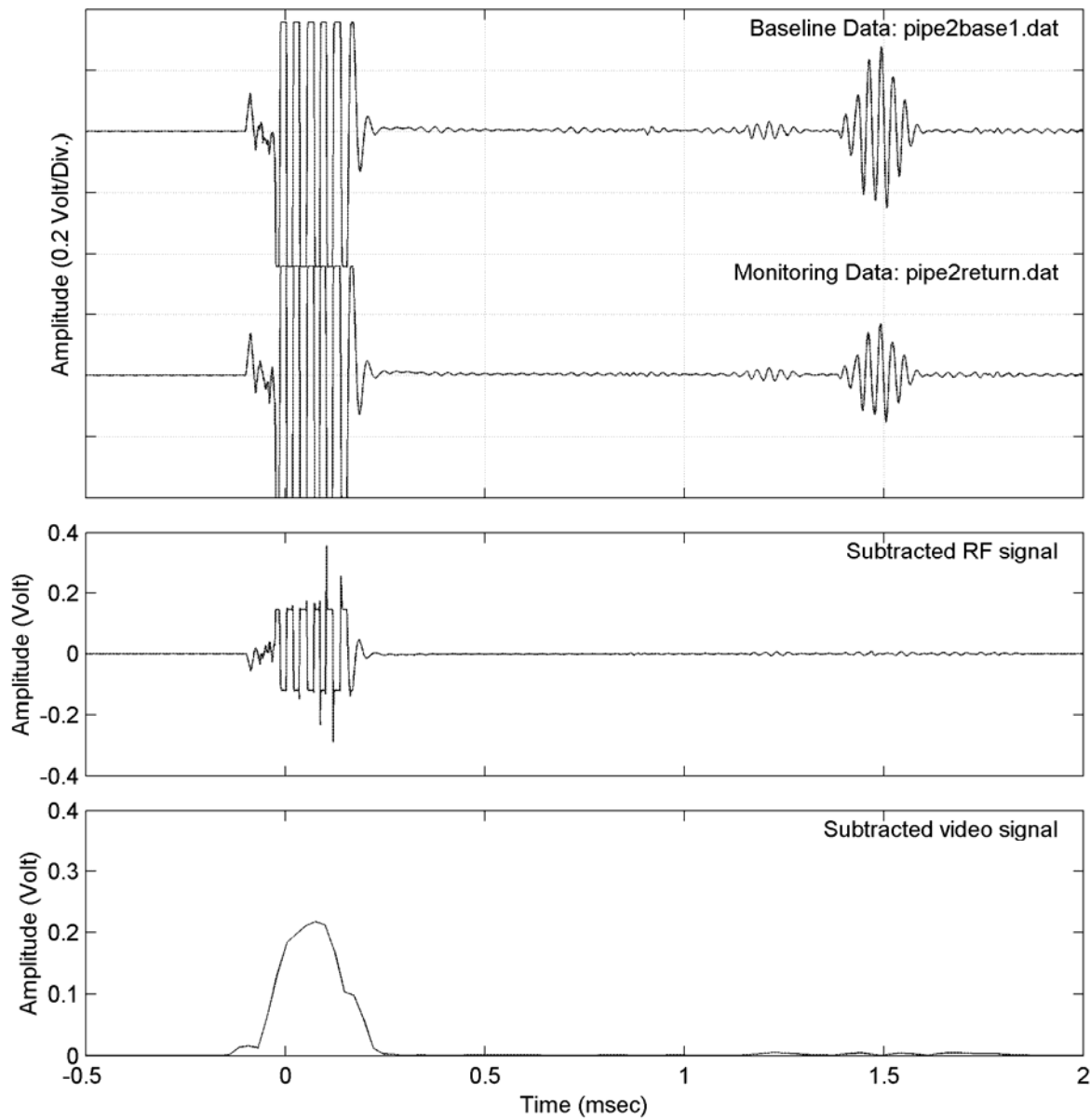


Figure 90. Comparison of baseline waveform data with monitoring waveform data taken after temperature excursion for the segmented MsS

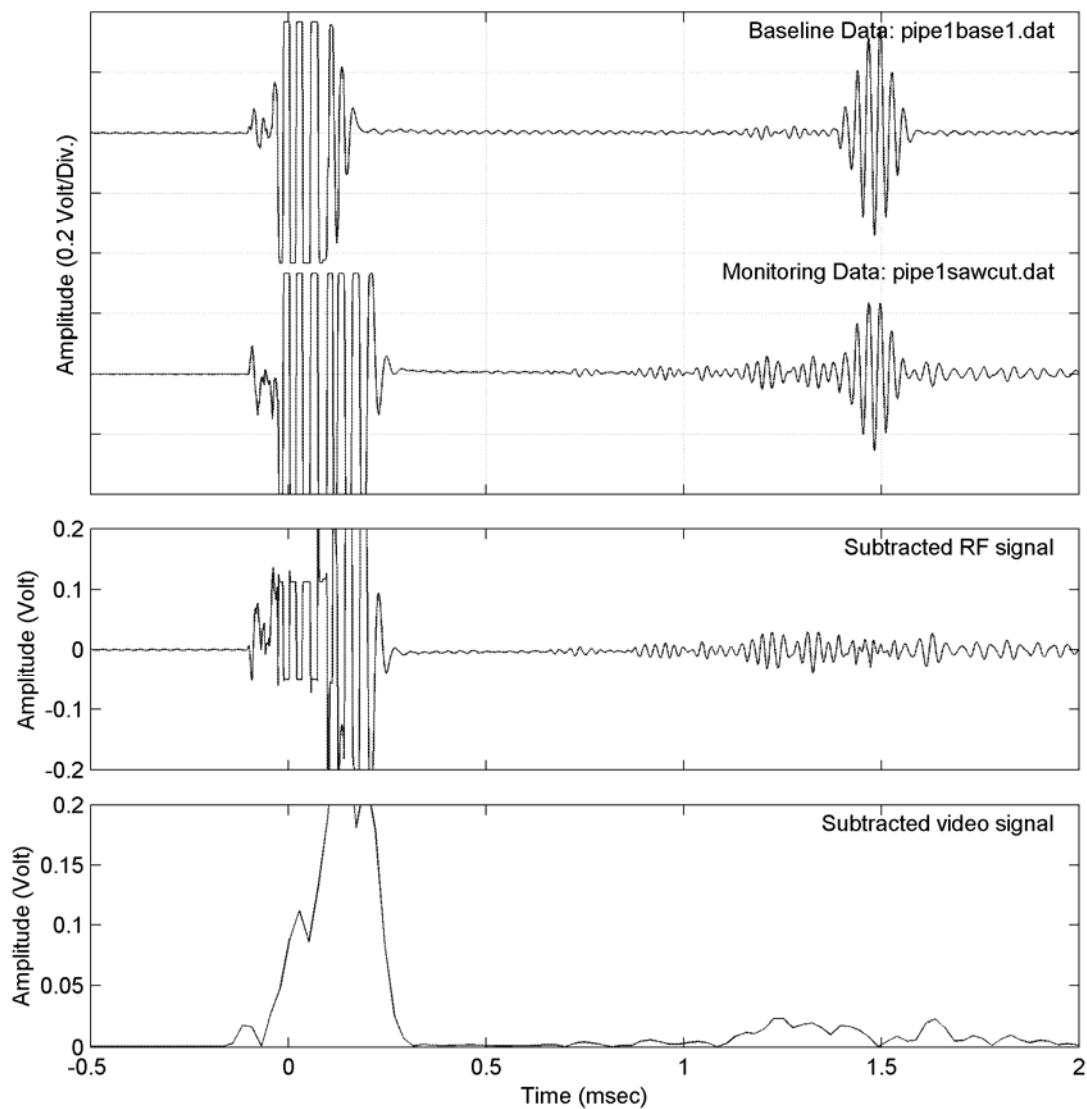


Figure 91. Waveform data collected with the continuous band nickel MsS showing that the notch is detectable in the data after waveform subtraction is performed.

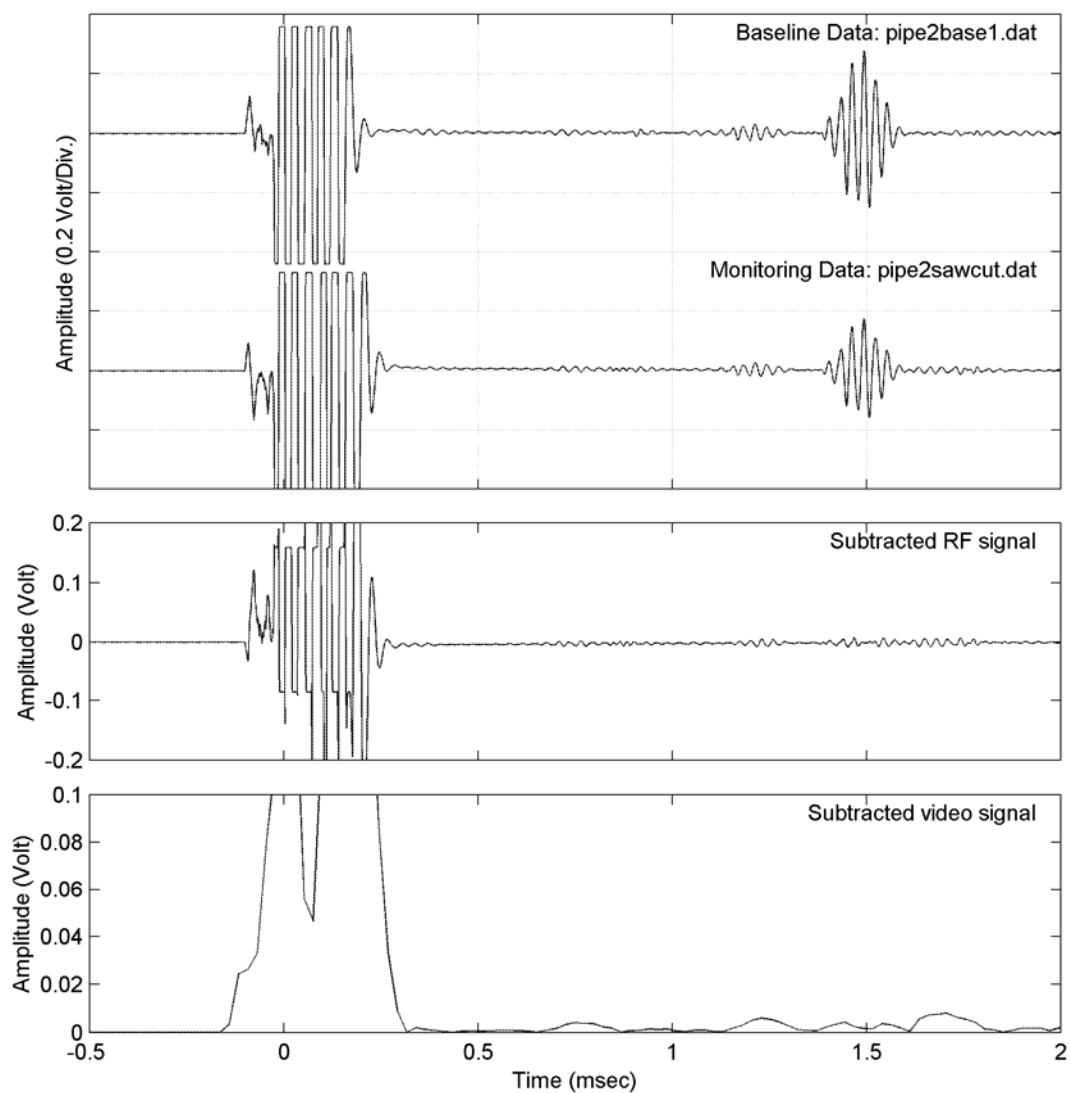


Figure 92. Waveform data collected using the segmented nickel MsS showing that the notch is apparent after subtraction, but less so than in the continuous nickel sensor data.

3. CONCLUSIONS

As a result of the work conducted under this project, a number of conclusions were reached.

- (1) The nickel based magnetostrictive sensor (MsS) technology can be used to monitor a number of structural failure mechanisms including
 - debonding of adhesively bonded patches on plate structure (not honeycomb structure)
 - defect growth under an adhesively bonded patch
 - defects under fasteners
- (2) For monitoring aluminum aircraft structure exposed to a temperature range of approximately -65°F to 150°F , the nickel must be bonded to the aluminum at room temperature with an adhesive similar to 3MTM467, not 5-minute or similar epoxies.
- (3) For monitoring steel structure, nickel bonded with 5-minute or similar epoxy can be used even over the temperature range of approximately -300°F to 150°F .
- (4) Data acquisition and analysis software is available to allow effective subtraction of waveforms obtained at various times for given structures so that very small changes in the structure can be detected.
- (5) A rule of thumb for defect detection sensitivity for various types of structures is given in Table 2.

Table 2. Defect Detection Capability and Sensitivity Observed in Various Types of Geometry using the MsS Monitoring Technique

GEOMETRY	TYPE OF DEFECT	SENSITIVITY
Bonded aluminum patch on 1/8-inch-thick aluminum plate	Patch debond	Patch corner debond defects on the order of 1/2 inch by 1/2 inch could be detected
Bonded thermal blanket on aluminum honey-comb structure	Debond of thermal material on stress isolation pad (SIP)	Debonds could not be detected between the SIP and the honeycomb structure. More work is needed to evaluate MsS capability on honeycomb structure.
Fastener holes in 1/4-inch-thick aluminum plate	Notch and simulated corrosion on fastener holes	Changes in notch length of approximately 0.1 inch could be detected. Changes in corrosion depth of 0.03 inch could be detected.
12-inch-diameter aluminum pipe	Notches	Notch defects on the order of 2% of the total pipe wall cross section could be detected

- (6) Preliminary modeling using the transmission line approach that was developed that provides insight into wave propagation and reflection by different types of reflectors in one- and two-dimensional geometries.
- (7) A number of example applications of MsS were demonstrated and evaluated in the laboratory.
- (8) The MsS technology is clearly ready for evaluation on real world applications and flight tests.
- (9) The MsS technology can be used in either the PE or PC mode for monitoring bond quality of adhesively bonded patches.

4. FUTURE WORK

Although this project showed that the MsS technology is ready for flight testing, more work is needed to

- (1) Optimize the adhesives used to mount the MsS probes to the structures,
- (2) Identify and develop ways to mitigate life limiting parameters of the MsS probes
- (3) Automate algorithms for subtracting appropriate waves forms and develop autonomous reasoning capability
- (4) Study the interaction of the guided waves with honeycomb structure so that monitoring can be accomplished for honeycomb structure.
- (5) Develop embedded sensor technology on the MsS probe including placement of excitation coils on the nickel strip and wireless communication capability
- (6) Develop modeling process for characterizing the received MsS signal.

5. REFERENCES

- (1) R. M. Bozorth, Ferromagnetism. New Jersey: IEEE Press, 1978, p. 663
- (2) M. J. Sablik, K. J. Telschow, B. Augustyniak, J. Grubba, and M. Chmielewski, "Relationship Between Magnetostriction and the Magnetostrictive Coupling Coefficient for Magnetostrictive Generation of Elastic Waves," *Review of Progress in Quantitative NDE*, vol. **21**, ed. D. O. Thompson and D. E. Chimenti (AIP, N.Y., N.Y., 2002), pp. 1613-1620
- (3) D. Jiles, "Introduction to magnetism and magnetic materials," Chapman and Hall, 1998
- (4) L. Callegaro and E. Puppini, "Rotational hysteresis model for stressed ferromagnetic films," *IEEE Transactions on Magnetics*, vol. 33, no. 2, p. 1007, 1997
- (5) L. Callegaro, E. Puppini, and A. Vannucchi, "Magneto-optical measurements on mechanically stressed thin ferromagnetic films," *Rev. Sci. Instrum.*, vol. 67, p. 1065, 1995
- (6) L. Callegaro and E. Puppini, "Stress dependence of coercivity in Ni films: Thin film to bulk transition," *Appl. Phys. Lett.*, vol. 68, p. 1279, 1996
- (7) H. Kwun and C. Dynes, "Long-range guided wave inspection of pipe using the magnetostrictive sensor technology — feasibility of defect characterization," *International Society for Optical Engineering (SPIE)* Vol. 3398, pp. 28–34 (1998)
- (8) M. P. David, *Microwave Engineering* (John Wiley & Sons, New York, 1988), Chapter 5
- (9) R. M. Bozorth, Ferromagnetism, loc. cit., p. 658
- (10) *ibid*, p. 656
- (11) X. Liu, A. Berger, and M. Wuttig, "Stability of the Perpendicular Magnetic Anisotropy of Ultrathin Ni films on Cu(100) upon Multiple Magnetization Reversals," *Phys. Rev. B* **63**, 144407 (2000)
- (12) P. LeFebvre, H. Magnan, A. Midoir, D. Chandesris, H. Jaffres, A. Fert, and J. P. Peyrade, "Correlation in Structure between Thin Films and Nanostructures," *Surf. Rev. & Lett.* **6**, 753 (1999)

APPENDIX 1

Information on Epoxies Evaluated to Determine their Capability to Couple T-Waves through the Epoxy into the Plate

SAMPLE ID	EPOXY MANUFACTURER	ESTIMATED STRENGTH	OTHER COMMENTS	COUPLES SHEAR-MODE
1A	Devcon 5 Minute®		Viscous mixture that is easy to apply to pipe and nickel with tongue depressor. Cures in 5 minutes and this means good preparation is needed before applying to the pipe	Yes
1B	Clock Spring® 440A	>1,200 psi shear	1 part activator to 10 parts adhesive makes thick mixture that is easy to apply to the pipe with tongue depressor. Initial cure in approximately 3 hours with final cure in 24 hours. Has an offensive odor. Bond quality and ability to couple torsional waves was good within 24 hours, but maximized between 3 and 7 days.	Yes
2A	3M™Scotchweld DP-100		Similar to Devcon 5-Minute® epoxy. Easy to apply with tongue depressor	Yes
2B	3M Super 77		Spray adhesive. Easy to apply, no mixing required	Poor Coupling
3A	Bond-It 7040		Mix two equal parts, makes white viscous gel, easy to apply with tongue depressor, requires 24-hour cure time	Yes
3B	Cotronics Durabond 454	10,000 psi tensile	Mix 2 parts of resin with 1 part of hardener, makes very thick paste, easy to apply with tongue depressor but difficult to produce a thin bond line, requires 24-hour cure time	Yes
4A	Cotronics Duralco 4540N	10,000 psi tensile	Requires applicator gun, viscosity like thick paint, 16-hour cure time	Did not bond well
4B	Cotronics Duralco 4461N	9,500 psi tensile	Requires applicator gun; viscosity like thin oil, therefore, difficult to apply in real pipe application; may produce thin bond line, 16-hour cure time	Yes
5A	Cotronics Duralco 4537 N	6,000 psi tensile	Requires applicator gun, easy to apply with tongue depressor, 1- to 4-hour cure time	Yes
5B	Aeropoxy ES6220	3,000 psi tensile	Mix equal parts of A and B, viscosity like thick paint, similar to Devcon 5-minute epoxy, cure time is 5 minutes	Yes
6A	Aeropoxy PR2032/PH3660	45,870 psi Tensile	Mix 3 parts 2032 to 1 part 3660, viscosity like water, 18- to 24-hour cure time, would be difficult to apply on real pipe application	Yes
6B	Aeropoxy ES6279	7,200 psi Tensile	Mix equal parts of A and B, makes thick paste, easy to apply with tongue depressor, 6- to 8-hour cure time, requires eye and hand protection	Yes

SAMPLE ID	EPOXY MANUFACTURER	ESTIMATED STRENGTH	OTHER COMMENTS	COUPLES SHEAR-MODE
7A	Epic Resins R1603/H5002	2600 to 2940 psi shear	Mix 2 parts of 1603 to 1 part of 5002, viscosity like thin paint, spreads easily with tongue depressor, cure time is 7 days	Yes
7B	Epic S7005	700 psi shear	Mix 2 parts of A to 1 part of B, makes creamy white mix, cures in 10 to 12 hours	Yes
8A	Epic S7033	2660 to 2940 psi shear	Mix equal parts of A and B, makes very stiff mixture similar to peanut butter, will not stick to pipe, cures in 2 to 4 days	Yes
8B	Epic S7045		Mix equal parts of A and B, 8 to 12-hour cure time, makes thick liquid that is easy to apply with tongue depressor	Yes
9A	Clock Spring HT180	1200 psi shear	Mix 2 parts of A to 1 part of B, makes thick liquid that is easy to apply with tongue depressor, very strong odor, cure time is unknown	Yes
9B	Armstrong A-31	2350 psi shear	Mix 3 parts of A to 1 part of B, viscosity similar to butter, 16 to 24-hour cure time, easy to apply using a tongue depressor	Yes
10A	Armstrong A-1	3000 psi tensile	Mix 100 parts of A-1 to 4 parts of Activator, 7-day cure time at room temperature, easy to apply with tongue depressor	Yes
10B	Armstrong A-3	3070 psi tensile	Mix 100 parts of A-3 to 4 parts of Activator, 7-day cure time at room temperature, easy to apply with tongue depressor	Yes
	3M™467			

APPENDIX 2

Theoretical Method for Understanding the Coupling Efficiency for Magnetostrictive Generation of Elastic Waves and for Deciding How To Select the Best Materials for the Magnetostrictive Generation of Elastic Waves

I. Formulation of Coupling Efficiency

We wish to derive an expression for coupling efficiency for magnetostrictive generation of waves. We will use a paper by Williams [1] as the basis for such a derivation.

For a number of years, confusion arose from Williams' very fine paper [1] in the 1950s, which actually gave a prescription for computing the efficiency for magnetostrictive generation of elastic waves from a sinusoidally varying magnetic field. The model was one-dimensional, and it started with the following magnetostrictive sensor equations, given as

$$H = \frac{1}{\mu} B - 4\pi\lambda \frac{\partial u}{\partial x}, \quad (1a)$$

$$T_s = E \frac{\partial u}{\partial x} - \lambda B. \quad (1b)$$

In these equations, T_s is mechanical stress, E is Young's modulus (i.e., the elastic constant), u is displacement, x is distance along the one-dimensional wire, H is magnetic field, B is magnetic induction, μ is magnetic permeability, and λ is a constant.

The confusion that has arisen from these equations is that too many people have interpreted λ as the magnetostriction. It is *not the magnetostriction*. If it were the magnetostriction, then the term $-4\pi\lambda \frac{\partial u}{\partial x}$ in Eq. (1a) would be dimensionless and inconsistent with the rest of the terms in the equation, which have units of magnetic field. In mks units, the other terms would have units of A/m . That would mean that λ would have to have *units of A/m* . Williams never calls λ the magnetostriction, but rather the "magnetostrictive constant." The confusion arises because λ is the conventional symbol for magnetostriction.

One more point is that μ is interpreted by Williams as the "reversible" permeability μ_r because the elastic wave displacement is small and the displacement vibrates at a point on the major magnetic hysteresis curve, leading to an induction perturbation about this point on the major hysteresis curve along a path known as a minor loop, which has a slope that is roughly half that of the slope of the major hysteresis curve at that point. This reduced slope has been given the misnomer of "reversible" permeability. It is a misnomer because the path followed cannot be reversible because the path exhibits hysteresis. Nevertheless, we keep in mind it is argued that μ in Eq. (1a) is really μ_r .

If λ is not the magnetostriction, then we need to understand what it really is. To do this, we go to the book by Katz [2], which writes the magnetostrictive sensor equations in the following way:

$$H = \frac{1}{\mu_{33}} B - g_{33} T_s, \quad (2a)$$

$$T_s = \frac{1}{S_{33}} \frac{\partial u}{\partial x} - \frac{g_{33}}{S_{33}} B. \quad (2b)$$

When written this way, it is easy to see that, comparing to the expression for the effective field in the Jiles-Atherton hysteresis model [3], as corrected for stress effects [4], the expression $g_{33}T_s$ is representable as

$$g_{33}T_s = \frac{3}{2} \frac{1}{\mu_o} \frac{d\lambda_m}{dM} T_s, \quad (3)$$

where *here* the symbol λ_m does indeed refer to *magnetostriction*. This expression can also be derived from the derivation found in Gurevich [5] or in the paper by Sablik, Telschow, et al. [6], which provides experimental justification for the expression as well.

We need to check if the expression for $g_{33}T_s$ has units of A/m, which is seen in the following argument:

$$g_{33}T_s = \frac{3}{2} \frac{1}{\mu_o} \frac{d\lambda_m}{dM} T_s = \frac{3}{2\mu_o} \frac{d\lambda_m}{dH} \frac{dH}{dM} T_s = \frac{3}{2} \frac{d\lambda_m}{dH} \frac{dH}{d(\mu_o M)} T_s,$$

or because $\mu_o M = B - \mu_o H = \mu H - \mu_o H = (\mu - \mu_o) H$, then $dH/d(\mu_o M) = 1/(\mu - \mu_o)$, and thus

$$g_{33}T_s = \frac{3}{2} \frac{d\lambda_m}{dH} \frac{T_s}{(\mu - \mu_o)}. \quad (4)$$

The denominator has units of magnetic induction and the numerator has units of stress (i.e., force per unit area). Thus, we have that the dimension of $g_{33}T_s$ is

$$\begin{aligned} \frac{N/m^2}{Tesla} &= \frac{J/m^3}{Wb/m^2} = \frac{J/m^3}{volt \cdot sec/m^2} = \frac{J/m}{volt \cdot sec} \\ &= \frac{\left(volt \left(\frac{coul}{sec} \right) \right) sec/m}{volt \cdot sec} = \frac{coul}{m \cdot sec} = \frac{A}{m}. \end{aligned}$$

We thus see that our expression for $g_{33}T_s$ has the correct units, and that

$$g_{33} = \frac{3}{2} \frac{d\lambda_m}{dH} \frac{1}{\mu - \mu_o}. \quad (5)$$

We shall now obtain most of what follows in terms of g_{33} . At the end, we shall use Eq. (5) and substitute for g_{33} .

Returning to Eq. (2b), and comparing to Eq. (1b), we see that

$$S_{33} = \frac{1}{E}, \quad (6)$$

and that Eqs. (1b) and (2b) can be written as

$$T_s = E \frac{\partial u}{\partial x} - (Eg_{33})B. \quad (7)$$

Thus, the two magnetostrictive sensor equations can be written as

$$H = \frac{1}{\mu}B - g_{33}T_s, \quad (7a)$$

$$T_s = E \frac{\partial u}{\partial x} - Eg_{33}B, \quad (7b)$$

analogous to Katz' equations.

We can now reexpress these equations in a form used by Williams, as follows:

$$\begin{aligned} H &= \frac{1}{\mu}B - g_{33}T_s = \frac{1}{\mu}B - g_{33} \left(E \frac{\partial u}{\partial x} - Eg_{33}B \right) \\ H &= \frac{1}{\mu}B - g_{33}E \frac{\partial u}{\partial x} + Eg_{33}^2B \end{aligned}$$

or, in other words,

$$H = \left(\frac{1}{\mu} - Eg_{33}^2 \right) B - g_{33}E \frac{\partial u}{\partial x}, \quad (8a)$$

$$T_s = E \frac{\partial u}{\partial x} - Eg_{33}B. \quad (8b)$$

These can be further reworked. First, solve for B by rearranging Eq. (8a), obtaining

$$B = \frac{H + g_{33}E \frac{\partial u}{\partial x}}{\frac{1}{\mu} - Eg_{33}^2}. \quad (9)$$

Then, substituting into Eq. (8b), the following results:

$$\begin{aligned} T_s &= E \left\{ \frac{\partial u}{\partial x} - g_{33} \left(\frac{H + g_{33}E \partial u / \partial x}{1/\mu - Eg_{33}^2} \right) \right\}, \\ T_s &= E \frac{\partial u}{\partial x} \left[1 - \frac{\mu g_{33}^2 E}{1 - \mu Eg_{33}^2} \right] - \frac{\mu g_{33} E H}{1 - \mu Eg_{33}^2} \end{aligned} \quad (10)$$

This compares to the Williams development, as follows, starting with Eq. (1b)

$$B = \frac{1}{\lambda} \left(E \frac{\partial u}{\partial x} - T_s \right),$$

and using $B = \mu H$,

$$H = \frac{1}{\mu \lambda} \left(E \frac{\partial u}{\partial x} - T_s \right) - 4\pi \lambda \frac{\partial u}{\partial x},$$

and rearranging, we obtain

$$T_s = E \frac{\partial u}{\partial x} \left(1 - \frac{4\pi \lambda^2 \mu}{E} \right) - \mu \lambda H. \quad (11)$$

By comparing Eqs. (10 and (11), we find that

$$\frac{\mu g_{33} E}{1 - \mu g_{33}^2 E} = \mu \lambda,$$

or

$$\lambda = \frac{g_{33} E}{1 - \mu g_{33}^2 E}. \quad (12)$$

Similarly,

$$\frac{\mu g_{33}^2 E}{1 - \mu g_{33}^2 E} = \frac{4\pi \lambda^2 \mu}{E} = \frac{4\pi g_{33}^2 E^2 \mu}{E (1 - \mu g_{33}^2 E)^2},$$

or

$$\begin{aligned} E^2 (1 - \mu g_{33}^2 E) &= 4\pi E^2, \\ 1 - \mu g_{33}^2 E &= 4\pi. \end{aligned} \quad (13)$$

Returning to Eq. (10), and using Eq. (13), we see that

$$T_s = E \frac{\partial u}{\partial x} \left(1 - \frac{g_{33}^2 \mu E}{4\pi} \right) - \frac{1}{4\pi} E g_{33} \mu H, \quad (14)$$

and defining

$$\bar{E} = E \left(1 - \frac{g_{33}^2 \mu E}{4\pi} \right), \quad (15)$$

we obtain a result simpler in form, namely

$$T_s = \bar{E} \frac{\partial u}{\partial x} - \left(\frac{1}{4\pi} E g_{33} \mu \right) H. \quad (16)$$

We now discuss wave generation by using the wave equation

$$\rho \frac{\partial^2 u}{\partial t^2} = \frac{\partial T_s}{\partial x}, \quad (19)$$

where ρ is mass density. Into this equation, we substitute Eq. (16) and obtain

$$\rho \frac{\partial^2 u}{\partial t^2} = \bar{E} \frac{\partial^2 u}{\partial x^2} - \left(\frac{1}{4\pi} E g_{33} \mu \right) \frac{\partial H}{\partial x}. \quad (18)$$

Furthermore, since

$$u(x, t) = u_o(k, x) e^{j\omega t}, \quad (19)$$

we have

$$-\rho \omega^2 u_o = \bar{E} \frac{\partial^2 u_o}{\partial x^2} - \left(\frac{1}{4\pi} E g_{33} \mu \right) \frac{\partial H}{\partial x},$$

or, using Eq. (15)

$$-\frac{\omega^2}{c^2} u_o = \frac{\partial^2 u_o}{\partial x^2} - \frac{1}{4\pi} \frac{g_{33} \mu E}{E \left(1 - g_{33}^2 \frac{E \mu}{4\pi} \right)} \frac{\partial H}{\partial x}.$$

In the second equation, we have substituted

$$c = \sqrt{\bar{E}/\rho}, \quad (20)$$

and now use further that $k = \omega^2/c^2$, obtaining for the wave equation of motion that

$$\frac{\partial^2 u_o}{\partial x^2} + k^2 u_o = \left(\frac{1}{4\pi} \frac{g_{33} E}{\left(1 - \frac{g_{33}^2 E \mu}{4\pi} \right)} \right) \frac{\mu}{E} \left(\frac{\partial H}{\partial x} \right). \quad (21)$$

The wave equation given by Eq. (21) can be solved as

$$u(k, x) = A e^{-jkx} + B e^{jkx} + \left[\frac{1}{4\pi} \frac{g_{33} E}{\left(1 - g_{33}^2 \frac{\mu E}{4\pi} \right)} \right] \left(\frac{\mu}{E} \right) \frac{1}{2jk}. \quad (22a)$$

$$x \int_o^x \frac{dH}{d\xi} \left\{ e^{jk(x-\xi)} - e^{-jk(x-\xi)} \right\} d\xi$$

This expression can be compared to that of Williams, which was

$$u(k, x) = Ae^{-jkx} + Be^{jkx} + \left(\frac{\lambda\mu}{\bar{E}} \right) \frac{1}{2jk} \int_0^x \frac{dH}{d\xi} \left\{ e^{jk(x-\xi)} - e^{-jk(x-\xi)} \right\} d\xi. \quad (22b)$$

Comparing Eqs. (22a) and (22b), we find that it says that, using Eq. (15)

$$\frac{\lambda\mu}{\bar{E}} = \frac{g_{33}E\mu}{4\pi \left[E \left(1 - \frac{g_{33}^2\mu E}{4\pi} \right) \right]} = \frac{g_{33}E\mu}{4\pi\bar{E}}. \quad (23)$$

To prove that this is equivalent to Eq. (12), we substitute Eq. (13) and find that

$$\lambda = \frac{g_{33}E}{1 - g_{33}^2\mu E}$$

and note that indeed we get the same expression for λ as Eq. (12).

Finally, we apply the approximate property that

$$H(x) = H_o \begin{cases} f(x), & 0 < x < \ell \\ 0, & x < 0 \text{ and } x > \ell \end{cases}, \quad (24)$$

which says that H is defined as nonzero only in the region of the coil. Substituting this, we get

$$u(k, x, t) = \frac{1}{2jk} \left[\frac{g_{33}\mu}{4\pi \left(1 - \frac{1}{4\pi} g_{33}^2\mu E \right)} \right] \int_0^\ell H(\xi) e^{jk(\xi - x + ct)} d\xi, \quad (25)$$

where the evaluation here parallels that in Williams between his Eqs. (8) and (12).

If we continue on with the development all the way to Williams' Eq. (30), one obtains a voltage gain in the signal given by

$$g = \left(\frac{4\pi\mu\lambda^2}{\bar{E}} \right) \frac{n_2}{n_1} \frac{\sin^2 \Omega}{\Omega}, \quad (26)$$

where n_1 is the number of turns in the input coil and n_2 the number of turns in the output coil, and where

$$\Omega = k\ell/2 = \pi f\ell/c, \quad (27)$$

where f is frequency. The expression

$$\gamma^2 = \frac{4\pi\mu\lambda^2}{\bar{E}} = \frac{4\pi\mu}{\bar{E}} \left(\frac{g_3 E}{1 - g_{33}^2 \mu E} \right)^2, \quad (28)$$

or

$$\gamma^2 = \frac{4\pi}{\bar{E}} \left[\frac{g_{33}^2 E^2 \mu}{(1 - g_{33}^2 \mu E)^2} \right] = \frac{g_{33}^2 E^2 \mu}{(1 - g_{33}^2 \mu E) \bar{E}},$$

or

$$\gamma^2 = \frac{g_{33}^2 \mu E^2}{1 - g_{33}^2 \mu E} \left[\frac{1}{E \left(1 - \frac{g_{33}^2 \mu E}{1 - g_{33}^2 \mu E} \right)} \right] = \frac{g_{33}^2 \mu E}{(1 - g_{33}^2 \mu E) \left[\frac{1 - 2g_{33}^2 \mu E}{1 - g_{33}^2 \mu E} \right]},$$

and finally

$$\gamma^2 = \frac{g_{33}^2 \mu E}{1 - 2g_{33}^2 \mu E}. \quad (29)$$

γ^2 is known as the “intrinsic conversion loss.” The constant γ is called the “electromechanical coupling constant.” The intrinsic conversion loss γ^2 indicates the efficiency of the material for converting magnetic energy into mechanical energy at the input, or mechanical energy into magnetic energy at the output.

Returning to the gain equation, we note that gain g depends on the intrinsic conversion loss times the number-of-turn ratio of output to input coils times a function $\sin^2 \Omega/\Omega$, which is a function of frequency.

II. Selecting Magnetostrictive Materials for Efficient Magnetostrictive Coupling

We note that coupling efficiency

$$\gamma^2 = \frac{g_{33}^2 \mu E}{1 - 2g_{33}^2 \mu E} = \frac{\left(\frac{3}{2} \frac{d\lambda_m}{dH} \frac{1}{\mu - \mu_o} \right)^2 \mu E}{1 - 2 \left(\frac{3}{2} \frac{d\lambda_m}{dH} \frac{1}{\mu - \mu_o} \right)^2 \mu E}. \quad (30)$$

This is how the magnetostriction actually enters into the coupling efficiency. It enters via its derivative with respect to H , viz. $d\lambda_m/dH$.

To check this, we use the property that an efficiency ought to be dimensionless. Thus, the quantity

$$\left(\frac{3}{2} \frac{d\lambda_m}{dH} \frac{1}{\mu - \mu_o} \right)^2 \mu E$$

ought to be dimensionless. We remember that

$$g_{33} = \left(\frac{3}{2} \frac{d\lambda_m}{dH} \frac{1}{\mu - \mu_o} \right)$$

had dimensions of $(A/m)/(N/m^2)$, since $g_{33}T_s$ had dimensions of A/m . Thus, using dimensional analysis, we have

$$\begin{aligned} \left(\frac{3}{2} \frac{d\lambda_m}{dH} \left(\frac{1}{\mu - \mu_o} \right) \right)^2 \mu E &\rightarrow \left(\frac{A}{m} / \frac{N}{m^2} \right)^2 \left(\frac{T}{A/m} \right) \left(\frac{N}{m^2} \right) \\ &\rightarrow T \cdot \frac{A}{m} \cdot \frac{N}{m^2} / \left(\frac{N}{m^2} \right)^2 \\ &\rightarrow T \cdot \frac{A}{m} \cdot \frac{J}{m^3} / \left(\frac{J}{m^2} \right)^2 \\ &\rightarrow \frac{\text{volt} \cdot \text{sec}}{m^2} \frac{A}{m} / \left(\frac{J}{m^3} \right) \\ &\rightarrow \frac{\text{volt} \cdot \text{coul}}{m^3} / \frac{J}{m^3} \rightarrow 1 \quad \text{dimensionless!} \end{aligned}$$

Thus, γ^2 is indeed dimensionless, as expected from its being an efficiency factor.

We note that if $g_{33}^2 \mu E$ is much less than 1, then so is γ^2 .

Now, γ^2 is the efficiency of the material for converting magnetic energy into mechanical energy. We note that, since μ is rather large compared to μ_o , then

$$\frac{\mu}{\mu - \mu_o} \simeq 1. \quad (31)$$

This means that the efficiency, while dimensionless, is essentially the same as

$$\gamma^2 = \frac{\rho}{4} E \left\{ \frac{(d\lambda_m/dH)^2}{\mu - \mu_o} \right\}, \quad (32)$$

or, in other words,

$$\gamma^2 \propto \frac{(d\lambda_m/dH)^2}{\mu - \mu_o},$$

where \propto is the proportionality sign meaning “is proportional to.” This is important to note because it determines selection of material.

For a good material for magnetostrictive wave generation, one wants (1) *high* $d\lambda/dH$ and (2) *low permeability* μ . If the material has low total permeability, it also will have low reversible permeability, which is roughly half the total permeability. So it does not matter whether one uses total permeability or reversible permeability in Eq. (30) or in Eq. (32). When it comes to material selection, one still needs high $d\lambda/dH$ and low permeability μ , be it total permeability or reversible permeability.

Again, (1) high $d\lambda/dH$ and (2) low permeability are the *criteria for selection of material*. It is also seen from Eq. (32) that (3) *Young's modulus* E also determines material selection. In addition to higher $d\lambda_m/dH$ and lower μ , a higher Young's modulus E would make the material more desirable. On the other hand, Young's modulus is not as likely to vary as widely as $d\lambda/dH$ or permeability, so E is the least important criterion.

III. References

1. R. C. Williams, "Theory of Magnetostrictive Delay Lines for Pulse and Continuous Wave Transmission," *IRE Trans. on Ultrasonics Engineering*, vol. **UE-7**, pp. 16–38 (1959).
2. *Solid State Magnetic and Dielectric Devices*, H. W. Katz, ed. (John Wiley & Sons, New York, NY, 1959), p. 112.
3. D. C. Jiles and D. L. Atherton, "Theory of Ferromagnetic Hysteresis," *J. Magn. Magn. Mater.*, vol. **6**, pp. 48–61 (1986).
4. M. J. Sablik and D. C. Jiles, "Coupled Magnetoelastic Theory of Magnetic and Magnetostrictive Hysteresis," *IEEE Trans. Magn.*, vol. **29**, pp. 2113–2123 (1993).
5. S. Yu. Gurevich, "The Theory of Electromagnetic Generation of Acoustic Waves in a Ferromagnetic Medium at a High Temperature," *Russ. J. NDT*, vol. **29**, pp. 193–204 (1993).
6. M. J. Sablik, K. J. Telschow, B. Augustyniak, J. Grubba, and M. Chmielewski "Relationship Between Magnetostriction and the Magnetostrictive Coupling Coefficient for Magnetostrictive Generation of Elastic Waves," *Review of Progress in Quantitative NDE*, vol. **21**, ed. D. O. Thompson and D. E. Chimenti (AIP, N.Y., N.Y., 2002), pp